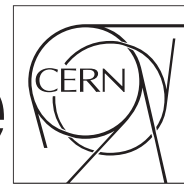


The Compact Muon Solenoid Experiment

CMS Draft Note

Mailing address: CMS CERN, CH-1211 GENEVA 23, Switzerland



2011/03/23

Head Id: 45398

Archive Id: 29932:47166MP

Archive Date: 2011/03/12

Archive Tag: trunk

Search for Collimated Groups of Muons

Jim Pivarski, Aysen Tatarinov, and Alexei Safonov
 Texas A&M University

Abstract

We present an inclusive, signature-based search for groups of collimated muons, arising from spectroscopic cascades in a hidden sector accessible only through high-energy collisions, using the CMS detector. In several signatures defined by number of muons per collimated group and number of groups per event, we searched for the lightest on-shell state in the hidden spectrum with a mass-peak fit and set limits on $\sigma\mathcal{B}\alpha$, where α is the model acceptance of the signature. With no excess of data events compared to the expectation, production rate for the new resonances within the experimental acceptance is ruled out at the level of 0.1–0.5 pb at 95% C.L. depending of the signature and the mass of the new lightest state within $0.25 < m < 5 \text{ GeV}/c^2$. We also set $\sigma\mathcal{B}$ limits on two representative benchmark scenarios for SUSY with a hidden dark sector and the NMSSM Higgs production in the channel $h_1 \rightarrow a_1 a_1 \rightarrow 4\mu$.

This box is only visible in draft mode. Please make sure the values below make sense.

PDFAuthor: Jim Pivarski, Alexei Safonov, Aysen Tatarinov
 PDFTitle: Search for Collimated Groups of Muons
 PDFSubject: CMS
 PDFKeywords: CMS, physics, software, computing

Please also verify that the abstract does not use any user defined symbols

1 Introduction

2 1.1 Motivation

3 Although the dimuon mass spectrum is well understood in e^+e^- and $p\bar{p}$ collisions up to col-
 4 lision energies of 0.2 and 2 TeV respectively, new states may be hidden by weak couplings
 5 to Standard Model particles. A wide class of hidden-valley models predicts new states cou-
 6 pling weakly to the Standard Model yet significantly to a hidden sector, accessible to the LHC
 7 through massive particles that connect the two sectors. In these scenarios, massive particles M
 8 would be created singly or in pairs and then decay through the hidden spectrum to the lightest
 9 hidden state: e.g. $pp \rightarrow M\bar{M}$ and $M \rightarrow mX$ where m is the lightest hidden particle in a cascade
 10 chain. If m is unstable, it would decay with very small width to the kinematically-accessible
 11 Standard Model states, either democratically (Z-like) or to the heaviest accessible state (Higgs-
 12 like). Muon-pair final states would appear as a low-mass, high-momentum dimuon resonance,
 13 and therefore be collimated by relativistic boost. With several low-mass states in the decay
 14 chain, e.g. $m_2 \rightarrow m_1 m_1 \rightarrow 4\mu$, cascades would either produce two groups of collimated
 15 dimuons or one group of four collimated muons, depending on the boost of m_2 . Arbitrarily
 16 complex decay chains are conceivable, and groups of muons might be produced in association
 17 with other Standard Model pairs, such as e^+e^- and hadrons. These striking signatures are often
 18 called “lepton jets.”

19 Hidden, low-mass resonances are especially interesting in light of the high-energy positron ex-
 20 cess reported by the PAMELA primary cosmic-ray experiment [1]. While pulsars cannot be
 21 conclusively ruled out as the source of this excess [2], the interstellar positrons could be the
 22 product of WIMP annihilations [3], assuming that the WIMP annihilation rate is higher than
 23 what would be expected from thermal freeze-out in the early universe, and also assuming
 24 some mechanism to prohibit decay chains that produce antiprotons, in which no excess was
 25 observed. A new force boson, a_{dark} , with a mass of approximately $1 \text{ GeV}/c^2$ and coupling sig-
 26 nificantly to WIMPs yet weakly to Standard Model particles, would explain both observations.
 27 Acting as a long-range Yukawa force, a_{dark} would draw together slow-moving WIMPs, increas-
 28 ing their effective annihilation cross-section in the modern era without affecting their produc-
 29 tion in the early universe. This mechanism is known as the Sommerfeld enhancement [4, 5].
 30 The lack of an antiproton excess in PAMELA data [6] can be consistent with these models if the
 31 $a_{\text{dark}} \rightarrow p\bar{p}X$ channel were kinematically forbidden [3]; that is, if the mass of a_{dark} were below
 32 $2 \text{ GeV}/c^2$ or so. Alternatively, a_{dark} can have a preferential coupling to leptons [7, 8], which
 33 could also explain the annual modulation reported by the DAMA/LIBRA experiment [9]. Rel-
 34 atively simple extensions of this picture (see [3] for details), such as adding a dark Higgs boson
 35 h_{dark} to give the a_{dark} its mass, or introducing the force with non-abelian structure, would pro-
 36 duce more complex event topologies: 2^N fermion pairs per lepton jet for a two-body decay
 37 chain with N light states and/or several lepton jets per event if the decay chain includes heavy
 38 particles. These models are particularly natural in the context of supersymmetry. Depending
 39 on the strength of the coupling of the dark sector to MSSM, at the LHC one can expect the
 40 new signatures to be detectable in MSSM squark/gluino production followed by two some-
 41 what different types of cascade decays leading to appearance of the dark sector particles. If
 42 the coupling is weak, the MSSM cascades proceed in a standard fashion down to the MSSM
 43 LSP, which can then decay to the “dark photon” and “dark neutralino,” with the latter being
 44 the truly stable dark matter particle [10]. If the coupling is strong, one may expect new large
 45 decay channels for squarks into the dark sector particles [11]. Searches for lepton jets have been
 46 performed at DØ [12, 13] with no observed signal, but the Tevatron energy may just be too low
 47 to access these signals.

Another, very different, motivation derives in the context of Next-to-Minimal Supersymmetric Model (NMSSM) [14–20], which extends MSSM by an additional singlet superfield $\langle S \rangle$ in the superpotential. That leads to an extension of the Higgs sector compared to MSSM, particularly to the addition of a light higgs boson a_1 that can couple of the SM-like Higgs and substantially broaden the phenomenology of the Higgs sector. Apart from reducing the fine-tuning present in MSSM [21] and solving the so-called “ μ -problem” [22], the NMSSM relieves the tension between the low Higgs mass predicted by precision electroweak fits and the direct LEP limit of $114 \text{ GeV}/c^2$. This particular limit assumes that the Higgs boson decays directly into Standard Model particles with known branching fractions. If additional light Higgs bosons allow for Higgs-to-Higgs decays, the direct limit may be circumvented. In a well-defined region of Next-to Minimal SuperSymmetric (NMSSM) parameter space, the lightest CP-odd Higgs (a_1) can have arbitrarily low mass. Below the $2m_\tau$ threshold, the branching fraction for $a_1 \rightarrow \mu\mu$ is about 20%, making its detection in the muon channel viable at the LHC with already modest amounts of data [23]. For values of the NMSSM parameters that give the lightest CP-even Higgs (h_1) a large singlet field component, $h_1 \rightarrow a_1 a_1$ can be as large as 100%. If nature has chosen this path, the lightest CP-even Higgs mass could be as low as $86 \text{ GeV}/c^2$ and the primary light Higgs decay mode could be $h_1 \rightarrow a_1 a_1 \rightarrow 2\mu, 2\mu$, where the dimuons appear as well-collimated lepton jets. The strongest constraints on the NMSSM scenarios with light a_1 come from LEP [24]. Searches at BaBar and CLEO [25, 26] have little impact on the allowed parameter space as well as the DØsearch for this signature [27], which has only a small impact on the allowed parameter space as it was shown in [23].

1.2 Analysis Strategy

This analysis is an inclusive, signature-based search for resonant production of light bosons m_1 that decay to pairs of muons (the mass range searches is from 0.25 to $5 \text{ GeV}/c^2$). To preserve the model independence of the search, selections are designed to have minimal dependence on the exact production mechanism of the new bosons, e.g. whether they are produced in electroweak-like processes leading to final states with isolated dimuons, produced inside hadronic jets, or in cascades of new particles. The only assumption made in the latter case is that all or some of the decay chains in the hidden sector reach an on-shell lowest-mass state m_1 before its final decay, as illustrated in Fig. 1(a). Similarly, selections are designed to be insensitive to whether m_1 decays exclusively to muons or has other allowed decay channels, e.g. e^+e^- or hadron decays. Such model independence is achieved by avoiding the use of isolation requirements, which could otherwise severely link acceptances to the details of the production mechanism and decay branching fractions. As an illustration, Fig. 1(b) shows a possible topology where the decay products of two or more spatially close new bosons overlap, leading to either “muon jets,” or “mixed jets,” in which some of the m_1 bosons decay to non-muon modes. Finally, to avoid unnecessary model dependencies, additional objects, such as isolated single leptons, hadronic jets, and missing energy, are neither required in the search nor are they forbidden.

The strategy of the analysis is to select events with multiple muon candidates per event, identify the combination of muon pairs most compatible with the decays of low mass resonances, and search for an enhancement in the production of muon pairs consistent with the hypothesis of being the decay products of particles of the same mass. Here we give an overview of the analysis, full details and definitions are provided in the rest of the note. Selection of muon pairs proceeds in two steps. First, muons satisfying a minimum- p_T threshold ($p_T > 5 \text{ GeV}/c$) are iteratively grouped into “mu-jets” if a new muon and any oppositely charged muon in the jet have pairwise invariant mass $m_{\mu\mu} < 9 \text{ GeV}/c^2$. The procedure continues until all “mu-jets” are built. There is no limit on the number of muons per group, and not all muons need to

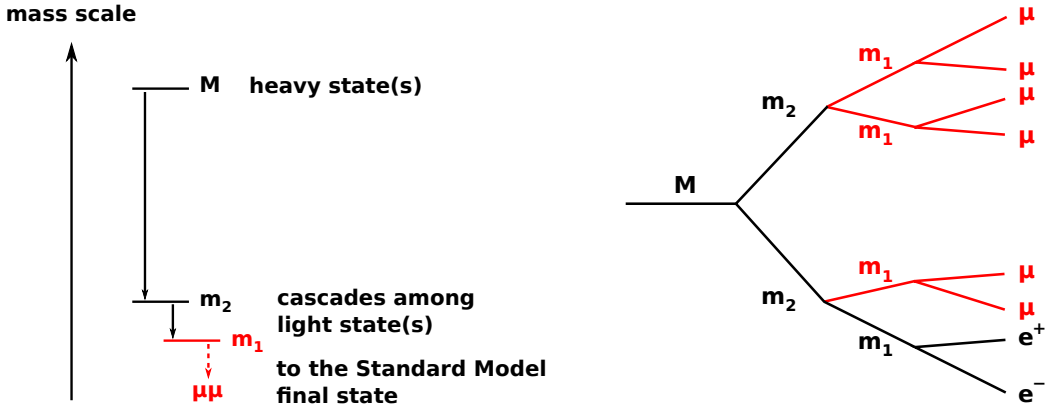


Figure 1: Schematic of a decay chain from heavy states in the hidden sector to light states, ultimately to Standard Model pairs. We identify groups of muons collimated by boost, possibly containing non-muons and search for a resonance in muon pairs from $m_1 \rightarrow \mu\mu$.

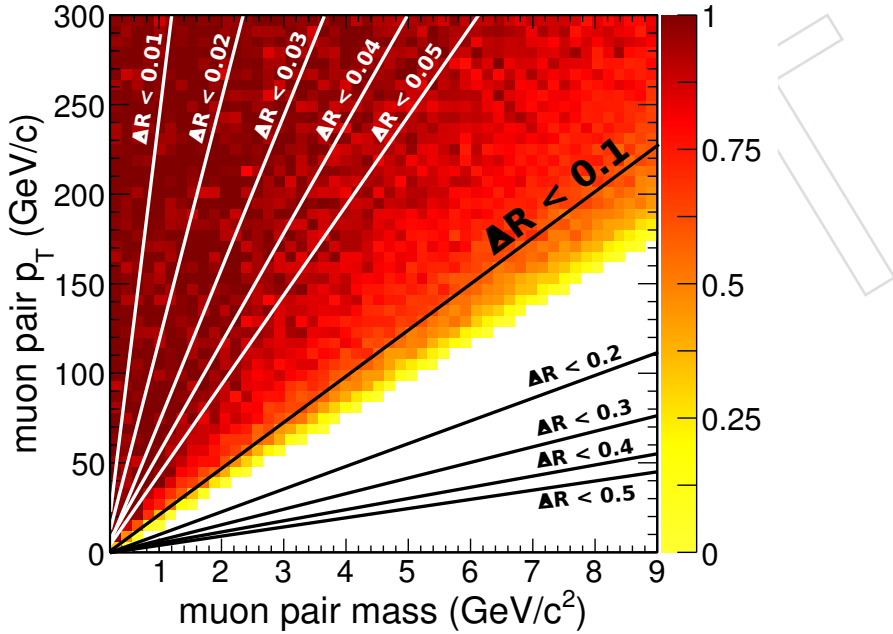


Figure 2: Mass and momentum of dimuons from a toy Monte Carlo (uniform in mass, p_T , η with scalar decays); color scale indicates the fraction that pass $\Delta R < 0.1$. Contour lines are overlaid at the center (50% edges) of similar turn-on curves for a range of ΔR values.

- 95 be grouped (isolated muons are allowed). Note that this definition is kinematic, rather than a
 96 geometric based on a ΔR -cone algorithm¹, as was used in the Tevatron searches [13]. The latter
 97 leads to unnecessary inefficiencies for resonances of higher masses or for pairs produced with
 98 a moderate transverse momentum, which can happen in the dark SUSY $U(1)$ model if mass
 99 splitting $\chi_1^0 - \chi_{dark}^0$ is not too large or in the NMSSM as it is illustrated in Fig. 2.
 100 The second step in the procedure is to classify events by the number of mu-jets and the number
 101 of muons in each mu-jet (if there are other muons in the event not clustered into mu-jets, they do
 102 not affect classification). Next, high-multiplicity mu-jets are split into a set of electrically neutral

¹ $\Delta R = \sqrt{(\Delta\phi)^2 + (\Delta\eta)^2}$

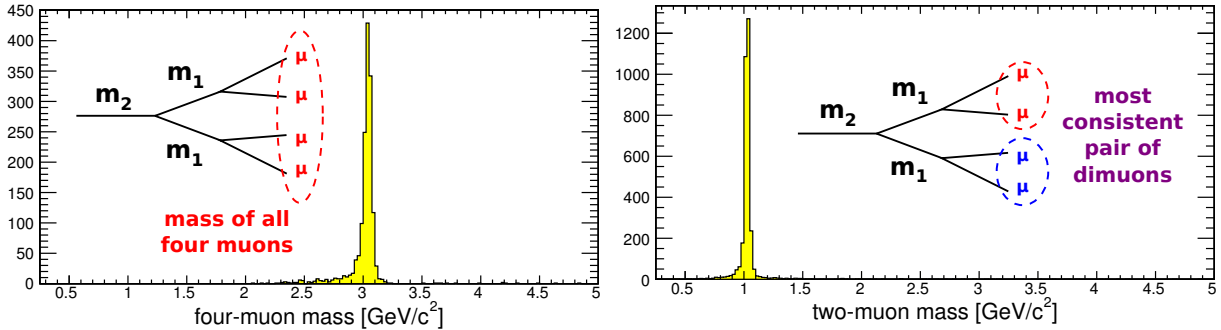


Figure 3: Identification of fundamental dimuons in a mu-jet containing four muons from $m_2 \rightarrow m_1 m_1 \rightarrow 4\mu$. The invariant mass of all four muons is a sharp peak at m_2 ($3 \text{ GeV}/c^2$ in this example), and the invariant mass of the most consistent pair of dimuons within this mu-jet is a sharp peak at m_1 ($1 \text{ GeV}/c^2$ in this example).

- 103 muon pairs most consistent with having a common invariant mass (across all muons clustered
 104 in mu-jets in the entire event). The best assignment of opposite-sign pairs is preserved for the
 105 remainder of the analysis and are referred to as “fundamental dimuons.” The effectiveness of
 106 this simple procedure is illustrated in Fig. 3 for a sample signal with a mu-jet containing four
 107 muons from $m_2 \rightarrow m_1 m_1 \rightarrow 4\mu$ ($m_2 = 3 \text{ GeV}/c^2$ and $m_1 = 1 \text{ GeV}/c^2$) by showing the invariant
 108 masses of the selected “fudamental dimuons” as well as the invariant mass of all four muons.
 109 Next, we categorize events based on the number of mu-jets $N_{\mu\text{-jet}}$ and the number of funda-
 110 mental di-muons in each mu-jet $N_{\mu\mu}$ as these correspond to different signal topologies and
 111 therefore have different sensitivities to particular models of interest. These topologies are
 112 shown in Table 1.

Table 1: Topologies used to categorize events based on the number of mu-jets and the number of muon pairs (fundamental dimuons) in each mu-jet.

region	Description	Targeted Models
	$N_{\mu\text{-jet}} = 1$:	
(a-1)	one dimuon with $p_T > 80 \text{ GeV}/c$	single high- p_T $m_1 \rightarrow \mu\mu$
(a-2)	two fundamental dimuons in a single mu-jet (4μ)	cascades, e.g. $m_2 \rightarrow 2m_1 \rightarrow 4\mu$
(a-3)	more than four muons in the mu-jet	more complex hierarchy
	$N_{\mu\text{-jet}} = 2$:	
(b-1)	both mu-jets contain exactly two muons	heavy $M \rightarrow m_1 m_1 \rightarrow 4\mu$ (e.g. NMSSM Higgs)
(b-2)	one of the two mu-jets has more than two muons	e.g. $M \rightarrow m_2 m_1$ or $m_2 m_2$
	$N_{\mu\text{-jet}} \geq 3$:	
(c-1)	> 2 mu-jets with any numbers of muons	more complex hierarchy

- 113 To be explicit, the multi-muon signatures that are excluded from this analysis acceptance are
 114 the following:

- 115 • events with no mu-jets (e.g. a $Z \rightarrow \mu\mu$ event will not have muons clustered into a
 116 mu-jet)
- 117 • events with exactly one mu-jet containing exactly two muons with $p_T < 80 \text{ GeV}/c$
 118 (backgrounds are too high, used as a control sample);
- 119 • events with exactly one mu-jet containing three muons (negligible signal, used as a

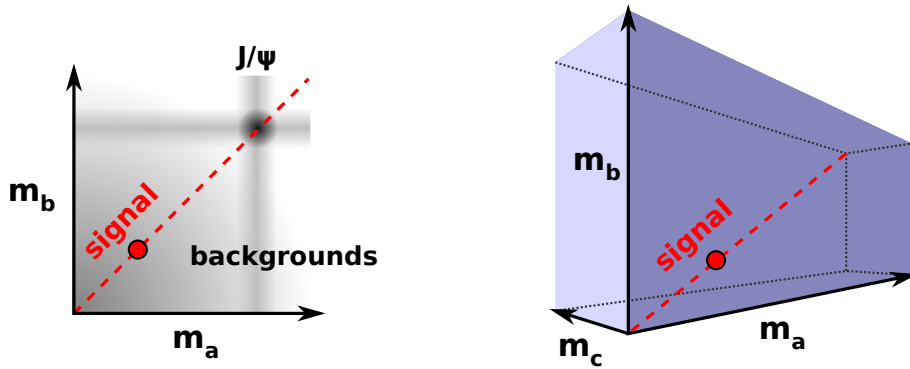


Figure 4: Schematic of multi-dimensional search for signal in topologies with two (a) and three (b) dimuons in the event. The signal, if observed, will appear as a peak somewhere on the diagonal while the backgrounds events will have a distribution spread across the entire multi-dimensional space. Known resonances may form an enhancement near the diagonal, but those will also appear as vertical or horizontal acceptances in events that have only one of the dimuons coming from a resonance.

120 control sample);

121 As a reminder, any additional ungrouped muons are not counted as mu-jets because a mu-
122 jet requires at least two opposite charged muons in it. A muon would not be grouped if its
123 pairwise invariant mass is greater than $9 \text{ GeV}/c^2$ with respect to all other muons of opposite
124 charge in the same vertex.

125 Events in each category have a fixed number of fundamental dimuons; in the case of signal
126 events, all such dimuons should have compatible masses, as they originate from the decays
127 of the same particle type, while the background events do not have such correlations. For a
128 sample topology with two or three reconstructed dimuons in the event, this is schematically
129 illustrated in Figs. 4(a) and (b), respectively. The signal, if observed, will be somewhere on the
130 diagonal while the backgrounds will be distributed across the entire multi-dimensional space.
131 Known resonances may form an enhancement near the diagonal, but those will also appear as
132 vertical or horizontal acceptances in events that have only one of the dimuons coming from
133 a resonance. We therefore analyze the $N_{\mu\mu}$ -dimensional distribution of fundamental dimuon
134 masses for each category and search for an enhancement near the diagonal. In some of the
135 topologies, one could also analyze the invariant mass distributions for groups of fundamental
136 dimuons in the same mu-jet to search for a possible hierachial structure of the hidden sector.
137 To avoid overcomplicating the interpretation of our results, we decided to base the main results
138 on an analysis of the $N_{\mu\mu}$ -dimensional space of fundamental dimuon masses alone. However,
139 if an excess is observed, we will perform an additional analysis, searching for possible structure
140 in the spectrum of new particles.

141 The analysis of the multi-dimensional spectra is performed using a binned likelihood fit with
142 the background shape determined from properly defined background-enriched samples and a
143 Crystal Ball shape used to model the signal. For multi-dimuon topologies, the fit is performed
144 in the region near the diagonal, while the normalization for background is determined from
145 the fit in the side-band (off-diagonal) region. For single-dimuon topologies, a fit with floating
146 signal and background normalizations is used. The posterior for the signal normalization is
147 used to either discover or set limits on the production rate of new resonances.

2 Benchmark Models for Signals of New Physics

2.1 SUSY with Extra- $\mathcal{U}(1)_{\text{dark}}$

The scenario we explore is described in [10] and is an extension of the ordinary MSSM content with the new particles, most notably a new dark matter particle $\tilde{\chi}_{\text{dark}}$, a light mediator a_{dark} , and a dark Higgs h_{dark} to give the mediator its mass. The ordinary MSSM LSP is not stable and decays to $\tilde{\chi}_{\text{dark}}$ in combination with h_{dark} or a_{dark} , or even both (small contribution, $B(\tilde{\chi}_1^0 \rightarrow h_d \gamma_d \tilde{\chi}_d) \sim 2\%$).

More specifically, the visible sector in this model is the ordinary MSSM with a Bino-like neutralino LSP, $\tilde{\chi}_0$. The dark sector contains a $\mathcal{U}(1)_{\text{dark}}$ gauge group, and two Higgs superfields with opposite charges under $\mathcal{U}(1)_{\text{dark}}$. The dark sector interacts with the ordinary MSSM sector through a small kinetic mixing between the $\mathcal{U}(1)_{\text{dark}}$ gauge superfield and the $\mathcal{U}(1)_Y$ gauge superfield. The dark sector LSP is the dark Higgsino, $\tilde{\chi}_{\text{dark}}$ and is the DM candidate. Correspondingly, the dark gauge boson, which is identified as the mediator a_{dark} , provides an attractive force between two $\tilde{\chi}_{\text{dark}}$ particles. $\mathcal{U}(1)_{\text{dark}}$ is broken by the vacuum expectation values of the dark Higgs fields (the lightest physical Higgs is denoted as h_{dark}), which provide a_{dark} a mass of $O(1 \text{ GeV}/c^2)$. Due to kinetic mixing, a_{dark} can decay to two SM leptons.

If $m(h_{\text{dark}}) > 2m(a_{\text{dark}})$, h_{dark} mainly decays to two on-shell a_{dark} particles, which subsequently decay to four Standard Model fermions. For $m(\tilde{\chi}_{\text{dark}}) < m(\tilde{\chi}_0^1)$, the MSSM LSP decays via $\tilde{\chi}_0^1 \rightarrow \tilde{\chi}_{\text{dark}} h_{\text{dark}}$, $\tilde{\chi}_0^1 \rightarrow \tilde{\chi}_{\text{dark}} a_{\text{dark}}$, or 3-body $\tilde{\chi}_0^1 \rightarrow \tilde{\chi}_{\text{dark}} h_{\text{dark}} a_{\text{dark}}$. The ratio of the three-body and the two-body decay widths can be hypothetically measured and used to determine the coupling g .

The exact parameters chosen are: $m(\tilde{\chi}_{\text{dark}}) = 300 \text{ GeV}/c^2$, $m(a_{\text{dark}}) = 1 \text{ GeV}/c^2$, and $m(h_{\text{dark}}) = 3 \text{ GeV}/c^2$, the coupling constant $g = 0.40$ (provides the correct DM relic density). In the MSSM sector, the LSP mass was set to $m(\tilde{\chi}_0^1) = 400 \text{ GeV}/c^2$ and we scanned over the gluino mass from 500 to 1200 GeV/c^2 while the squark masses for first two generations were set to $m(\tilde{q}) = m(\tilde{g})/1.2$ (the third one was assumed to be heavier). In this scenario, the gluino directly decays to quark plus squark and the squark only directly decays to quark plus $\tilde{\chi}_0$.

Samples were generated using MadGraph [28] for $2 \rightarrow 2$ squark/gluino production. The 2-body and 3-body decays for $\tilde{\chi}_0$ are performed with CalcHEP [29] and all other particles, including a_{dark} , h_{dark} and the other super particles, are decayed with BRIDGE [30]. In simulating the samples, we set branching for a_{dark} decays to two muons as 100%, and we will comment on the case with a_{dark} decaying to electrons later. The parton-level events (in the LHE format) are further processed with PYTHIA for showering/hadronization, and a CMS GEANT simulation for detector response. All of the above have typical pile-up for the 2010 data (estimated for $\mathcal{L} = 6.9 \times 10^{31}$ with 156 bunch-crossings, an average of 3 pp collisions per crossing).

The total cross section for this model is essentially the MSSM cross-section (calculated using MadGraph) for squark/gluino production and depends on gluino and squark masses. Numeric values were obtained using MadGraph. The final states are determined by the decay channels of the lightest MSSM neutralino decaying to one of the three combinations: $\tilde{\chi}_{\text{dark}} h_{\text{dark}}$, $\tilde{\chi}_{\text{dark}} a_{\text{dark}}$ with branching fractions of 48.7% each, and $\tilde{\chi}_{\text{dark}} h_{\text{dark}} a_{\text{dark}}$ with a branching fraction of 2.6%.

Because the assumption of $B(a \rightarrow \mu\mu) = 100\%$ may not be true if decay channels $a \rightarrow e^+e^-$, $a \rightarrow \rho \rightarrow \pi\pi$ are allowed, we produced additional samples using the original LHE files by flagging some of the a_{dark} and dropping muons from their decay from consideration, to simulate cases with $B(a_{\text{dark}} \rightarrow \mu\mu) = 50\%$ and 33%.

193 2.2 SUSY with Dark Fermion Cascades

194 Another possible scenario is SUSY with stronger coupling to MSSM and a more complex dark
 195 sector consisting of an hierarchy of the new dark bosons and fermions. Here, we follow the
 196 model described in [11]. The dark photons are produced in cascade decays of dark fermions,
 197 radiating γ_{dark} or a_{dark} , e.g. $\tilde{n}_2 \rightarrow \tilde{n}_1 \gamma_{\text{dark}}$ or $\tilde{n}_2 \rightarrow \tilde{n}_1 a_{\text{dark}} (\rightarrow \gamma_{\text{dark}} \gamma_{\text{dark}})$ followed by $\gamma_{\text{dark}} \rightarrow$
 198 $\mu\mu$ or $\gamma_{\text{dark}} \rightarrow e^+ e^-$. Such dark fermions can be produced at the LHC in strong production
 199 of squarks $pp \rightarrow \tilde{q}\tilde{q}/\tilde{q}\tilde{g}$ with each squark decaying via $\tilde{q} \rightarrow q\tilde{n}_2$. Depending on the mass
 200 hierarchy of \tilde{n}_2 , \tilde{n}_1 , and γ_{dark} , one could expect either resonant or non-resonant decays of γ_{dark}
 201 to pairs of muons. In this scenario, \tilde{n}_1 is assumed to be stable on the typical collider detector
 202 lifetimes. We treat the two scenarios with the squark cascading into either one or two dark
 203 photons separately, which assumes that one of the decay topologies may be dominant. If this
 204 assumption is not correct, the experimental results can be reinterpreted allowing both types
 205 of decays in the same event. The MC samples were produced for the range of squark masses
 206 from $m(\tilde{q}) = 200\text{--}700 \text{ GeV}/c^2$ in steps of $50 \text{ GeV}/c^2$. Gluino mass was set $m(\tilde{g}) = 1.2m(\tilde{q})$.
 207 As a benchmark example scenario for the acceptance calculation shown in the next section,
 208 masses of new particles were set to $m(n_2) = 2$, $m(n_1) = 0.5$, $m(\gamma_{\text{dark}}) = 0.5$, $m(h_{\text{dark}}) = 1.2$
 209 GeV/c^2 . Two subsets of models were considered with $\mathcal{B}(n_2 \rightarrow n_1 h_{\text{dark}}) = 100\%$ or $\mathcal{B}(n_2 \rightarrow$
 210 $n_1 h_{\text{dark}} \rightarrow n_1 a_{\text{dark}} a_{\text{dark}}) = 100\%$. We emulated the scenarios for $\mathcal{B}(a_{\text{dark}} \rightarrow \mu\mu)$ taking values
 211 of 100, 50, and 33%. Note that the cross-sections used in comparisons of experimental limits
 212 and theoretical predictions is calculated in the assumption of squark mass universality (for all
 213 three generations) at the electroweak scale. If these masses are not universal, the cross-section
 214 can be substantially lower.

215 2.3 NMSSM: Modified SM-like Higgs Decay Dynamics

216 As mentioned earlier, the NMSSM extends the standard MSSM by additional singlet superfield
 217 leading to broader phenomenology of Higgs production and decay dynamics. In particular, the
 218 new allowed decay modes of the SM-like Higgs reduce the branching fractions for Higgs decays
 219 into conventional channels weakening LEP limits on allowed Higgs mass range. We follow the
 220 phenomenological study published in [23] and explore the scenario where the CP-even Higgs
 221 h_1 (the SM-like Higgs) decays via $h_1 \rightarrow a_1 a_1$, where a_1 is a new light CP-odd Higgs a_1 (which
 222 typically carries a large fraction of the NMSSM singlet field). If a_1 is lighter than $2m_\tau$, it has a
 223 high branching fraction for decays into muon pairs, $h_1 \rightarrow a_1 a_1 \rightarrow 2\mu 2\mu$. Both the production
 224 rate for the SM-like Higgs h_1 (via gluon fusion predominantly) as well as the branching fraction
 225 for $h_1 \rightarrow a_1 a_1$ can vary significantly depending on the singlet fraction of h_1 and a_1 . Typical
 226 production cross-sections $\sigma(pp \rightarrow h_1)$ can vary from 0.05 to $\sim 10 \text{ pb}$ while $\mathcal{B}(h_1 \rightarrow a_1 a_1)$ can
 227 be as high as 100%. Simulated events for a benchmark NMSSM scenario are produced using
 228 Pythia 6's [31] MSSM Higgs subroutines (the $gg \rightarrow h$ production with a subsequent decay of
 229 $h \rightarrow AA$). Higgs masses are set by hand to $m_h = 100$ and $m_a = 2 \text{ GeV}/c^2$. The cross-section
 230 times branching fraction for this topology, with these masses, can be anything from 0.05 to
 231 10 pb, depending on the free parameters of the model, especially λ , the trilinear coupling in
 232 the NMSSM superpotential. The NMSSM Higgs production cross-sections are calculated using
 233 the SM Higgs production cross-sections $gg \rightarrow H_{SM}$ [32] and $b\bar{b} \rightarrow H_{SM}$ with QCD-improved
 234 (running) Yukawa couplings [33] corrected for differences in coupling between NMSSM and

235 SM using the NMSSMTools [34]:

$$\sigma(gg \rightarrow h_1) = \sigma(gg \rightarrow H_{SM}) \frac{\Gamma(h_1 \rightarrow gg)}{\Gamma(H_{SM} \rightarrow gg)} = \sigma(gg \rightarrow H_{SM}) \frac{Br(h_1 \rightarrow gg)\Gamma^{tot}(h_1)}{\Gamma(H_{SM} \rightarrow gg)} \quad (1)$$

$$\sigma(b\bar{b} \rightarrow h_1) = \sigma(b\bar{b} \rightarrow H_{SM}) \left(\frac{Y_{bbh_1}}{Y_{bbH_{SM}}} \right)^2 \quad (2)$$

(3)

236 where $\sigma(gg \rightarrow H_{SM})$ and $\Gamma(H_{SM} \rightarrow gg)$ are calculated using HIGLU [35], while $Br(h_1 \rightarrow gg)$,
237 $\Gamma^{tot}(h_1)$, and the ratio of Yukawa couplings $Y_{bbh_1}/Y_{bbH_{SM}}$ are obtained using NMSSMTools.

238 3 Analysis selection and efficiencies

239 This section describes details of the event selection, reconstruction, and trigger efficiencies. We
240 first define acceptance selections that ensure well-understood and high-efficiency reconstruc-
241 tion and triggering, and then determine the efficiency of offline and trigger selections for events
242 satisfying acceptance cuts. We then discuss modeling of the shape of the signal invariant mass
243 distribution that will be later be used in the fit and the systematics associated with the accuracy
244 of this shape.

245 3.1 Minimal Acceptance Definition

246 To avoid introducing complicated model-dependent efficiencies, signal regions are defined by
247 kinematic cuts that avoid trigger turn-on curves and regions where detector effects lead to di-
248 minished trigger or reconstruction efficiency. The latter becomes an issue when two or more
249 muons are very close to one another in the muon system. Offline, we use an arbitrated, inside-
250 out muon identification algorithm that minimizes such efficiency losses, discussed further in
251 the text. An event satisfies minimal acceptance requirements if it passes the following selec-
252 tions:

- 253 • at least one reconstructed muon candidate with $p_T > 15 \text{ GeV}/c$ and $|\eta| < 0.9$ per
254 event (ensures high and well-understood trigger efficiency, see Sec. 3.3);
- 255 • at least one additional muon candidate with $p_T > 5 \text{ GeV}/c$ and $|\eta| < 2.4$ (ensures
256 high and well-understood reconstruction efficiency).

257 Events satisfying minimal acceptance requirements are preserved for further analysis and cat-
258 egorization. Additional muon candidates, if present in the event, are used only if they also
259 satisfy the $p_T > 5 \text{ GeV}/c$ and $|\eta| < 2.4$ requirements.

260 3.2 Reconstruction and Efficiency

261 Muons in this analysis are identified by matching tracks in the inner tracker to segments re-
262 constructed in the muon chambers (inside-out), arbitrated such that tracks and segments are
263 used only once. The muon reconstruction algorithm used in many other CMS analyses require
264 a multi-segment muon track to be built in the muon chambers and then matched to a track in
265 the inner tracker (outside-in), but the low segment multiplicity and large multiple scattering in
266 the CMS magnet return yoke makes this method inefficient for muons whose trajectories cross
267 each other in the muon system (as low as 50%, see Appendix A). While this inefficiency is unde-
268 sirable in itself, it is especially problematic for a model-independent analysis, because different
269 models can predict different distributions of muon trajectory overlaps, which would make it
270 impossible to apply a single efficiency correction to all cases. The inside-out muon identifica-
271 tion used in this analysis, however, is much less sensitive to this source of inefficiency.

272 3.2.1 Effects Related to the Muon System and Matching

273 To ensure a high-purity muon sample, we additionally require every muon to have at least two
 274 arbitrated segments², at least eight tracker hits, and a tracker-track $\chi^2/N_{\text{DOF}} < 4$. Although the
 275 cut on arbitrated segments re-introduces a dependence on whether the muon trajectories cross
 276 in the muon system, this inefficiency is still much less severe than the outside-in algorithm.
 277 The arbitrated segments cut also eliminates as many fake muons from accidental overlaps and
 278 punch-through as the outside-in algorithm.

279 An overview of muon reconstruction efficiency with the above algorithm and cuts is presented
 280 in Fig. 5. A Monte Carlo sample of dimuons is generated with flat distributions in dimuon mass
 281 and vector-sum p_T and η , passed through the full CMS detector simulation, and is subject to
 282 the same reconstruction algorithms and cuts as data. The sample is partitioned into “crossing”
 283 muons and “non-crossing” muons by discriminating on angular distance between the muons
 284 at a given depth in the muon system.³ Figure 5 presents three efficiencies: (a) the probability
 285 of reconstructing at least one muon, (b) the probability of reconstructing a specific muon (the
 286 leading muon), and (c) the probability of reconstructing both muons: (c) is approximately the
 287 square of (b), as expected. Inefficiency for crossing muons is maximal for high-momentum and
 288 very forward muons, where trajectories are nearly straight and collinear, allowing for confu-
 289 sion between the candidate muon segments. However, this difference in efficiency reaches an
 290 extreme value of only 7% at $|\eta| = 2.4$, and is only 2% for a distribution uniform in η .

291 Acceptance corrections for each signal region are calculated in Sec. 3.5 using realistic bench-
 292 mark models. A systematic uncertainty of 1.3% (the difference in single-muon efficiency be-
 293 tween the crossing and non-crossing cases) is applied to each $|\eta| < 2.4$ muon, to account for
 294 the unknown fraction of overlapping trajectories in the general case. No such uncertainty is
 295 applied for $|\eta| < 0.9$ muons. Apart from the collective effects related to crossing trajectories,
 296 the single muon reconstruction efficiency is high (of the order of 97-98% efficient, see Fig. 5(b))
 297 and is known to about 0.3% per muon. We apply this systematics uncertainty for each recon-
 298 structed muon. While the overall per muon efficiency is high, the efficiency for reconstructing
 299 a very narrow group of muons has a correlated term due to the dips in efficiency in the gaps
 300 between the wheels (the structure in η seen in Figs. 5(e) and (f)). If a narrow muon jets crosses
 301 one of these gap regions, the efficiency of reconstructing each muon crossing the gap region is
 302 substantially lower (of the order of 92% per muon). Because the efficiency in the gaps is de-
 303 termined by the accuracy in describing the fiducial volumes of the muon chambers, we assign
 304 an additional uncertainty of 1% for every muon in the gap region, which corresponds to a 10%
 305 uncertainty in the accuracy with which simulation describes the size of the gap (corresponds to
 306 about 2 cm, the gap size is about 25 cm). Summarizing, the efficiency and its uncertainty for a
 307 group of N muons in the barrel approximately follows $\epsilon = (0.970 \pm 0.003)^{n_1} \times (0.92 \pm 0.01)^{n_2}$,
 308 where n_1 is the number of muons not crossing the gap and n_2 is the number of muons in the
 309 group that cross the gap ($n_1 + n_2 = N$).

²Arbitration in this case refers to the requirement that a given muon segment can be assigned to only one tracker track, the assignment is done by considering all potential matches among tracker tracks and choosing the most compatible one

³ $\Delta\phi$ = difference in azimuthal angle of the two muon trajectories, each evaluated on a cylinder centered on the beamline with 600 cm radius for $|\eta| < 1$ and one of two transverse planes, 700 cm from the interaction point, for $|\eta| > 1$. Crossing muons have $\Delta\phi < 0.3$ mrad and non-crossing muons have $\Delta\phi > 0.3$ mrad. (See Appendix A for details.)

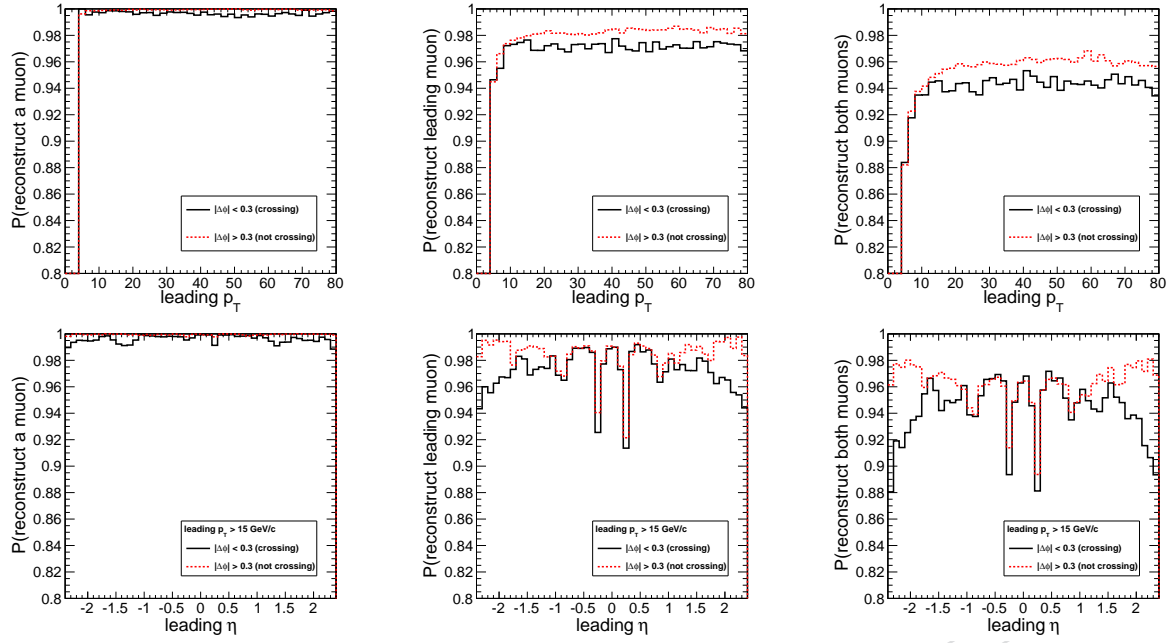


Figure 5: Reconstruction efficiency as a function of momentum (top) and pseudorapidity (bottom), depending on whether the muon trajectories cross in the muon system. All muons in this sample have $p_T > 5$ GeV/c and $|\eta| < 2.4$, and the pseudorapidity plots have at least one muon with $p_T > 15$ GeV/c (see text for details).

3.2.2 Effects Related to Muon Track Reconstruction in the Tracker

For very high momentum muon groups, there is an additional inefficiency associated with the cases when closeness of the track trajectories in the tracker results in one of the tracks not being reconstructed. More precisely, a track is not reconstructed if it shares more than 50% of its hits with other tracks. For reference, with the cluster sizes of the order of 1-2 channels (pixels or strip widths in $r - \phi$) for nearly straight tracks, two opposite sign tracks with $p_T > 300$ GeV/c and nearly parallel at the origin will be within about 1 pixel/strip of each other up to the radius of 60 cm (TOB) acquiring very significant efficiency losses due to hit sharing. While models with such high momentum muon pairs are outside of the kinematic reach of this analysis, tracking inefficiency is not negligible for higher momentum muon jets ($p_T \sim 100 - 300$ GeV/c per group) that may be currently accessible. Because this kinematic limit is per muon group, muon pairs are the most affected at given muon jet p_T as for higher multiplicity muon jets the momentum is shared between multiple muons leading to the lower average muon momenta and decreasing the probability of significant overlaps. E.g. the tracking inefficiency in a quadmuon from $h_d \rightarrow \gamma_d \gamma_d \rightarrow 4\mu$ is generally driven by the inefficiency in reconstructing the muon pair of higher momentum.

To demonstrate effects of tracking efficiency, Fig. 6 shows step-by-step efficiency of reconstructing a pair of muons as a function of p_T of the pair, invariant mass of the pair and η for pairs generated using a pair gun with a flat distribution in $p_T(\mu\mu) = 0 - 500$ GeV/c, invariant mass $m = 2m(\mu) - 0.6$ and $\eta = -0.9 - 0.9$. Ignoring the kinematic thresholds in reconstructing the sample and the unavoidable averaging over non-physical distributions in the sample, it is evident that the p_T dependent effects are driven by the tracker. The shape of the efficiency as a function of the invariant mass is determined by the differences in efficiencies for the “cowboy” (the two tracks bend towards each other in the tracker) and “sailor” (the two tracks bend away from each other) topologies. Depending on the mass and momentum of the pair, tracks in the

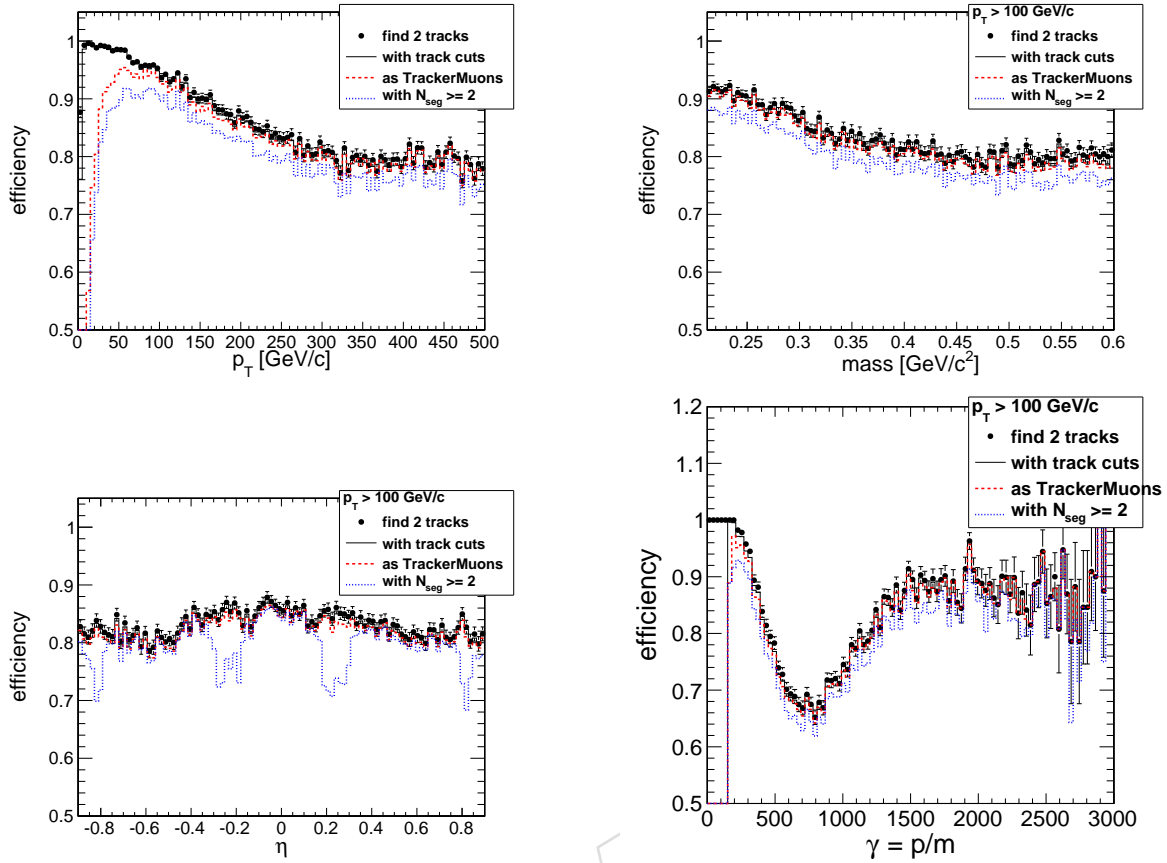


Figure 6: Probability of passing each of the four stages of cuts, given that two muons exist at generator level as a function of muon pair p_T (a), invariant mass $m(\mu\mu)$ (b), η (c), and the relativistic boost γ (d). All distributions were obtained using the dimuon gun with flat distribution in the invariant mass of the pairs from 0.210 to 0.6 GeV/c^2 and $p_T(\mu\mu)$ from 0 to 500 GeV/c .

“cowboy” topology can remain close throughout a substantial portion of the the tracker volume leading to reduced efficiency. For very small masses ($m(\mu\mu) \sim 2m(\mu)$), the difference between the two becomes small as the two tracks are nearly parallel at the origin. Additional and more detailed studies are presented in Appendix N. Because closeness of the two tracks depends both on the invariant mass and the momentum of the pair, a convenient way to present tracking efficiency is to plot it as a function of Lorentz boost $\gamma = p(\mu\mu)/m(\mu\mu)$ shown in Fig. 6(d). The increase in the efficiency at high γ is because that region is populated by pairs with high momentum and low invariant mass $m(\mu\mu) < 0.3 \text{ GeV}/c$ where the two tracks are nearly parallel, in which case the tracks in the “cowboy” topology at the origin intersect at smaller radii and frequently become effectively “sailors” in the tracker. Generally, the onset of inefficiency starts earlier in $p_T(\mu\mu)$ for “cowboys” than for “sailors” as at a fixed momentum tracks in the “cowboy” topology tend to stay close longer.

As it was mentioned already, the dominant factor in the efficiency is the extent to which the two tracks overlap (and share hits) within the tracker volume. While this is a purely geometric effect, small systematic differences between the simulation predictions and the data if the sizes of the track hits (clusters) in the tracker could lead to a systematic deviation in the tracking efficiency in simulation. The proper procedure to evaluate this effect, while technically complicated, would be to modify the size of the hits in tracker simulation by $\pm 20\%$ (a

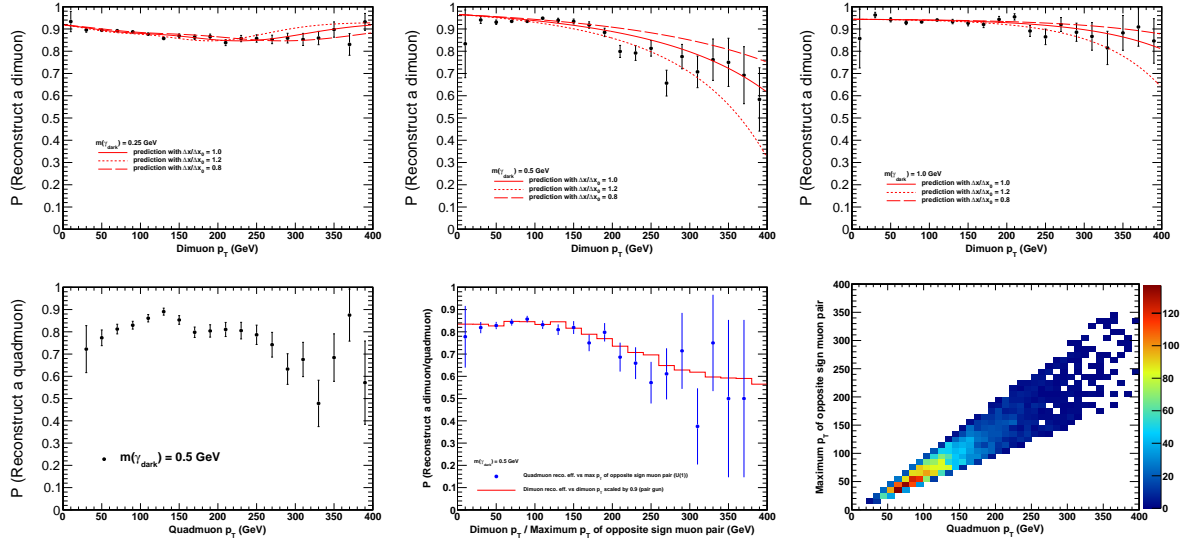


Figure 7: (a,b,c): Illustration of estimating the systematic uncertainty in tracking efficiency by fitting the efficiency of findinga dimuon pair to a smooth curve $\epsilon(p_T)$ and using curves $\epsilon'(p_T) = \text{eps}((1 \pm 0.2)p_T)$ to estimate the systematic uncertainty in tracking efficiency. Varying p_T within 20% approximately corresponds to varying the hit (cluster) size in tracker simulation by 20%. Fits are performed separately for “cowboy” and “sailor” topologies and then combined in the plots for $m(\mu\mu) = 0.25$ (a), 0.5 (b), and $1.0 \text{ GeV}/c^2$ (c). (d): Efficiency of finding a “quadmuon” from $h_d \rightarrow \gamma_d \gamma_d \rightarrow \mu\mu\mu\mu$ as a function of $p_T(\mu\mu\mu\mu)$, (e): the same efficiency plotted as a function of $p_T^{\max}(\mu\mu)$ of the higher momentum muon pair overlaid with the efficiency of a singlle dimuon scaled to match the quadmuon efficiency at lower $p_T(\mu\mu)$ showing that the tracking part of quadmuon efficiency finding is driven by the track finding efficiency of the higher momentum pair, (f): distribution of p_T^{\max} of the higher momentum pair in a quadmuon versus quadmuon $p_T(\mu\mu\mu\mu)$ showing that on average $p_T^{\max} \sim 2/3 p_T(\mu\mu\mu\mu)$.

very conservative figure) and re-measure the efficiency. A more simple, but nearly identical approach is instead of increasing the size of the hits to “push” the two trajectories closer by the same 20% and remeasure efficiency. Because the distance between the tracks scales with $1/\gamma = m(\mu\mu)/p(\mu\mu)$, this can be accomplished by comparing the efficiency for a given dimuon mass and $p_T(\mu\mu)$ points with efficiency at points with $p'_T = (1 \pm 0.2)p_T(\mu\mu)$ and assigning the difference as the systematic uncertainty in tracking efficiency. Figures 7(a),(b), and (c) show the efficiency of finding a dimuon pair (it also includes effects related to muon system in addition to tracking effect, but that inefficiency is nearly independent of momentum) for $m(\mu\mu) = 0.25$, 0.5 and $1 \text{ GeV}/c^2$. It also demonstrates the procedure for estimating the systematics uncertainty by shifting the efficiency curve by $\pm 20\%$ in muon pair p_T to account for possible deviations in track cluster sizes in the tracker simulation. Efficiency for $m(\mu\mu) > 1 \text{ GeV}/c^2$ is similar to what it is for $m(\mu\mu) = 1 \text{ GeV}/c^2$.

For the models of interest, the efficiency of finding each muon pair in a higher multiplicity muon jet is nearly independent of other pairs because the closest tracks are always those originating from the lowest mass dimuon resonance. Accidental substantial overlaps of the trajectories of muons from different nearby resonances are rare and do not dominate the uncertainty. In particular, the efficiency of reconstructing a “quadmuon” (shown in Fig. 7(d)) is essentially a product of reconstruction efficiencies of the two dimuons within the quadmuon and is dominated by the probability to reconstruct the higher momentum pair. This observation is

372 illustrated in Fig. 7(e) showing the quadmuon efficiency plotted as a function of the higher mo-
 373 mentum dimuon within the quadmuon overlaid with the reconstruction efficiency of a single
 374 dimuon of the same momentum (the latter is scaled to agree with the quadmuon efficiency at
 375 low p_T to remove the offset due to the efficiencies related to reconstructing the muons in the
 376 second pair in the muon system). Finally, Fig. 7 shows the transverse momentum of the more
 377 energetic dimuon within the quadmuon versus transverse momentum of the quadmuon. One
 378 can conclude that $p_T^{\max}(\mu\mu) \sim p_T \mu\mu\mu\mu$ allowing a simple translation of the tracking related
 379 part of the dimuon reconstruction efficiency and systematics into the reconstruction efficiency
 380 and systematics for the quadmuon. The same logic applies to higher multiplicity muon jets, but
 381 note that kinematically accessible higher multiplicity muon jets will have on average lower mo-
 382 mentum of constituent dimuons leading generally to higher overall reconstruction efficiency.
 383 This is because the same energy is essentially divided between higher number of dimuons.
 384 We also re-iterate our conclusion that the reconstruction efficiency for dimuons in events with
 385 nearby track pairs (e.g. in $h_d \rightarrow \gamma_d \gamma_d \rightarrow \mu^+ \mu^- e^+ e^-$) is essentially the same as for standalone
 386 dimuons.

387 Summarizing, we assign a systematic uncertainty due to tracking using plots in Fig. 7. For
 388 reference, for $p_T = 150 \text{ GeV}/c$, the systematic uncertainty for dimuon reconstruction efficiency
 389 due to tracking is 2.5, and 2% for $m(\mu\mu) = 0.25, 0.5$ and $1.0 \text{ GeV}/c^2$, respectively. For quad-
 390 muons of $p_T = 150 \text{ GeV}/c$, the tracking uncertainty is under 2% independent of mass and is
 391 approximately corresponds to dimuon efficiency at $p_T = 100 \text{ GeV}/c$ ($2/3$ of the quadmuon p_T).
 392 For higher multiplicity lepton jets, the uncertainty is taken from the quadmuon case, which is a
 393 conservative estimate. These figures are used to estimate the efficiency for more complex event
 394 topologies with multiple muon jets, in which case the uncertainties for each lepton jet are taken
 395 to be 100% correlated.

396 3.3 Trigger Selections

397 Trigger choice is an important consideration for this analysis because the presence of nearby
 398 muon hits can potentially affect trigger performance. Indeed, it was found that the trigger is
 399 substantially inefficient for muons whose trajectories cross in the muon endcap, though not the
 400 barrel. The non-isolated, single-muon trigger response is studied in the same way as Sec. 3.2,
 401 and presented in Fig. 8(a). See Appendix B for an explanation of why we chose non-isolated
 402 and single-muon triggers only. As described in Sec. 3.2, inefficiencies that depend on whether
 403 the muon trajectories cross are undesirable in a model-independent analysis. For this reason
 404 and because of the many changes in the Endcap Level 1 ghost cancellation parameters during
 405 the data taking period, events were required to be triggered in the barrel ($|\eta| < 0.9$). The
 406 lowest-threshold, unprescaled trigger also changed from 9 to 15 GeV/c during the data-taking
 407 period, so we select events with the 15 GeV/c when available and simulate it by requiring a
 408 trigger candidate of at least 15 GeV/c for data before its introduction.

409 While the above selections ensure robust L1 trigger performance, the correlated muon effects
 410 may potentially introduce inefficiencies at the level of the High Level Trigger (HLT). Because
 411 muon reconstruction in the HLT closely follows the global muon reconstruction used in the
 412 offline, the trigger efficiency can potentially suffer from correlated effects due to the presence
 413 of nearby muon segments. Such inefficiency would have caused a substantial effect on this
 414 analysis should we required two reconstructed trigger muon candidates, however we only
 415 require one muon to be reconstructed, so the efficiency of finding the higher p_T muon remains
 416 high; see Fig. 8(b).

417 Because the barrel muon trigger efficiency does not suffer from the correlated effects observed

in the endcap to any significant degree, the trigger efficiency is calculated using simulation and corrected with a uniform scale factor of 0.968 ± 0.004 per event is obtained from $Z \rightarrow \mu\mu$ data and simulation using a tag-and-probe technique (see Appendix C).

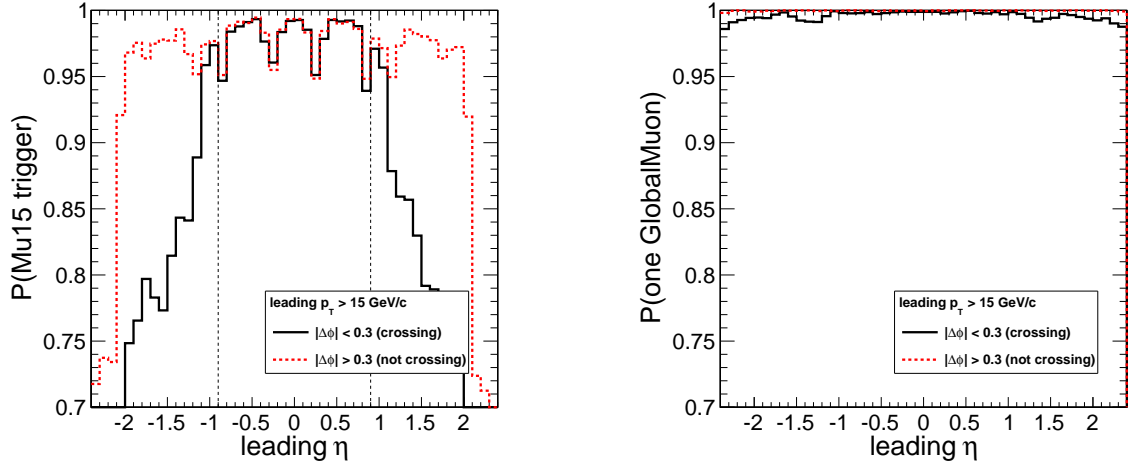


Figure 8: Left: non-isolated, single-muon, $p_T > 15 \text{ GeV}/c$ trigger efficiency (L1 and HLT). Right: probability of finding one $p_T > 15 \text{ GeV}/c$ GlobalMuon (algorithm used by the HLT).

421 3.4 Modeling of the Signal Dimuon Resonance Mass Spectrum

Because the new resonances decay to Standard Model particles only and the coupling to SM is weak, they have narrow width and the shape of the di-muon invariant mass distribution is fully determined by the detector resolution and final-state radiation of a photon from one of the muons. Though extreme precision in modeling these shapes is not required in the presence of nearly zero backgrounds, it has to be reasonably well-understood if we need to quantify properties of the new resonances, assuming they are discovered.

The Standard Model provides four narrow, high cross-section dimuon resonances in our mass range of interest, ω , ϕ , J/ψ , and ψ' , which we use to calibrate the signal lineshapes. We study the resolution of each of these resonances in data using a suitably defined function (Crystal Ball with separate core resolutions for the barrel and the endcap) and find a good agreement with the expectation based on simulation predictions (see details in Appendix D).

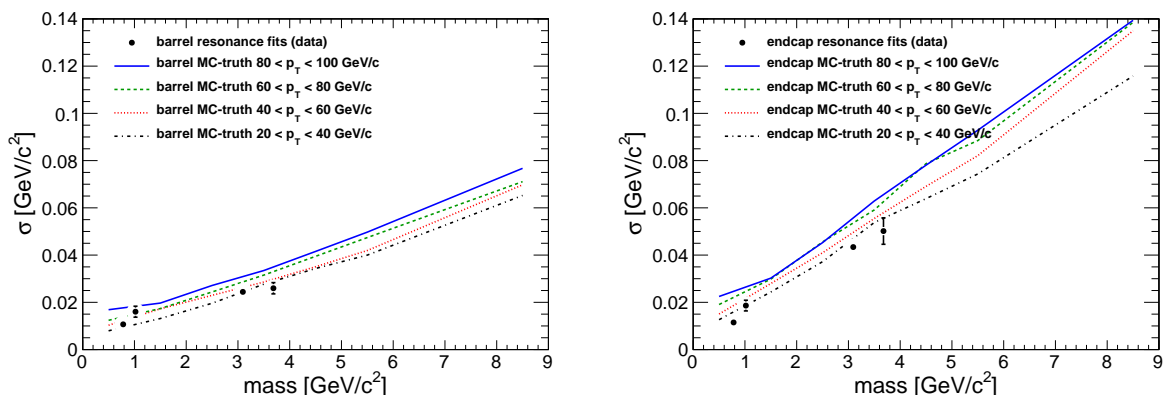


Figure 9: Left: resolution as a function of mass for simulated muons (lines) and real resonances (points) in the barrel region $|\eta| < 0.9$ as obtained using the fit to a Crystal Ball shape. Right: the same distributions for the overlap and endcap region $|\eta| > 0.9$.

433 To study the systematics effects, we note that the resolution of the low mass resonances de-
434 pends on the mass of the resonance, momentum (boost) of the resonance and also have an
435 η -dependent component associated with lower resolution in the forward region. Figure 9(a)
436 shows the dependence of the core resolution on dimuon p_T and resonance mass, overlaid with
437 the results of the fits in data for regions with $|\eta| < 0.9$ and $|\eta| > 0.9$ (note that the momenta of
438 resonances in data typically fall into the lowest bin, $p_T = 20\text{--}30 \text{ GeV}/c$). Because the data and
439 simulation agree well, we conservatively use the spread due to the dimuon p_T shown in the
440 figure as the systematic uncertainty for the core resolution parameter σ . The mean value used
441 corresponds to the middle of the band and evolves with the mass of the resonance according
442 to the dependency shown; the dimuon p_T dependency is not included for simplicity. Note that
443 while one of the muons in the distribution is typically a trigger muon, these resolutions are
444 dominated by the tracker performance and are independent of the trigger: the trigger modifies
445 the acceptance and efficiency, but this is not an issue for the shapes of the resonances.

446 We use these studies to define the signal regions in the multi-dimensional space of dimuon
447 invariant masses as a “corridor” near the diagonal with the width of 5σ in detector resolution
448 in each direction, where $\sigma(m, p_T) = 0.026 + 0.0065m$ for the barrel and $\sigma(m, p_T) = 0.026 +$
449 $0.013m \text{ GeV}/c^2$ for the endcap.

450 **3.5 Complete Acceptance, Event Categorization and Selection Efficiencies**

451 To simplify interpretation of the model-independent results and allow for a comparison with
452 specific theoretical models, we calculate acceptance and efficiencies at the generator level and
453 the fully-reconstructed level for each signal region. The acceptance is representative of geomet-
454 ric and kinematic cuts while the efficiency quantifies losses due to reconstruction and trigger
455 effects. Acceptances predicted by simulation are corrected for systematic effects obtained from
456 comparisons with data using appropriate scale factors and uncertainties and are propagated
457 into the experimental reported acceptances. This is convenient because corrections for recon-
458 struction and trigger efficiencies are much less dependent on the kinematics of the events and
459 a comparison to different models can be obtained by recalculating acceptance at the generator
460 level and adjusting the limit by the ratio of acceptances for a new model and one of our models.

461 Table 2 lists acceptances and efficiencies of the event selections and categorization into signal
462 regions for several representative benchmark scenarios. The upper part of the table serves
463 mostly as an illustration and shows cumulative efficiencies for applying the minimal accep-
464 tance (which is actually applied in this analysis) and shows how the acceptance would reduce
465 if one were to require additional muons in the event (these selections were not applied). Each
466 line in the upper part of the table shows the fraction of events satisfying given requirement
467 and all previous requirements. The bottom part of the table shows actual reconstruction level
468 acceptances for each of the topologies used in this analysis. These are defined relative to all
469 signal events generated (i.e. they already include minimal acceptance). The overall acceptance
470 for all topologies is therefore a sum of individual acceptances for each topology. Furthermore,
471 because the regions are not overlapping, the sum of acceptances for each of the topologies with
472 a given number of muons should be roughly equal to the efficiency of requiring the same num-
473 ber of muons in the upper part of the table. The difference is due to failures in reconstruction or,
474 for the single dimuon region (a-1), is due to the additional kinematical requirement of a highly
475 boosted dimuon $p_T > 80 \text{ GeV}/c$ not applied in the upper part of the table.

Table 2: Illustration of the acceptances and efficiencies of the event selections and categorization into signal regions for several representative benchmark scenarios. The upper part of the table serves mostly as an illustration and shows cumulative efficiencies for applying the minimal acceptance (which is actually applied in this analysis) and shows how the acceptance would reduce if one were to require additional muons in the event (these selections were not applied). Each line in the upper part of the table shows the fraction of events satisfying given requirement and all previous requirements. The bottom part of the table shows actual reconstruction level acceptances for each of the topologies used in this analysis. These are defined relative to all signal events generated (i.e. they already include minimal acceptance). The overall acceptance for all topologies is therefore a sum of individual acceptances for each topology. Furthermore, because the regions are not overlapping, the sum of acceptances for each of the topologies with a given number of muons should be roughly equal to the efficiency of requiring the same number of muons in the upper part of the table. The difference is due to failures in reconstruction or, for the single dimuon region (a-1), is due to the additional kinematical requirement of a highly boosted dimuon $p_T > 80 \text{ GeV}/c$ not applied in the upper part of the table. Acceptances for regions (a-2) and (b-1) refer to the near-diagonal signal region only (within 5σ in detector resolution: $\sigma(m) = (0.026 + 0.0065 b m) \text{ GeV}/c^2$, where $b = 1$ for barrel and $b = 2$ for endcap.).

Selections	NMSSM	$U(1)$	$n_2(\rightarrow n_1\gamma_D)$	$n_2 \rightarrow n_1 h_D(\rightarrow 2\gamma_D)$
Minimal Acceptance:				
$p_{T_1} > 15 \text{ GeV}/c$ & $ \eta_1 < 0.9$	58.0	88.2	77.2	81.0
$p_{T_2} > 5 \text{ GeV}/c$ & $ \eta_2 < 2.4$	55.4	88.0	76.3	80.9
Additional Muons with $\eta < 2.4$:				
$p_{T_3} > 5 \text{ GeV}/c$	48.3	86.1	69.5	80.5
$p_{T_4} > 5 \text{ GeV}/c$	26.9	78.6	48.5	78.4
$p_{T_5} > 5 \text{ GeV}/c$	0.1	55.1	5.7	73.4
$p_{T_6} > 5 \text{ GeV}/c$	0.0	35.1	0.6	63.4
Categorization and Trigger				
(a-1) accept. [%] & trig. eff.	1.7 1.7	7.8 7.4	17.4 —	0.9 —
(a-2) accept. [%] & trig. eff.	0.0 0.0	5.5 5.1	0.9 —	6.6 —
(a-3) accept. [%] & trig. eff.	0.0 0.0	2.5 2.3	0.0 —	3.7 —
(b-1) accept. [%] & trig. eff.	24.9 23.8	15.7 15.4	40.6 —	0.7 —
(b-2) accept. [%] & trig. eff.	0.0 0.0	44.4 42.8	0.2 —	59.2 —
(c-1) accept. [%] & trig. eff.	0.0 0.0	0.1 0.1	0.1 —	0.2 —

476 4 Background estimation

477 In this analysis, the background estimation in the signal regions is obtained by fitting the (gen-
 478 erally multi-dimensional) spectrum of dimuon masses in data to a sum of signal and back-
 479 ground templates with either both signal and background normalizations floating (for the
 480 topology with exactly one dimuon) or the signal normalization floating and the background
 481 normalization constrained in the off-diagonal side-band region of multi-dimensional distribu-
 482 tion of dimuon invariant masses. Modeling of the signal shape is discussed in Sec. 3.4, and
 483 the shapes of the distributions for backgrounds are modeled by using appropriately selected
 484 background-enriched samples, described below.

485 Because signal regions are expected to have near-zero background contamination, our final
 486 results only weakly depend on possible imperfections in modeling the background shape pre-
 487 dictions. However, interpretation of a possible discovery motivated us to perform a thorough
 488 study of the dimuon mass distributions and careful consideration in constructing the back-
 489 ground templates used in the fit. The shape templates for background mass distributions are
 490 derived from background-enriched samples, in which Standard Model sources dominate over
 491 any potential signals. These samples must have the same Standard Model physics content as
 492 the corresponding signal regions, which requires a thorough understanding of the background
 493 data. We validate our techniques and check for possible biases using data in suitably defined
 494 control regions, still dominated by Standard Model sources, but closer to the signal in event
 495 kinematics.

496 4.1 Features of low-mass dimuon spectrum

497 To investigate the features of the low-mass single-dimuon spectrum ($0.25 < m_{\mu\mu} < 5 \text{ GeV}/c^2$),
 498 we use events in data satisfying minimal acceptance requirements and trigger selections (de-
 499 scribed in Sec. 3.1). To avoid unblinding any of the signal regions, we require events to have no
 500 additional analysis-quality muon candidates ($p_T > 5 \text{ GeV}/c$ and $|\eta| < 2.4$), and the transverse
 501 momentum of the dimuon must be less than $80 \text{ GeV}/c$.

502 The selected region contains events from several Standard Model processes. The largest con-
 503 tribution is from QCD multi-jet production, including J/ψ , ψ' , ϕ , ρ/ω , and η (decays to $\mu\mu\gamma$)
 504 resonances from both light- and heavy-flavor hadronization, double-semileptonic decay chains
 505 from b -flavored hadrons, as well as events with kaon and pion decays-in-flight and various
 506 types of misidentified muons. The second source is prompt production of the resonances, fol-
 507 lowed by low-mass Drell-Yan.

508 To simulate these Standard Model processes, we use the following Monte Carlo samples:

- 509 • inclusive-muon sample skimmed off the Pythia 6 QCD $2 \rightarrow 2$ sample that has $\hat{p}_T >$
 510 $30 \text{ GeV}/c$, which we divide into three exclusive partitions:
 - 511 • $b\bar{b}$ with one b -quark decaying to $\mu\mu X$ by double-semileptonic decay or
 512 dimuon resonances (both muons have the same b -flavored hadron as a
 513 common ancestor in the generator-level decay tree);
 - 514 • muons from light-flavor hadronization and muons that are unassociated
 515 with one another, excluding misidentified muons and decays-in-flight;
 - 516 • dimuons with at least one misidentified muon and/or decay-in-flight of
 517 a charged pion, charged kaon, or strange baryon;
- 518 • prompt $J/\psi \rightarrow \mu\mu$, $\psi' \rightarrow \mu\mu$, and $\psi' \rightarrow J/\psi \pi\pi \rightarrow \mu\mu \pi\pi$, produced with Pythia 6,
 519 decayed with EvtGen (including final state QED radiation);

- 520 • Drell-Yan, generated using Pythia 8 including pile-up (with no explicit low-mass
 521 cut-off except that used internally by Pythia).

522 Figure 10(a) shows a “raw” mass spectrum overlaid with the “out-of-the-box” Monte Carlo pre-
 523 dictions using the above samples, scaled to the integrated luminosity of the dataset (35 pb^{-1}).
 524 While there is an excellent general agreement, one can note several features associated with
 525 known deficiencies in generating the MC samples, e.g. the QCD multi-jet sample is missing ω
 526 and ψ' resonances, and the prompt/Drell-Yan MCs are missing the ω . Because this analysis
 527 will use templates obtained by fitting actual data distributions, these deficiencies are not a con-
 528 cern as long as the origin of the discrepancies is understood. In addition, there is an excess near
 529 the low-mass edge of the spectrum not explained by the MC.

We undertake additional studies to further our confidence in understanding the sample composition. This can be important if the relative fractions of the components present in the low-mass dimuon spectrum depend strongly on the selections used in the analysis. We first divide the data into two subsamples enriched with $b\bar{b}$ and non- $b\bar{b}$ contributions, respectively. We use absolute track isolation Iso and transverse vertex displacement L_{xy} (see Appendix E for definitions) to define the following “ $b\bar{b}$ cuts,”

$$b\bar{b}\text{-like if } (Iso > 4.5 \text{ GeV}/c \text{ or } L_{xy} > 2 \text{ mm}), \quad (4)$$

530 and we also define the “anti- $b\bar{b}$ cuts” by inverting this requirement.

531 The invariant mass distributions for the $b\bar{b}$ -enriched and the $b\bar{b}$ -depleted sub-samples is shown
 532 in Figs. 10(b) and (c). The comparison affirms our observation that the inclusive-muon sample
 533 simulation is missing ω and ψ' resonances, while the prompt/Drell-Yan is missing the ω . Note
 534 that most of the dimuons arising from misidentified muons and decays-in-flight pass the $b\bar{b}$ cut
 535 as these are typically produced inside jets and therefore are not well isolated. The fraction of
 536 these events comprises about 25% of the events with $m_{\mu\mu} < 1 \text{ GeV}/c^2$. Below $0.5 \text{ GeV}/c^2$, there
 537 is a low-mass rise not described by the Monte Carlo, and this distribution is too wide to be a
 538 detector resolution-dominated $\mu\mu$ resonance. This is discussed in further detail in Appendix E
 539 where it is shown that a large fraction of these events is due to the not simulated very low
 540 mass Drell-Yan with the topology of two very close and nearly parallel muon tracks causing a
 541 poorly measured secondary vertex position and leading to L_{xy} large enough to pass the “ $b\bar{b}$ ”
 542 selections.

543 4.2 Background Mass Spectrum in Region (a-1): High- p_T Dimuons

544 The (a-1) signal region is defined as exactly one dimuon with the transverse momentum $p_T^{\mu\mu} >$
 545 $80 \text{ GeV}/c$. For sufficiently high $p_T^{\mu\mu}$ (away from threshold effects), the composition of the Stan-
 546 dard Model backgrounds, and therefore the invariant mass distribution of the single-dimuon
 547 sample, is weakly dependent on $p_T^{\mu\mu}$. To show that the composition of the samples does
 548 not change substantially, Fig. 11 compares the $p_T^{\mu\mu}$ distribution for three sub-classes of single-
 549 dimuon events: (i) non- J/ψ events passing the $b\bar{b}$ cuts, (ii) J/ψ events passing the $b\bar{b}$ cuts, and
 550 (iii) events failing the $b\bar{b}$ cuts. J/ψ events are selected with a $0.15 \text{ GeV}/c^2$ -wide mass window
 551 around the PDG J/ψ mass. For $p_T^{\mu\mu} > 40 \text{ GeV}/c$, all three distributions are exponential with
 552 mutually consistent decay length scales. To show that the shape of the distribution is weakly
 553 dependent on $p_T^{\mu\mu}$, Fig. 11(b) shows the inclusive-muon MC mass distributions in $20 \text{ GeV}/c$
 554 bins of $p_T^{\mu\mu}$ from 40 to 120 GeV/c . We conclude that the mass spectrum of the background
 555 events is negligibly dependent on $p_T^{\mu\mu}$.

556 Based on the above observations, the (a-1) background template is obtained by fitting the

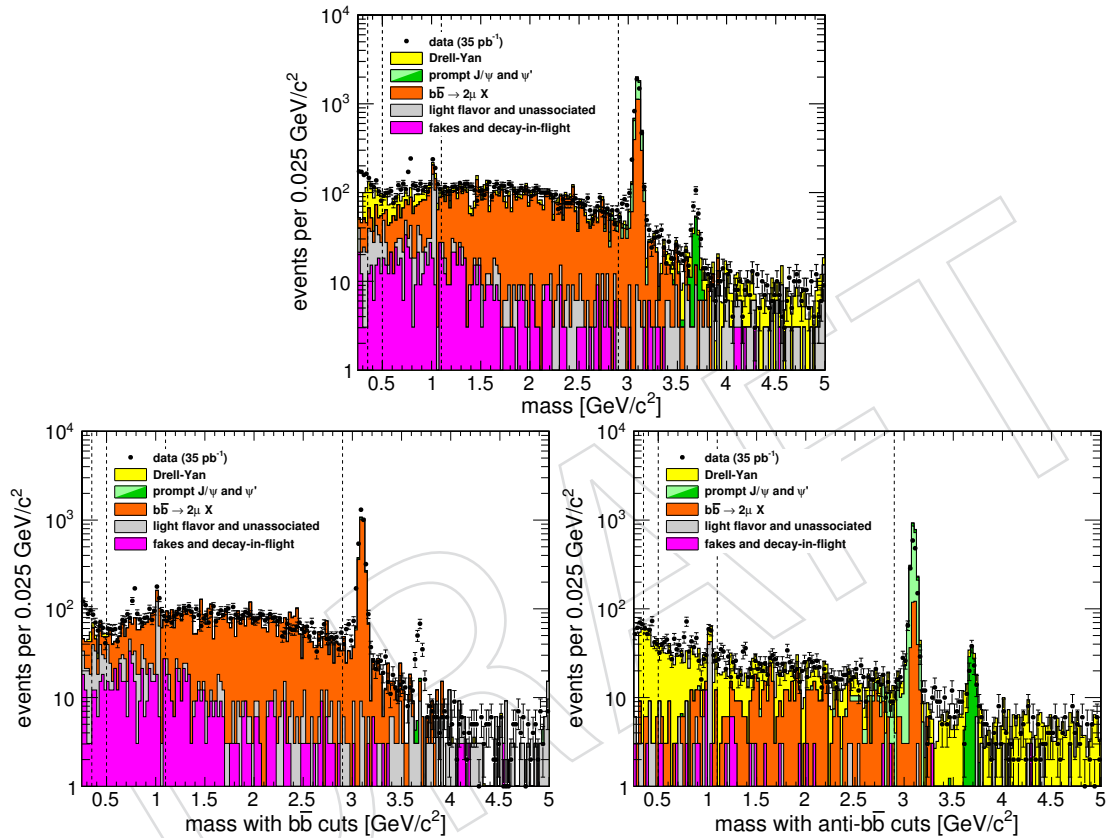


Figure 10: (a): Mass distribution of single-dimuon events with Monte Carlo simulations superimposed. (b) and (c): The same distribution for the samples enriched with $b\bar{b}$ events (b) and depleted of $b\bar{b}$ events (c).

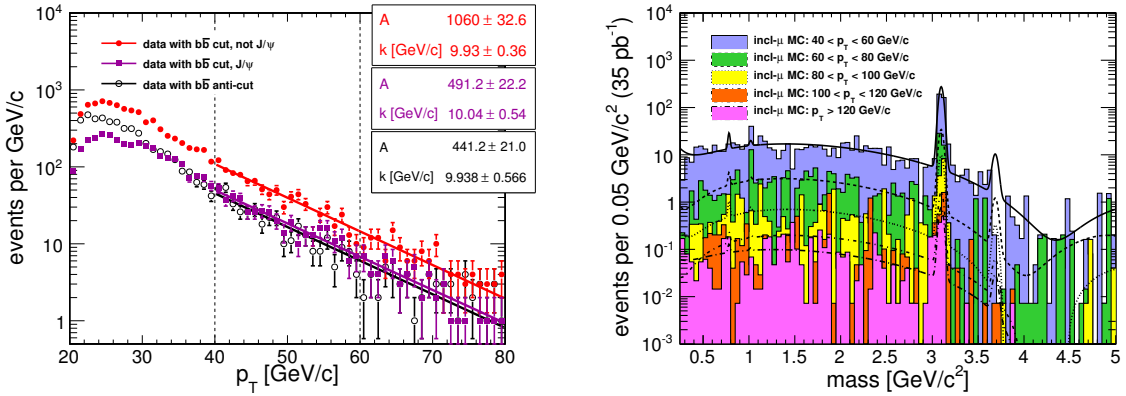


Figure 11: Scaling of single-dimuon data with p_T . Left: p_T spectra for three non-overlapping subsamples of dimuons ($\propto \exp(-x/k)$, normalized by A , the integral from 40 to 80 GeV/c). Right: Mass distribution of inclusive-muon MC in bins of p_T from 40 to 120 GeV/c .

557 dimuon invariant mass distribution using events with $40 < p_T^{\mu\mu} < 60 \text{ GeV}/c$ (the background-
558 enriched sample). We additionally define a control region, $60 < p_T^{\mu\mu} < 80 \text{ GeV}/c$ for validation.

The template shape is obtained by fitting the mass distribution in the background-enriched region to a parametric function using an unbinned likelihood fit. For uniformity, we use the same function for this and all other background template fits, although we reduce the number of fit parameters when warranted.

$$\begin{aligned} BG(m; p_\omega, p_\phi, p_{J/\psi}, p_{\psi'}, \alpha_{J/\psi}, \sigma_{J/\psi}, p_{1/m^2}, p_{poly}, p_1, \dots, p_n) = \\ p_\omega G(m; 0.78265, 0.011) + p_\phi G(m; 1.019455, 0.014) + \\ p_{J/\psi} CB(m; 3.096916, \sigma_{J/\psi}, \alpha_{J/\psi}) + p_{\psi'} G(m; 3.68609, 0.029) + \\ p_{1/m^2} 1/m^2 \left(\int_{0.25}^{5.0} 1/m^2 dm \right)^{-1} + p_{poly} B(m; p_1, \dots, p_n), \quad (5) \end{aligned}$$

559 where ω , ϕ , and ψ' resonances are parameterized using $G(m; m_0, \sigma)$, a Gaussian normalized to a
560 unit integral in the region $0.25 < m < 5 \text{ GeV}/c^2$. For each, m_0 is fixed to the corresponding PDG
561 mass and σ (resolution) is fixed to the resolution obtained in Sec. 3.4. The J/ψ resonance shape
562 is parameterized with a Crystall Ball function $CB(m; m_0 = 3.096916, \sigma_{J/\psi}, \alpha_{J/\psi})$, normalized
563 to unit area in $0.25 < m < 5 \text{ GeV}/c^2$. The $\sigma_{J/\psi}$ and $\alpha_{J/\psi}$ parameters are allowed to float
564 in fits. The bulk shape is described using $B(m; p_1, \dots, p_n)$, a series expansion in the Bernstein
565 polynomial basis⁴ of degree n . The $1/m^2$ term describes the low-mass Drell-Yan. The $p_\omega, p_\phi,$
566 $p_{J/\psi}, p_{\psi'}, p_B$, and p_{1/m^2} parameters are normalization factors for the resonances, bulk and the
567 $1/m^2$ components, respectively, and are obtained from the fit.

568 Figure 12(a) shows the background template obtained by fitting the data from the background-
569 enriched region. The band indicates the spread in the fitted shape due to variations of fitted
570 parameters within the measured values. To verify our assumption that the shape of the back-
571 grounds is not changing substantially with $p_T^{\mu\mu}$, Fig. 12(b) shows the same template overlaid
572 with the data in the control region $60 < p_T^{\mu\mu} < 80 \text{ GeV}/c$, showing good agreement (only the
573 normalization of the template is scaled to data).

⁴E.g., see <http://www.idav.ucdavis.edu/education/CAGDNotes/Bernstein-Polynomials.pdf>. Bernstein basis polynomials are positive-definite, thus, by providing n non-negative coefficients we can get a well behaving p.d.f. approximation. We use RooFit's implementation for Bernstein basis polynomials.

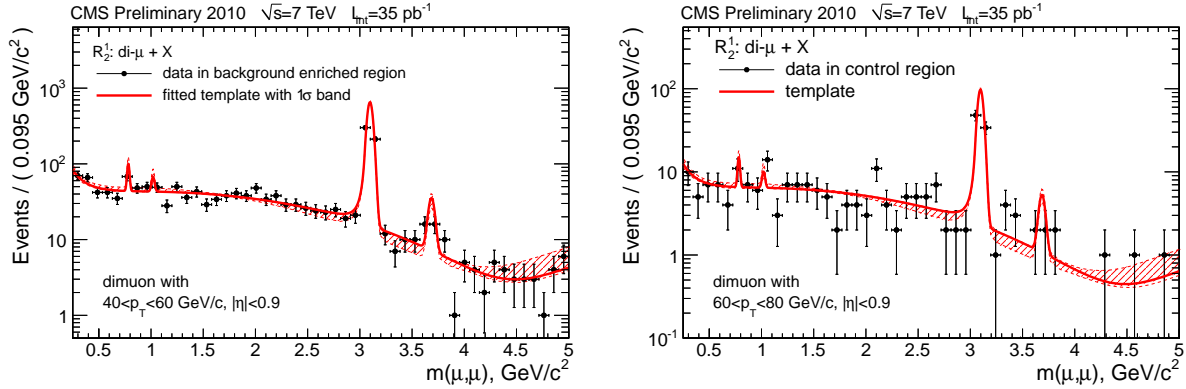


Figure 12: Left: fit of the (a-1) background-enriched data to Eqn. 5. Right: overlay of the same shape on the corresponding control region.

4.3 Background Spectrum for (a-2) and (a-3): high-multiplicity mu-jets

The (a-2) signal region consists of exactly one neutral mu-jet with two fundamental dimuons (four muons), with the final fit being performed in a 2D space formed by the masses of the two dimuons in the event. The signal, if present, would occupy the region near the diagonal. The (a-3) region is exactly one mu-jet with more than four muons and therefore the dimensionality of the space can be greater than two. Standard Model processes yielding four nearby real muons are extremely rare (primarily boosted $b\bar{b}$); thus the events in these regions are dominated by events with typically two real muons and the rest being either misidentified muon candidates or decays-in-flight produced in the same jet (and therefore having a very soft spectrum). In some of these events, one of the dimuons is composed of true muons and the other of misidentified muons, while in others, both dimuons contain one true muon and one misidentified muon. Both of these sources have to be correctly modeled.

Muon misidentifications are primarily rare failures of the muon identification procedure, in which muon chamber segments from one real muon are assigned to two distinct tracks in the tracker. Decays-in-flight are $\pi^\pm \rightarrow \mu^\pm \nu$, $K^\pm \rightarrow \mu^\pm \nu$, and (less frequently) strange baryons producing a muon far from the primary and secondary vertices. Because both types of backgrounds originate from tracks in jets, dimuons with either misidentified or decay-in-flight muons typically have similar low-mass distributions peaking at $1 \text{ GeV}/c^2$, as verified in Monte Carlo studies (see Appendix F.1 for more details). Based on these considerations, we conclude that there is no need to make a distinction between these two types of backgrounds.

To model the dimuon mass spectrum in the signal region, we use data events with exactly two analysis-quality muon candidates forming a mu-jet. We continue building the mu-jet by adding tracks as though they were muon candidates, using our standard mu-jet clustering algorithm. To be added to such a “pseudo-mu-jet,” a track has to possess exactly the same properties as analysis-quality muon candidates, except for muon chamber segments. We then split the pseudo-mu-jet into fundamental dimuons in the standard way and assign them either to category (a-2) or (a-3). Background-enriched samples obtained this way possess exactly the same kinematics as events in the corresponding signal region. Within each category, we define two subsamples: one in which both identified muons were assigned to the same dimuon (33% of events) and the other with each muon assigned to a different dimuon (the remaining 67%).

For the first subsample, the 1D invariant mass distributions of the “true” dimuon and the “fake” dimuon are fitted using the same generic parametrization as in other cases (Eqn. (5)), as illustrated in Fig. 13(a,b). The 2D background template for this kind of event is obtained as a

607 Cartesian product of 1D invariant mass templates for the true and fake dimuons, symmetrizing
 608 the distribution, i.e. $f(m_1, m_2) = \frac{1}{2}(f_{\text{true}}(m_1)f_{\text{fake}}(m_2) + f_{\text{true}}(m_2)f_{\text{fake}}(m_1))$. When selecting
 609 signal events, we would not know which dimuon is real, so the order of dimuons in the event
 610 is randomized.

611 For the second subsample with “mixed” dimuons, we separately fit the 1D invariant mass
 612 distributions for the “triggered” dimuon, containing at least one triggerable muon, and the
 613 “other” dimuon in the event. Because the two distributions were found to be identical, we
 614 combine them into a single distribution, see Fig. 13(c). The 2D template for “mixed” events
 615 is obtained by creating a Cartesian product of the 1D distributions, followed by symmetrizing
 616 the distribution. Finally, the two 2D templates for the two sources of background events are
 617 added with weights proportional to the number of events in the two subsamples (the statistical
 618 uncertainty in the relative fraction is negligible compared to other uncertainties).

619 As expected, the plots in Fig. 13 show that resonances are present only in the true dimuon
 620 spectrum and the distributions for misidentified and mixed dimuons have the characteristic
 621 continuum shape. In all cases, the data are overlaid with the parameterized shapes, fitted to
 622 the data using the functional form from Eqn. (5). The spread of the fit curves corresponds to
 623 the uncertainties in the fit. The full correlation matrix of the fitted parameters is saved with the
 624 function and used in the fit of the signal region.

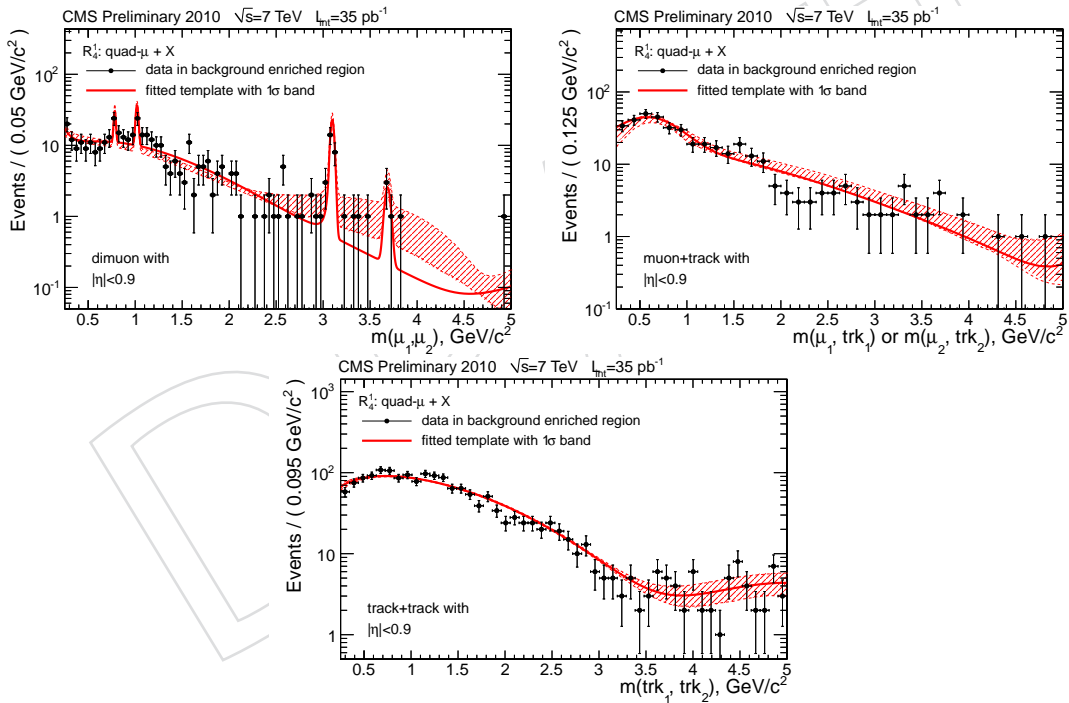


Figure 13: (a) Invariant mass of true dimuons (in which both muons are fully identified as muons). (b) Same for fake dimuons (both are non-muon tracks playing the role of misidentified muons). (c) Same for the dimuons in mixed events (one non-muon track in each dimuon). The last category is not divided into sub-samples for the dimuons containing a trigger quality muon or not as the distributions show no significant difference. Parameterized functions are obtained from fits of these distributions and are used to construct the final 2D background template for the (a-2) and (a-3) signal regions.

625 To validate this technique, we create a control sample from events with exactly three analysis-
 626 quality muon candidates forming a mu-jet. Similar to the background-enriched case, we then

627 continue adding tracks to form a pseudo-muon-jet, split it into fundamental dimuons and assign events either to category (a-2) or (a-3). The observed 2D invariant mass distribution of
 628 events in category (a-2) is shown in Fig. 14(a) and is compatible with the expectation based
 629 on the background template obtained earlier. Because the number of events is too small to
 630 evaluate the level of agreement visually, Fig. 14(b) shows the 1D invariant mass of all pseudo-
 631 dimuons in events of category (a-2) (the distribution contains two entries per event, one for
 632 each dimuon). The data are overlaid with the background prediction based on the 2D back-
 633 ground template obtained in the background-enriched sample by summing up 1D projections
 634 of the 2D template. Only the overall normalization of the background prediction is scaled to
 635 the data, as in the signal region. This comparison shows good agreement, thus validating the
 636 procedure.

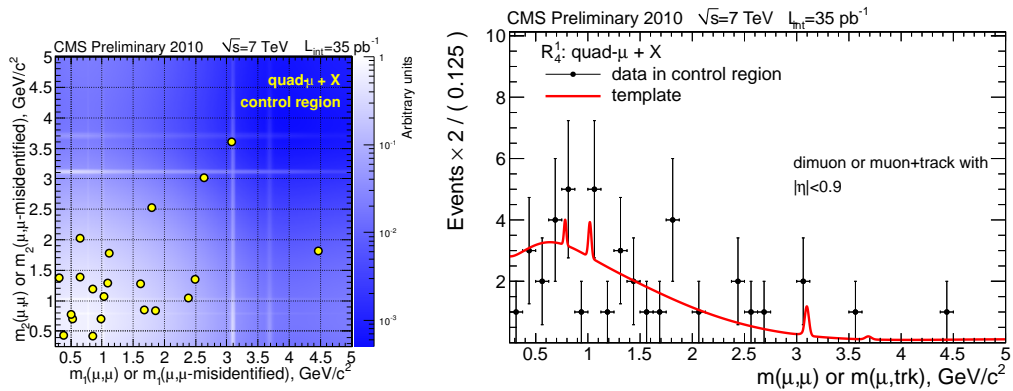


Figure 14: (a) 2D invariant mass distribution of the dimuons the $3\mu + \text{track}$ control region for category (a-2). (b) The invariant masses distribution of all dimuon candidates for the same events (two entries per event), compared to the prediction obtained from the 2D background template (the sum of the x - and y -projections of the 2D template).

638 As a second cross-check, we studied the sideband events in signal region (a-2) by looking at the
 639 off-diagonal part of the 2-D mass distribution. To hide a potential discovery before finalizing
 640 the procedure, the region along the diagonal was blinded by a strip 5σ wide in detector reso-
 641 lution. Only one event is observed in the off-diagonal region (see more details in Appendix H)
 642 consistent with the expectation of very low background based on a “back of the envelope” scal-
 643 ing $N_{4+0} = N_{3+1} \times N_{3+1} / N_{2+2} \sim 0.04 \pm 0.04$, which assumes that the probability to pick up
 644 each additional misidentified muon is roughly constant.

645 In a class of models with $h_{\text{dark}} \rightarrow a_{\text{dark}} a_{\text{dark}}$ where $m(h_{\text{dark}}) < 2m(a_{\text{dark}})$ and one or both of
 646 the a_{dark} particles are off-shell, the dimuon spectrum may not show characteristic mass peaks
 647 corresponding to $m(a_{\text{dark}})$. However, in these cases one would expect a peak in the four muon
 648 invariant mass distribution. Therefore, to improve the sensitivity of this analysis to such mod-
 649 els, we perform an additional fit of the four muon invariant mass distribution in region (a-2).
 650 The template is constructed using the same sample, two muon candidates and two tracks play-
 651 ing the role of misidentified muons, plotting the invariant mass of all four tracks. Figure 15(a)
 652 shows the invariant mass of such pseudo-mu-jets, which is used as a template for the back-
 653 ground shape. Note the two-humped structure in the distribution: the second hump is due to
 654 events with two muons from a J/ψ boosting the distribution for these events to higher mass. As
 655 a control region, we use the three-muon-plus-track sample with the same selections as before.
 656 The invariant mass distribution of the control region is shown in Fig. 15(b) overlaid with the
 657 background prediction using the background template fitted to the data with overall normal-
 658 ization being the only floating parameter. The comparison shows a good agreement, validating
 659 this technique.

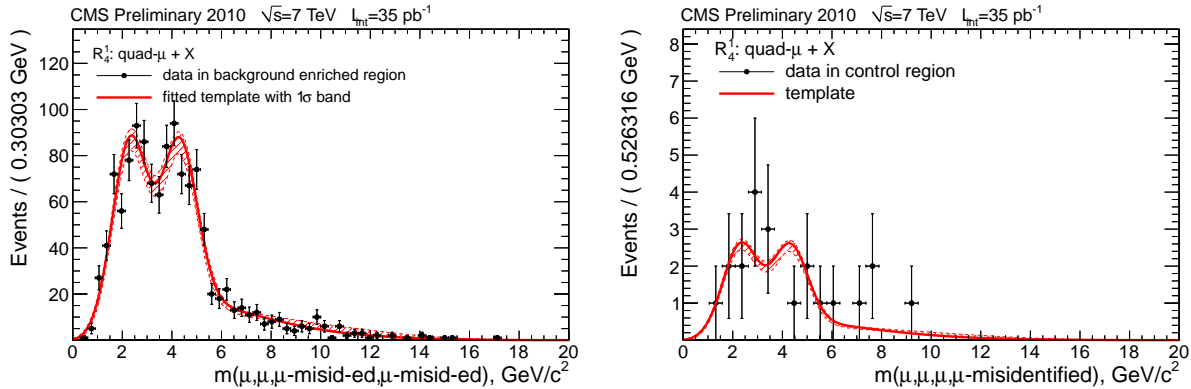


Figure 15: (a) Invariant mass distribution of the two pseudo-dimuon candidates in the two-muon-plus-two-tracks sample, which serves as a template for models with off-shell a_{dark} in category (a-2). (b) The same distribution for the three-muons-plus-track sample, with the background template normalization fitted to the data, showing good agreement.

660 4.4 Background Spectrum for Region (b-1)

661 The (b-1) signal region consists of events with two mu-jets each containing a single dimuon
 662 with both b -quarks decaying to $\mu\mu X$. The wide mass cut used to form mu-jets ensures that
 663 muons from nearby mu-jets do not fall in this category and a typical background event has
 664 a topology of two well-separated muon pairs. The fit for a possible signal in this region is
 665 performed in the 2D space of invariant masses of the two dimuons. Naïvely, because each
 666 b -quark decays independently of the other, the background distribution can be modeled by
 667 a Cartesian product of two identical 1D mass templates from a b -jet decay, derived from the
 668 $b\bar{b}$ -enriched sample selected in Sec. 4.1. However, because the dimuon invariant mass shape
 669 depends on the momentum of the b -quark due to momentum cuts, care must be taken to ensure
 670 that the kinematics of the background-enriched samples match the actual background events
 671 in the signal region. A related consideration is that one of the dimuons needs to contain a
 672 muon with $p_T > 15 \text{ GeV}/c$ within $|\eta| < 0.9$ to satisfy the trigger requirements, while the
 673 other dimuon does not. As a result, the shapes of the mass spectra for the two dimuons are
 674 not the same and must be measured separately for the “triggered” and “other” dimuons. One
 675 last consideration is a consequence of the way the signal 2D distribution is filled when both
 676 dimuons contain a muon satisfying trigger requirements: for these events we randomly assign
 677 the dimuons to the triggered and other sub-classes. This introduces a bias in the other dimuon
 678 spectrum that needs to be included in the modeling the background template.

680 To model the spectrum of the triggered dimuon, we use the $b\bar{b}$ -enriched sample selected in in
 681 Sec. 4.1 with the $b\bar{b}$ cuts defined in Eqn. (4) and require zero additional muons in the event.
 682 These events pass minimal acceptance requirements and therefore the dimuon always contains
 683 a trigger muon. The purity of the sample is high (Fig. 10) and we verified that these selections
 684 do not distort the $b\bar{b}$ dimuon mass shape (more details in the Appendix E). Figure 16 shows
 685 the invariant mass distribution of the triggered dimuons and the parameterized function fitted
 686 to the data, which will be used to construct the 2D template. The parameterized template uses
 687 the same universal functional form from Eqn. (5) with some of the parameters fixed.

688 To model the kinematics of the “other” dimuon, we use the $b\bar{b}$ -enriched sample to select events
 689 containing a dimuon (not required to contain a trigger-quality muon) and one additional muon:
 690 the additional muon is required to satisfy the trigger. Three-muon events with a small angle be-
 691 tween two of the muons are predominantly $b\bar{b}$ with one b -quark decaying to $\mu\mu X$ and the other

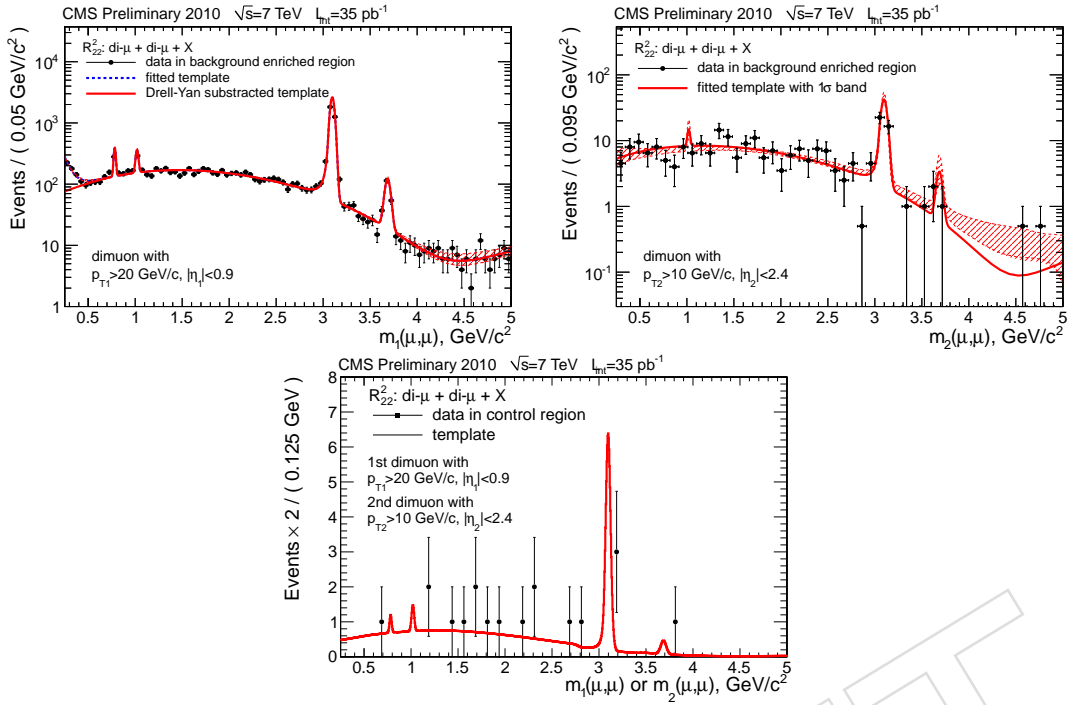


Figure 16: (a): dimuons with $b\bar{b}$ cuts (background-enriched region for triggered dimuon in (b-1)). (b): dimuons plus additional, triggered muon (background-enriched region for other dimuon in (b-1)). (c): The distribution of all dimuons in the off-diagonal part of the distribution in (b-1) compared to the prediction for the background shape obtained from the full 2D template and fitted to data for overall normalization only.

692 to μY . These selections ensure that the dimuon is unbiased by the trigger and also has approxi-
 693 mately the same kinematics as the events entering the signal region. Finally, we plot the invari-
 694 ant mass of selected dimuons with a weighting factor of $\frac{1}{2}$ to dimuons that contain a trigger-
 695 quality muon. This additional weighting is necessary to account for the bias in constructing the
 696 signal region 2D distribution for events with two trigger dimuons. (See Appendix F.2 for de-
 697 tails.) The resultant distribution for the other dimuon, along with the parameterized template
 698 to be used in the 2D mass template for the final fit, is shown in Fig. 16(b).

699 The final 2D background template is built from a Cartesian product of two parameterized 1D
 700 shapes for the triggered and other dimuons. As a cross-check, we compared the constructed
 701 background templates for both the triggered and other dimuons in signal region (b-1) with the
 702 background predictions using simulation. A large sample of $b\bar{b} \rightarrow 2\mu 2\mu X$ Monte Carlo, sim-
 703 ulated by Pythia 6 and decayed by EvtGen, was used to select events passing all region (b-1)
 704 selections. We verified that the 2D distribution has no correlations between the masses of the
 705 two dimuons, confirming the assumption used in constructing the background template that
 706 the 2D distribution is factorizable. In addition, the final background distributions for the trig-
 707 gered and other dimuons were compared with the data-driven templates, showing reasonably
 708 good agreement (see Appendix F.3).

709 To validate the technique, we use events satisfying selections for the (b-1) signal region, but
 710 in the off-diagonal part of the dimuon-dimuon mass plane (a 5- σ strip along the diagonal was
 711 blinded). Ten events were observed in that region, consistent with back-of-the-envelope scal-
 712 ing of the $b\bar{b} \rightarrow 2\mu X$ sample: $N_{4\mu+X} \sim \frac{1}{2} N_{2\mu+X} \mathcal{B}(b \rightarrow 2\mu X) = \frac{1}{2} \times 12841 \times 0.002 = 12.8$
 713 events. The distribution of these events is consistent with the background template, as shown
 714 in Fig. 16(c).

715 5 Statistical Interpretation of the Results

716 Statistical interpretation of the results was performed for each of the topologies separately with
 717 a binned likelihood fit of the data to the sum of parameterized functional forms for signal and
 718 background templates:

$$\mathcal{L} = \prod_{i=1}^{N_{bins}} \frac{\nu_i^{n_i} e^{\nu_i}}{n_i!}, \quad (6)$$

719 where i runs over all bins in the signal dominated region of space of invariant masses of the
 720 dimuon candidates in the event, \vec{m} , n_i is the number of observed events in the data (or pseudo-
 721 data in analyzing expected sensitivity when possible), and ν_i is the expected rate of events (for
 722 signal plus background) in bin i derived from the rate function $\nu(\vec{m})$ which has the following
 723 functional form:

$$\nu(\vec{m}) = \sigma B L \alpha_{rec} \times \frac{S_{m_0}(\vec{m}, \vec{p}_S)}{\int_{sig} S_{m_0}(\vec{m}, \vec{p}_S) d\vec{m}} + N_{BG} \times \frac{BG(\vec{m}, \vec{p}_{BG})}{\int_{sig} BG(\vec{m}, \vec{p}_{BG}) d\vec{m}} \quad (7)$$

724 where \vec{m} is a vector in the space of invariant masses of the dimuon candidates, \vec{p}_S and \vec{p}_{BG} are
 725 parameters used in the signal and background shape templates, $S_{m_0}(\vec{m}, \vec{p}_S)$ is the signal shape
 726 template for a new boson with true mass m_0 , $BG(\vec{m}, \vec{p}_{BG})$ is the predicted background shape,
 727 σ is the cross-section for the new boson production, B is the branching fraction for the dimuon
 728 decay, L is luminosity, α is the acceptance, and N_{BG} is the background rate normalization.
 729 Integration is performed over the signal dominated region (near the diagonal) in each category,
 730 except the case of 1D distributions where the entire range is considered the signal region. The
 731 expected rate of events in any given bin i is an integral of $\nu(\vec{m})$ ⁵ over the phase space of the
 732 bin:

$$\nu_i = \int_{bin i} \nu(\vec{m}) d\vec{m} \quad (8)$$

733 Additionally, we substitute the experimental acceptance α_{rec} with:

$$\alpha_{rec} = \alpha_{gen} \epsilon_\alpha \quad (9)$$

734 to absorb all experimental inefficiencies and (for model dependent results only) effects of mi-
 735 gration of events between the categories due to reconstruction and trigger inefficiencies into a
 736 new parameter ϵ_α .

737 The imprecise knowledge about the parameters entering the equation, the posterior PDF for
 738 $\sigma B \alpha_{gen}$ is obtained by integrating over all other parameters that are considered nuisance and
 739 using appropriate priors:

$$\begin{aligned} \mathcal{L}'(\sigma B \alpha_{gen}, m_0) = & \int \mathcal{L} \times \text{PDF}(\vec{p}_S) \text{PDF}(\vec{p}_{BG}) \text{PDF}(L) \text{PDF}(N_{BG}) \text{PDF}(\epsilon_\alpha) \times \\ & d\vec{p}_S d\vec{p}_{BG} dL dN_{BG} d\epsilon_\alpha. \end{aligned} \quad (10)$$

740 Prior distributions are normalized and are obtained, for \vec{p}_S and \vec{p}_{BG} , from the fits that construct
 741 templates from background-enriched regions (including correlations), for ϵ_α and L from log-
 742 normal priors, and σB from flat priors. Note that $\text{PDF}(\vec{p}_{BG})$ is a full multi-dimensional prob-
 743 ability density function for the parameters obtained from the fits to the data in background-
 744 enriched samples when constructing templates. Care was taken to ensure that those PDFs are

⁵Note that $\nu(\vec{m})$ also depends on many parameters including the new physics signal cross section, generally unknown background normalization etc

745 always positively defined. For the case of 1D distributions (region (a-1)), N_{BG} was taken to have
 746 a flat prior, while for the multi-dimensional regions, the PDF(N_{BG}) was obtained as a posterior
 747 of the likelihood fit in the sidebands (the off-diagonal regions) for N_{BG} where initial PDF(N_{BG})
 748 was taken to have a flat prior:

$$\text{PDF}(N_{BG}) = \int_{off-diag} \mathcal{L}|_{\sigma=0} \times \text{PDF}(\vec{p}_{BG}) d\vec{p}_{BG}.$$

749 Various efficiency uncertainties are convoluted into the acceptance uncertainty. In the case of
 750 no observed signal, a limit is set for each value of m_0 in the allowed range and the 95% C.L.
 751 upper limit on $\sigma B \alpha$ is derived from:

$$0.95 = \int_0^{\sigma_{95\%}(m_0)} \mathcal{L}'(\sigma B \alpha, m_0) d(\sigma B \alpha). \quad (11)$$

752 The integral calculation is performed using the modified Bayesian Monte Carlo algorithm
 753 available in the RooFit package (modifications were mainly aimed to optimize the convergence
 754 speed).

755 The expected limits are evaluated by normalizing the background template to the expected
 756 number of background events, generating pseudoexperiments, and determining the average
 757 limit as well as 68% C.L. and 95% C.L. ranges for the expected limit.

758 In the case of discovery, we also need to evaluate the probability of observing a fluctuation as
 759 significant as the one observed in the data. We adopt the following algorithm. We construct
 760 the following quantity:

$$\mathcal{R}\mathcal{L} = \mathcal{L}(S + B) / \mathcal{L}(B) = \frac{\max(\sigma B, m_0) \mathcal{L}'(\sigma B, m_0)}{\mathcal{L}'(\sigma B = 0, m_0)}, \quad (12)$$

761 which is defined for either the data distribution being analyzed or for the pseudodata. \mathcal{L}' is
 762 defined in Eq.(10). For data, this ratio is calculated by taking the ratio of the likelihood at the
 763 position of the maximum as obtained in the fit. For pseudoexperiments, the maximum fluctuation
 764 is searched by scanning the distribution in small steps in m_0 to find the point where
 765 the likelihood ratio reaches the maximum (in each step in m_0 , σB in the numerator is the one
 766 that maximizes the likelihood \mathcal{L}'). Pseudoexperiments are generated following the null hypothesis
 767 (no signal) with the number of generated events following Poisson distribution using the
 768 normalization for the backgrounds as obtained from the fit (in the sideband regions for multi-
 769 dimensional space), removing integration over N_{BG} in Eq.(10) and treating N_{BG} as a measured
 770 parameter. To evaluate the p -value of observing a fluctuation more significant than the one
 771 observed in data, we count the fraction of pseudoexperiments in which $\mathcal{R}\mathcal{L} > \mathcal{R}\mathcal{L}(\text{Data})$.

772 6 Results

773 Unblinding the signal regions did not reveal any evidence for high muon-multiplicity events in
 774 the 2010 CMS dataset. Exact numbers of events in each topology are given in Table 3. The only
 775 region with a large number of events is (a-1), the high-momentum dimuon region (which was
 776 expected from Fig. 11(a)). An incisive test of this signal region is given in the fit results, below.
 777 The (a-2) topology includes one event (see event display in Appendix H), but the two dimuons
 778 in this event are not consistent with a single mass. Similarly, the (b-1) region includes 9 events
 779 (see sample event display in Appendix H), but none of these are consistent with a single m_1
 780 mass.

Table 3: Number of observed events in each signal category. For regions with $N \geq 2$ dimuons, the number of events is shown both for the entire category as well as for the $5\sigma(m)$ signal region near the N -dimensional diagonal ($\sigma(m, p_T) = (0.026 + 0.0065 m \text{ GeV}/c^2$ for (a-2) and $\sigma(m, p_T) = (0.026 + 0.013 m \text{ GeV}/c^2$ for (b-1)).

Signal region	Description	Number of events	on diagonal
(a-1)	$N_{\mu-jet} = 1, N_\mu = 2, p_T > 80 \text{ GeV}/c$	145	—
	$2m_\mu < m < 0.25 \text{ GeV}/c^2$	4	—
	$0.25 < m < 5 \text{ GeV}/c^2$	130	—
	$5 < m < 9 \text{ GeV}/c^2$	11	—
(a-2)	$N_{\mu-jet} = 1, N_\mu = 4$ (opp. sign pairs)	1	0
(a-3)	$N_{\mu-jet} = 1, N_\mu > 4$	0	0
(b-1)	$N_{\mu-jet} = 2, N_\mu = 2$ in each	9	0
(b-2)	$N_{\mu-jet} = 2, N_\mu > 2$ in at least one	0	0
(c-1)	$N_{\mu-jet} \geq 3$	0	0

781 No high muon-multiplicity events were observed in any of other signal topologies. Figure 17
 782 shows the distributions for regions (b-1), (a-1), and (a-2) with the background-only fit overlaid
 783 with the data. We also show the invariant mass of the four muons for the single event in the
 784 (a-2) category found in the off-diagonal part of the region sets the upper limit on the possible
 785 production of $h_D \rightarrow \gamma_D \gamma_D$ in the special scenario where $m(h_D) < 2m(\gamma_D)$ leading to the off-
 786 shell production of γ_D .

787 6.1 Model Independent Results

788 Given no observed excess of data consistent with the properties of the signal of new physics,
 789 we set 95% C.L. upper limits on the production rate of the new physics events. To simplify
 790 future interpretation of our results, we choose to present these limits as $\sigma(pp \rightarrow X) \times B(X \rightarrow$
 791 $Na_{\text{dark}} + Mh_{\text{dark}}) \times \alpha_{\text{gen}}$, where α_{gen} is the ideal detector (generator level but with geometric
 792 and kinematic selections on muon p_T and η) acceptance for the events of the topology in ques-
 793 tion. Because no events were observed in any of the high dimuon-multiplicity regions (a-3),
 794 (b-2), and (c-1), we combine them into a single region. To be conservative, in cases when exper-
 795 imental acceptances for lower multiplicity dimuon regions in complex cascade models get an
 796 additional enhancement due to higher-multiplicity signatures with some of the dimuons not
 797 reconstructed in the fiducial volume, the experimental acceptance is taken to be generator level
 798 acceptance multiplied by corresponding efficiencies of reconstruction and triggering (and so
 799 can never be greater than generator level acceptance). In some models with large number of
 800 final state dimuons, these enhancements can be fairly substantial, so this approach can be very
 801 conservative for such models. However, for the results to remain being applicable to a wide
 802 range of models, this seems like the only reasonable solution. In this case ϵ_α in Eq. (10) is the
 803 experimental efficiency of reconstructing a particular topology in the data given that the event
 804 was reconstructed in that same topology at the generator level. For systematics, the parameters
 805 used in the fit are listed in Table 4 along with the description of the priors used in the fit.

806 6.2 Limits on Benchmark Models

807 For model dependent results, we use reconstruction level acceptances calculated using the sim-
 808 ulation for each of the signal regions. The likelihood function is calculated for each of the re-
 809 gions and the sensitivity of the various channels was combined at the level of likelihoods prior
 810 to integrating over the nuisance parameters to ensure that the correlated systematics effects
 811 are correctly accounted for. In addition to the systematic uncertainties listed for the model-

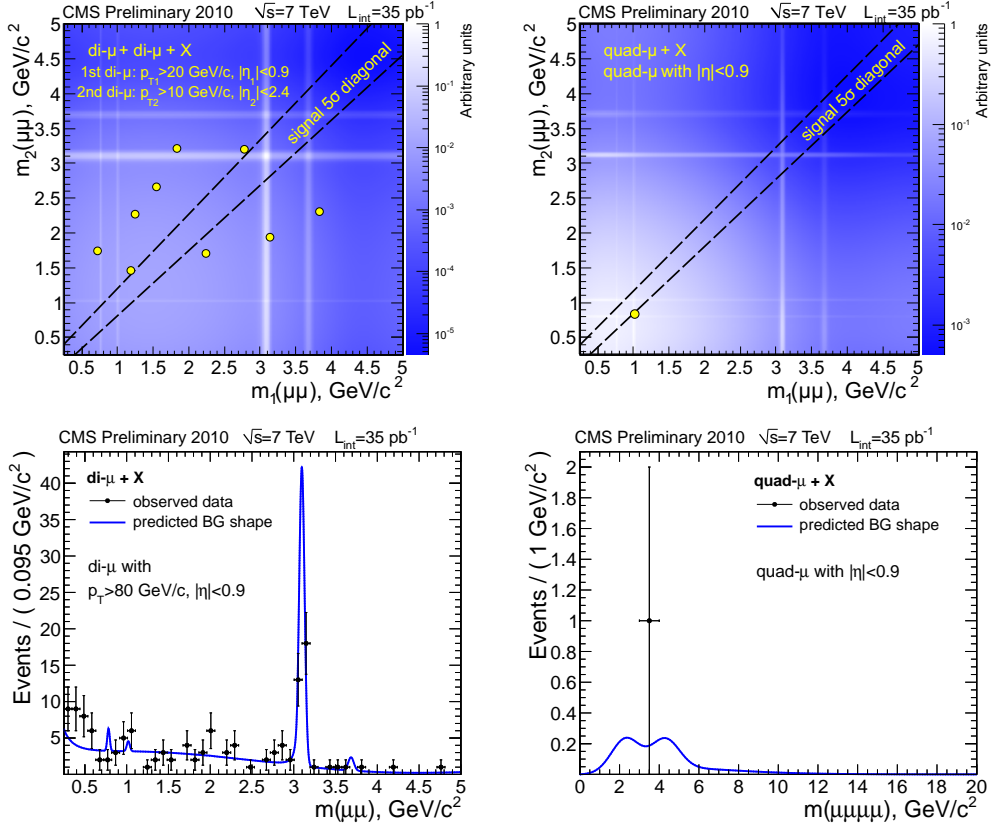


Figure 17: 2D and 1D distributions of events in data and expected backgrounds in signal categories: (a): “double dimuon” region (b-1), (b): the “quadmuon” region category (a-2), (c): “single dimuon” region (a-1), (d): (b): the invariant mass of the four muons for the single event in the “quadmuon+X” category found in the off-diagonal part of the region sets the upper limit on the possible production of $h_D \rightarrow \gamma_D \gamma_D$ in the special scenario where $m(h_D) < 2m(\gamma_D)$ leading to the off-shell production of γ_D . None of the events in the signal categories have invariant masses of the dimuons consistent with one another, which would indicate presence of signal. The dashed lines indicate signal regions for 2D categories (those are five standard deviations from the diagonal in detector resolution). No events were observed in any of the high dimuon-multiplicity regions (a-3), (b-2), or (c-1).

812 independent case, the model-dependent limits take into account the 3% uncertainty in the ac-
 813 ceptance due to PDF uncertainties (obtained using CTEQ6.6 and comparing the default pa-
 814 rameterization CTEQ6L with the NNPDF2.0 and MSTW-2008). Additionally, the higher muon
 815 multiplicity category is taken into account in the acceptance estimation. Because in this case
 816 the muon momentum spectrum is known in each case and the limits are set for specific mass
 817 points, the variation of efficiencies to account for the unknown mass and p_T spectrum is not
 818 used.

819 As one example, we calculate the limit on the production cross section times branching ratio for
 820 dark SUSY models with dark fermion production. Acceptances for the two model variations,
 821 $B(\tilde{q} \rightarrow q(n_2 \rightarrow n_1 \gamma_D)) = 100\%$ and $\tilde{q} \rightarrow q n_2 (\rightarrow n_1 h_D (\rightarrow 2\gamma_D)) = 100\%$, with squark-squark
 822 and squark-gluino production the acceptance is shown in Tables 8 and 9 for three choices
 823 of $B(\gamma_D \rightarrow \mu\mu) = 100, 50, \text{ and } 33\%$. Depending on the branching fractions and the model, the
 824 limit is dominated by different signal regions with the results shown in Figs. 19(a) and (b). Note
 825 the weak dependence of the limit on squark mass, emphasizing the weak model-dependence

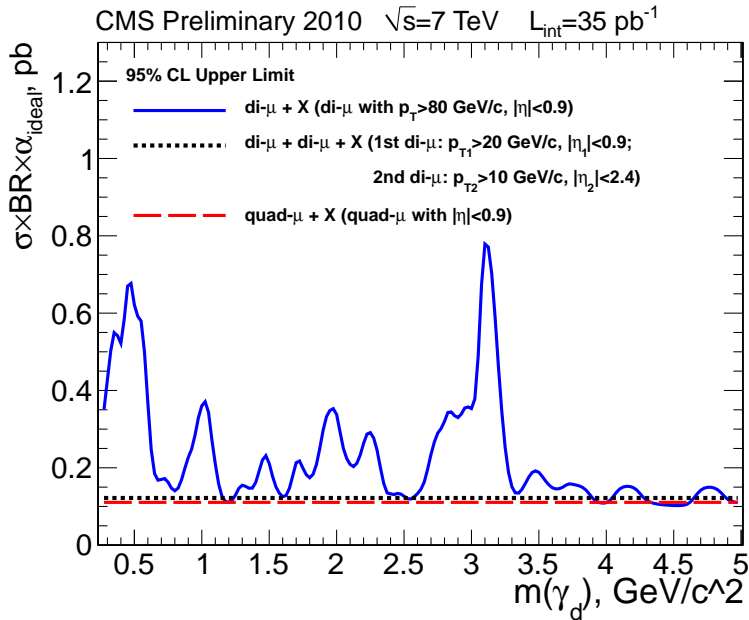


Figure 18: 95% C.L. limits on production cross-section for three topologies: “single dimuon” (a-1), “two dimuons” (b-1) and “quadmuon+X” (all others). In the absence of signal events for the two latter topologies, the limits for regions correspond to three signal events corrected for the experimental efficiency of reconstructing this particular topology in the data given that the event was reconstructed in that topology at the generator level.

of the results of this analysis. It is important as the branching fractions for squark decays to the dark sector fermions are not 100%, e.g. due to a weaker coupling of the dark and visible sectors.

In the case of extra $\mathcal{U}(1)_{\text{dark}}$ model, Table 7 shows acceptances for each of the relevant regions for three choices of $B(\gamma_D \rightarrow \mu\mu) = 100, 50, \text{ and } 33\%$. Fig. 19(c) shows the corresponding limit.

In the case of NMSSM, the sensitivity is dominated by the (b-1) category with the acceptance is of the order of 25% (see Table 6), which leads to a limit on the lightest CP-even NMSSM Higgs production rate $\sigma(pp \rightarrow h)B(h \rightarrow aa)B^2(a \rightarrow \mu\mu) \sim 0.4 \text{ pb}$. Taking $B(a \rightarrow \mu\mu) \sim 20\%$ for $m(a)$ below $2m_\tau$, this leads to an upper limit $\sigma(pp \rightarrow h)B(h \rightarrow aa) \sim 10 \text{ pb}$. To set the limits and make a comparison with the Tevatron sensitivity, we follow the method used in [23] and plot the density of model points consistent with LEP and the WMAP measurements in the plane of $B(h_1 \rightarrow a_1 a_1 \rightarrow 4\mu)$ versus $\sigma(pp \rightarrow h_1)$ for $\sqrt{s} = 7 \text{ TeV}$. The experimental limits on such models from Tevatron and LHC exclude the upper right corner of this parameter space. Because exact limit for a particular model point depends on the acceptance for this specific point (via dependence on m_h and m_a), experimental limits do not appear as strict lines in this plot. We therefore added the bands to show the range of limits that correspond to the range of acceptances for allowed models. Figure 20 shows that with $L \sim 75\text{--}100 \text{ pb}^{-1}$, the LHC sensitivity will surpass that of the Tevatron experiments and will significantly restrict the allowed parameter space with $L = 1 \text{ fb}^{-1}$.

7 Conclusions

In a model-independent search for groups of collimated muons from $m_1 \rightarrow \mu\mu$, we found zero events consistent with two or more m_1 decays in the same event, and no excess over

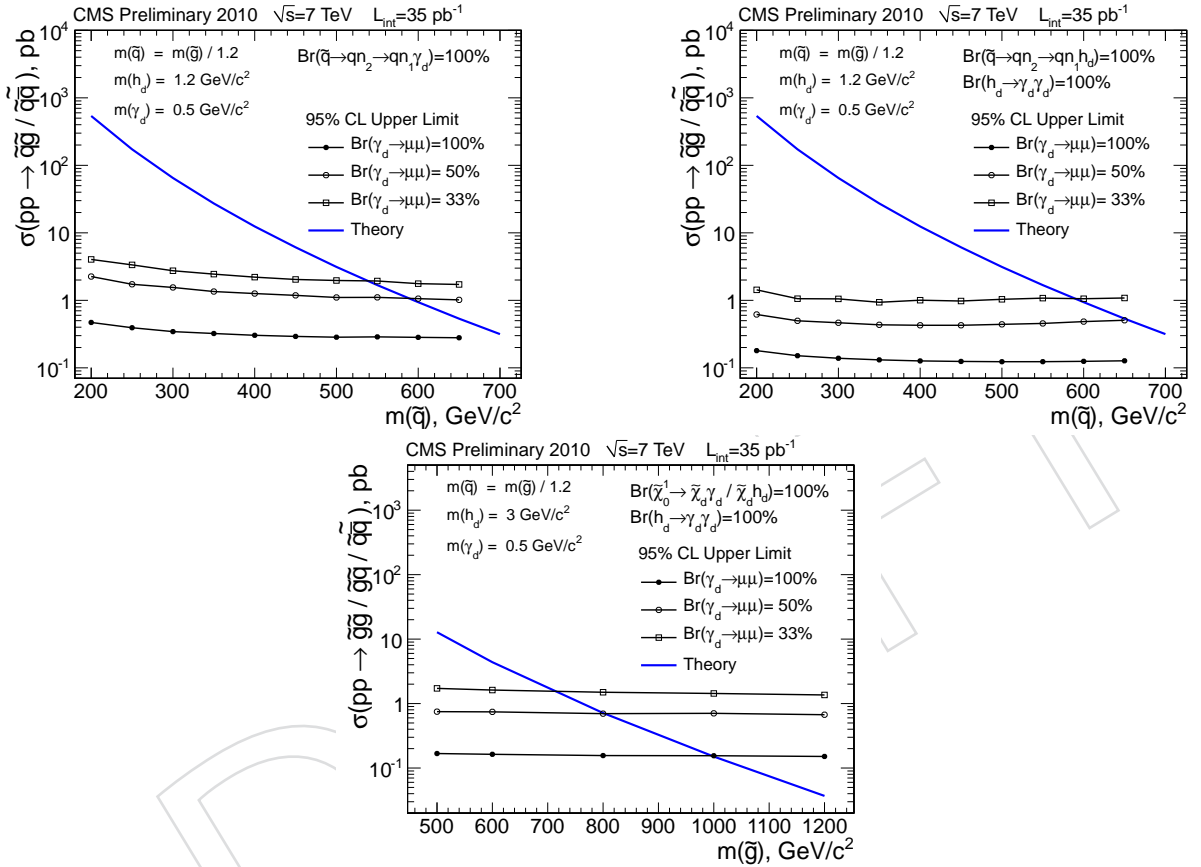


Figure 19: Limits on the Dark Fermion Cascades model and the Extra $U(1)_{dark}$ models described in Sections 2.2 and, 2.1 derived from the limits for each of the signal regions weighted with the model acceptance for each region. The $\gamma_{dark} \rightarrow \mu\mu$ branching fraction has a profound effect on the model acceptance and hence the final result. Note that the non-universality of squark masses can lead to decrease in the production cross sections.

Table 4: List of systematic uncertainties used for setting model-independent limits. (*) α and n in Crystal Ball are strongly correlated, the correlation coefficient used was -0.9 based on MC studies of J/ψ and ψ' , and cross-checked with data. Acceptance uncertainties are for $\alpha_{rec}/\alpha_{ideal}$ and includes the systematic uncertainties in the knowledge of efficiencies as well as a separate uncertainty to account for variations in the tracking efficiency itself with $p_T^{\mu-jet}$ and $m(\mu\mu)$. For the latter we assume that the bulk of the $p_T^{\mu-jet}$ distribution is below 400 GeV/c and the mean $p_T^{\mu-jet} \leq 250$ GeV/c. For higher momentum lepton jets, the uncertainties will need to be increased to account for the decrease in tracking efficiency.

Systematic	Region			Prior
	(a-1)	(a-2)	(b-1)	
hline Luminosity	4%	4%	4%	Log-normal
Acceptance parameters:				
$\alpha_{reco}/\alpha_{ideal}$	$94.7 \pm 0.1\%$	$79.3 \pm 0.3\%$	$89.8 \pm 0.2\%$	–
α_{EB}/α_{BB}	–	–	0.55 ± 0.05	Log-normal
Acceptance uncertainties:				
Muon eff. incl. trigger	1%	2.3%	4%	Log-normal
Tracking eff. uncertainty vs $m(\mu\mu)$	2-5%	2%	4-10%	Log-normal
Tracking eff. variation vs $p_T^{\mu-jet}$	20%	7%	35%	Log-normal
Signal Shape (Crystal Ball parameters):				
σ_0^B	0.00675 ± 0.00325			Log-normal
σ_0^E	0.0075 ± 0.0040			Log-normal
slope $_\sigma^B$	0.0070			–
slope $_\sigma^E$	0.0140			–
α	1.8 ± 0.16			bi-variate gaussian*
n	2.0 ± 0.6			bi-variate gaussian*
Background Shapes:				
\vec{p}_{BG}				Actual multi-dim posteriors from the fits

backgrounds for single, high- $p_T m_1$ decays. Relaxing the assumption that m_1 must be on-shell in $m_2 \rightarrow m_1 m_1 \rightarrow 4\mu$ cascades and searching for any collimated group of four or more muons, we found one event, but this event is fully consistent with expected backgrounds from fake muons. All CMS Run 2010A and 2010B events with four or more muons and two high- p_T muons with $m_{inv} < 5$ GeV/c 2 are presented with background PDFs in Fig. 17.

With these observations, three limits on any new physics producing low-mass multi-muons are presented in Fig. 18. New physics producing four or more muons is excluded above a $\sigma \times \mathcal{B} \times \alpha_{gen}$ of 0.1 pb at 95% confidence level, corresponding to a limit of three events, as no background was observed. The limit for high- p_T low-mass dimuons is more complex, as it was extracted from a channel with Standard Model backgrounds.

To illustrate the use of these model-independent results, we applied it to three benchmark models with acceptances presented in Table 2 and Appendix G. These limits are shown in Figs. 19 and 20.

Table 5: List of systematic uncertainties used for setting model-dependent limits. Signal shape parameters are the same as in the model-independent case. Uncertainties assume mean $p_T^{\mu-jet} < 200 \text{ GeV}/c^2$, which is true for all models used.

Systematic	Region				Prior
	(a-1)	(a-2)	(b-1)	others	
hline Luminosity	4%	4%	4%	4%	Log-normal
PDF (accept.)	3%	3%	3%	3%	Log-normal
Muon eff. incl. trigger	1%	2.3%	4%	4%	Log-normal
Tracking eff. uncertainties					
$m(\mu\mu) = 0.25 \text{ GeV}/c^2$	2%	2%	4%	4%	Log-normal
$m(\mu\mu) = 0.50 \text{ GeV}/c^2$	5%	2%	10%	10%	Log-normal
$m(\mu\mu) \geq 1.0 \text{ GeV}/c^2$	2%	2%	4%	4%	Log-normal

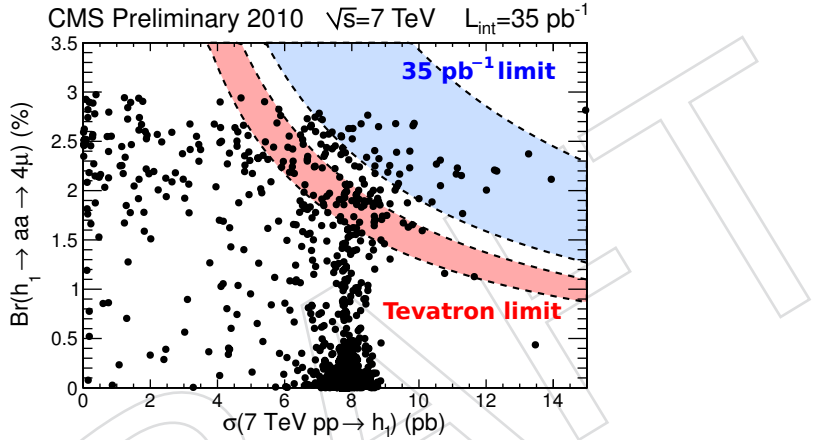


Figure 20: Limits on the allowed NMSSM models consistent with LEP exclusions and the relic density measurements in the plane of $B(h_1 \rightarrow a_1 a_1 \rightarrow 4\mu)$ versus $\sigma(pp \rightarrow h_1)$ for $\sqrt{s} = 7 \text{ TeV}$. The allowed models are shown as points and the experimental limits from Tevatron and LHC exclude the upper right corner of the parameter space. Because exact limits depend on the acceptance for each model point and therefore do not appear as strict lines, the bands show the range of limits that correspond to the range of acceptances for allowed models. The plot shows that with $L = 1 \text{ fb}^{-1}$ the LHC sensitivity will surpass that of the Tevatron experiments.

861 A Motivation for reconstruction methods

862 Figure 21 shows a comparison of performances of the outside-in and the inside-out (the one
 863 used in this analysis) muon identification algorithms in Monte Carlo. The plots show the prob-
 864 ability of finding both muons in a simulation sample of the dimuon events with a flat invariant
 865 mass distribution. Efficiencies are shown as a function of the separation of their trajectories in
 866 the muon system.

867 To quantify the separation of muon trajectories, we construct a cylinder with 600 cm radius,
 868 centered on the beamline, and two planes transverse to the beamline and 700 cm from the
 869 interaction point. The muon trajectories are propagated to the cylinder if $|\eta| < 1$ (barrel) and
 870 are propagated to one of the planes if $|\eta| > 1$ (endcaps). The difference in azimuthal coordinate
 871 of the two muon trajectories on these surfaces are called $\Delta\phi$. Closeness in the other coordinate

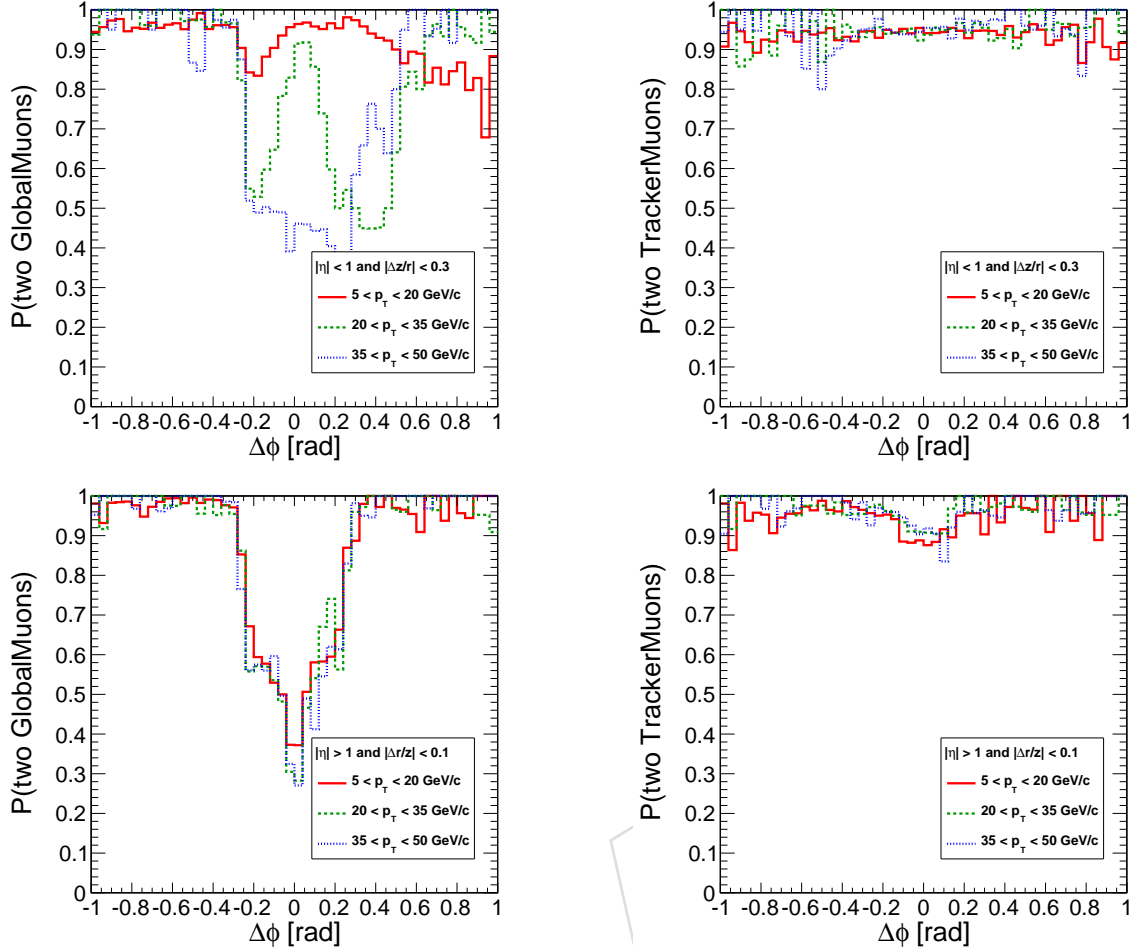


Figure 21: Comparison of outside-in (left) and inside-out (right) muon identification efficiency as a function of the separation of the muon trajectories in the muon system (top: barrel, bottom: endcap).

is quantified by $\Delta z/r$ on the cylinder and $\Delta r/z$ on the planes. Figure 21 shows efficiency as a function of $\Delta\phi$ with a cut on $\Delta z/r$ and $\Delta r/z$ for the barrel and endcaps, respectively.

The deficiencies of the outside-in reconstruction are due to confusion of “stand-alone” segments only track-finding in the muon system when multiple muons are present. One of the two muons is almost always found (important for trigger efficiency), but not both (important for offline reconstruction). In the barrel, the shape of the inefficient region in $\Delta\phi$ is complicated by muon energy loss: the propagation of trajectory into the muon system was done on the basis of generator-level parameters at the interaction point. As the p_T of the muons increases, the shape of the inefficient region consolidates and symmetrizes around $\Delta\phi = 0$.

The inside-out reconstruction algorithm used by this analysis is much less sensitive to overlapping muons. Only a small dip can be seen in the endcap, analyzed in more detail in Fig. 5 in the main text.

B Muon Trigger Performance for Events with Nearby Muons

There are many reasons why the muon trigger performance may be affected by the presence of additional muon hits or segments nearby affecting triggering efficiency for events with multi-

ple nearby or even crossing (in the muon stations) muons. In the worst-case scenario, events with a sufficiently energetic muon and additional nearby muons, there could be no single muon reconstructed by the trigger or, because of incorrect assignment of segments, the trigger may reconstruct one or more soft muons below the trigger threshold. While outside-in reconstruction used in the HLT always reconstructs the highest p_T muon, it often fails in reconstructing the second muon if it happens to be nearby. Therefore, selecting such events using multi-muon triggers (e.g. HLT_DoubleMu3) will lead to a substantial loss of efficiency even at the HLT level. This was one of the reasons for this analysis opting for a single-muon trigger, as outside-in reconstruction guarantees that at least the highest p_T muon candidate is reconstructed. However, apart from HLT, there are many reasons why the topologies for intersecting muons may be difficult for the Level-1 muon trigger. Examples of it include the limitation in the CSC on the maximum number of two trigger stubs per chamber reported to the CSC Track Finder (CSC-TF), which could lead to stubs reported to the CSC-TF being a mixture of stubs from different muons. Another example is ghost-busting veto at the level of chambers and in the CSC-TF vetoing duplicate muon candidates. While the latter effect is likely to mostly affect multi-muon triggers by failing to reconstruct two nearby muons, the former may affect even the single muon triggers by not reconstructing any muon candidates above the trigger threshold.

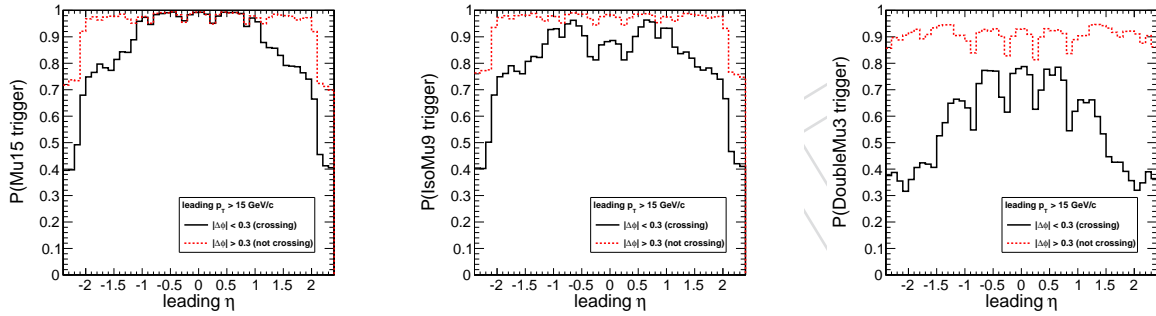


Figure 22: Efficiency of three triggers as a function of η and degree of trajectory-crossing in the muon system. Left: single-muon, unisolated trigger (used within $|\eta| < 0.9$). Middle: single-muon, isolated trigger (not used). Right: double-muon trigger (not used).

To investigate these effects, we used the same sample of simulated dimuon with a flat dimuon invariant mass distribution and measured trigger efficiency for single inclusive muon (HLT_Mu15.v1), single isolated muon (HLT_IsoMu9), and the dimuon (HLT_DoubleMu3) trigger configurations. Because the main cause of inefficiency is the closeness of muons in muon stations, we split the sample into the “crossing” and “not crossing” samples using $\Delta\phi$ of the two propagated muon positions at the cylinder and planes described in Appendix A. We use trigger emulation to parameterize efficiency of each trigger using η of the highest p_T muon. The corresponding efficiencies are shown in Fig. 22 for the three trigger configurations. From the comparisons of the “crossing” and “not crossing”, it is evident that only the inclusive non-isolated trigger is robust with respect to the presence of additional muon segments, and only in the barrel region, which determined the requirement of a trigger muon within $|\eta| < 0.9$ in our analysis. The same trigger develops inefficiency in the overlap and endcap region, likely because of the confusion in selecting segments used in building a track and the effects of the “ghost-busting” procedure in the CSC-TF. The isolated trigger shown in Fig. 22(b), is also developing inefficiency for “crossing” topology in the entire range due to the second muon interfering with the isolation requirements. Finally, as shown in Fig. 22(c), the dimuon configuration suffers the largest inefficiency for the “crossing” topology as in this case the requirement is that both outside-in muon candidates are to be found. The reduction in efficiency for the “not crossing” topology is because the efficiency in this case is a product of trigger efficiencies for both legs and the

inefficiency in reconstructing the second muon reduces the overall “plateau” efficiency. These observations show that the the CSC muon trigger algorithm performance deteriorates significantly⁶ in the presence of nearby muons even when the requirement is to reconstruct at least one (high- p_T) muon. Both DT and CSC dimuon trigger efficiencies show large degradation if the two muons are close to one another and the requirement is to reconstruct both muon candidates.

While the above addresses the algorithmic part of the muon trigger performance in the presence of additional nearby muons, another source of trigger inefficiency is due to generic instrumental effects. These include accuracy in simulating the response of the chambers in the fiducial volume and on edges in terms of stub reconstruction efficiency, reduction in efficiency due to dead regions, masked channels etc. These effects are not correlated with the presence of additional nearby muons and are universal. Therefore, we correct for the difference between simulation predictions and actual efficiency in the data using a single scale factor for inclusive muon trigger efficiency based on the measurement derived in Appendix C, below.

Based on these observations, we conclude that since the masses and momentum distributions of new physics dimuons is unknown, the endcap trigger efficiency cannot be quantified easily without parameterizing efficiency in both of these variables, which will substantially complicate the analysis and later interpretation of the results. That is why we require at least one above-threshold muon in the barrel per event.

C Trigger Efficiency Correction from Tag-and-Probe

To account for differences between the simulated trigger efficiencies and the real trigger efficiency, we performed a tag-and-probe study of our datasets with the $Z \rightarrow \mu\mu$ resonance and consulted similar studies from other CMS analyses.⁷ We selected two offline muons passing our selection criteria (Sec. 3.2), as well as $p_T > 15 \text{ GeV}/c$. We designated one muon as a tag and required it to be in the endcap with $1.2 < |\eta| < 2.1$ and matched to a $p_T > 15 \text{ GeV}/c$ trigger object (Level-3), thereby satisfying the trigger. The other muon, designated as probe, was required to have $|\eta| < 0.9$. We call this sample of events the denominator. If, in addition to these requirements, the probe also matched a Level-3 $p_T > 15 \text{ GeV}/c$ trigger object, the event belongs to a numerator sample. The denominator and numerator samples were independently background-subtracted using the sidebands shown in Fig. 23 and a linear background shape. The number of events in the background-subtracted numerator divided by the number of events in the background-subtracted denominator is taken to be the efficiency of the single-muon trigger with $p_T > 15 \text{ GeV}/c$, $|\eta| < 0.9$ (a combination of HLT_Mu9 and HLT_Mu15 with kinematic cuts on the Level-3 muon to emulate $15 \text{ GeV}/c$ for the whole dataset). Results are shown in Fig. 23. This study was performed for the dataset used in this analysis and a Monte Carlo sample generated in the same software version as the Monte Carlo samples used to calculate efficiencies for this analysis. The data-over-MC ratio, $0.947/0.978$ implies a 0.968 ± 0.006 scale factor, in agreement with studies performed by other CMS groups.

The tag and probe are required to be in non-overlapping regions of the detector (endcap and barrel, respectively) to ensure that their trajectories do not cross in the muon system. We know

⁶This study was performed with a 2010B-like endcap trigger simulation— no ME1/1 singles and modified ghost suppression— though the conclusion is the same for the 2010A-like endcap trigger simulation.

⁷Summary of muon trigger efficiency in $t\bar{t}$ cross-section studies: <https://twiki.cern.ch/twiki/bin/view/CMS/TopLeptonPlusJetsEffStudies> and especially Sinéad Walsh’s talk at the Muon HLT POG: <http://indico.cern.ch/conferenceDisplay.py?confId=122082>. These studies find an HLT_Mu9 scale factor of $0.94/0.97 = 0.969 \pm 0.002$ and an HLT_Mu15 scale factor of $0.955/0.97 = 0.985 \pm 0.002$ in the $|\eta| < 0.9$ barrel region.

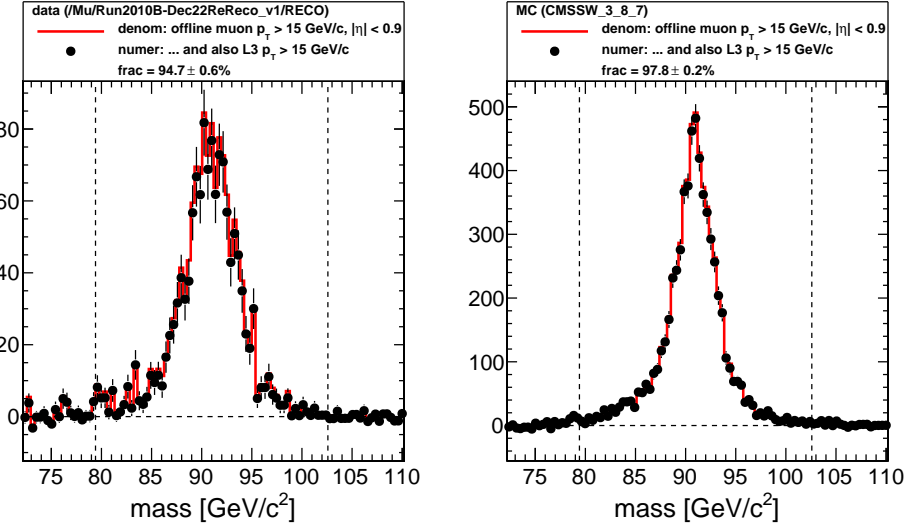


Figure 23: $Z \rightarrow \mu\mu$ events with and without a $p_T > 15 \text{ GeV}/c$ trigger object matched to the probe muon. Sidebands beyond the dashed lines were used to subtract non-resonant backgrounds. Left: dataset used for the analysis. Right: Monte Carlo generated in the same software release as all efficiency measurements. See text for details.

from studies in Appendix A that the outside-in muon identification algorithm is highly inefficient for muons that cross (about 50%, depending on closeness and p_T), and the muon identification used by the software trigger is outside-in. If a fraction of the tag and probe muons cross ($x = \#\text{crossing}/\#\text{total}$), then the efficiency measured by tag-and-probe would be lower than the true single-muon efficiency (tag-and-probe would measure $[0.5x + (1 - x)]\epsilon$ instead of the true efficiency, ϵ). Since Z bosons are produced with relatively little boost, the muons from $Z \rightarrow \mu\mu$ decays rarely overlap ($x \lesssim 0.1\%$), in addition to providing muons with momenta relevant to our signal search ($p_T \approx$ tens of GeV/c). The tag and the probe do not strictly need to be in different subsystems to avoid bias from overlaps: we know from Fig. 21 that a sufficient condition to avoid overlaps in the barrel is

$$(\Delta\phi < -0.4 \text{ or } \Delta\phi > 1) \text{ and } |\Delta z/r| > 0.3. \quad (13)$$

961 Repeating the efficiency study with this cut to avoid overlaps instead of requiring the tag to be
 962 in the endcap yields a scale factor of $94.2/97.7 = 0.964 \pm 0.004$, a systematic difference from
 963 the first study which is smaller than the statistical uncertainty.

964 Tag-and-probe studies of offline selection efficiency performed by other CMS groups yield
 965 data/MC scale factors of 1.000 ± 0.003 , so we did not repeat them for our datasets.

966 D Signal Shape Studies Using Low Mass Resonances in Data

967 Because the shapes of the dimuon invariant mass distributions are completely determined by
 968 detector resolution effects (dominated by tracking), these shapes can be obtained from actual
 969 low mass resonances directly in data. The studies in data are compared to Monte Carlo predic-
 970 tions and we use these comparisons to determine evolution of the resolution parameters.

971 We used the same dataset as in our analysis selections, but to avoid unblinding our signal
 972 regions, selected events were required to contain exactly two muons with the transverse mo-
 973 mentum of the dimuon system $p_T < 80 \text{ GeV}/c$. Additionally, we expanded the requirement

974 of at least one muon with $p_T > 15 \text{ GeV}/c$ to be within $|\eta| < 2.4$ (as opposed to $|\eta| < 0.9$
 975 in the main analysis) to include dimuons reconstructed in the overlap or endcap regions and
 976 correspondingly dropped the requirement of a central muon in the trigger selections. This is
 977 justified because resolutions are driven by tracking and not by muon or muon trigger perfor-
 978 mance. We then focus on the regions in the dimuon invariant mass spectrum around the four
 979 relevant resonances: ω , ϕ , J/ψ , and ψ' . The distributions for the selected data events are shown
 980 in Fig. 24 separately for barrel ($|\eta| < 0.9$) and forward $|\eta| > 0.9$ as resolutions in these regions
 981 are different.

We assume that the background is a linear function of mass, $p_0 + p_1 m$, and use a Crystal Ball shape to fit the shape of the resonances:

$$CB(m; m_0, \sigma, \alpha, n) = \frac{1}{\sqrt{2\pi}\sigma} \begin{cases} \exp\left(-\frac{(m-m_0)^2}{2\sigma^2}\right) & \text{if } (m-m_0)/\sigma > -\alpha \\ \exp\left(-\frac{\alpha^2}{2}\right) \left[\frac{n}{n-\alpha^2-|\alpha|(m-m_0)/\sigma}\right]^n & \text{otherwise} \end{cases} \quad (14)$$

982 The peak of the mass distribution (true mass of the particle in this parameterization) is m_0
 983 (GeV/c^2), with core resolution σ (GeV/c^2). The Crystal Ball parameter α indicates where the
 984 core Gaussian smoothly connects to a low-side $1/(m-m_0)^n$ tail (in number of standard devi-
 985 ations below the peak). In the ω fit, the ρ is included with mass and width fixed to its PDG
 986 values and allowed to float in normalization, as an additional background. Each resonance is
 987 fitted in the barrel and endcap separately, with large differences in σ observed between the two
 988 regions. Only in the J/ψ barrel fit is the Crystal Ball α parameter allowed to float (in the other
 989 seven fits, the value is fixed to the result from barrel J/ψ .)

990 To better understand the parameters of the Crystal Ball shape suitable for our analysis, we
 991 performed the same fit using simulated J/ψ events, see results shown in Fig. 25. It was found
 992 that there is a strong negative correlation between the parameters α and n , which determine the
 993 tail behavior of the function. The correlation coefficient was found to be $k = -0.9$. While this
 994 has negligible effect on the acceptance (the signal corridor is defined to be 5σ in core resolution,
 995 while variations in α and n mainly modify the shape near $\sigma \sim 2\text{--}3$) and is consistent with
 996 the measurements in data, we incorporated this correlation into the fit and used simulation
 997 prescribed parameters for α and n .

998 Results of the fits are shown in Fig. 24 overlaid on the data. Parameters of the fitted func-
 999 tion were compared to the simulation predictions and were found to be in good agreement as
 1000 shown in the main text (Fig. 9). Because mass resolutions depend on the mass, the shape of
 1001 the dependency was taken from the simulation. In addition, as shown in the main text, mass
 1002 resolutions weakly depend on the momentum (boost) of the dimuon system and we used sim-
 1003 ulation to determine the spread in the fit parameters using a broad range of dimuon momenta.
 1004 Because the spread is small and has little effect on the final results, we use it as a measure of
 1005 the systematic uncertainties in parameterizing the signal shape.

1006 E Background Composition of the Low Mass Dimuon Sample

1007 To understand the composition of the dimuon events with low invariant mass of muon pairs,
 1008 we first separate the sample into two orthogonal sub-samples: one enriched with the dimuons
 1009 from the $b\bar{b}$ production and the other depleted of the $b\bar{b}$ events. This is achieved using selections
 1010 based on isolation of the muon pair and the flight distance calculated using the common vertex

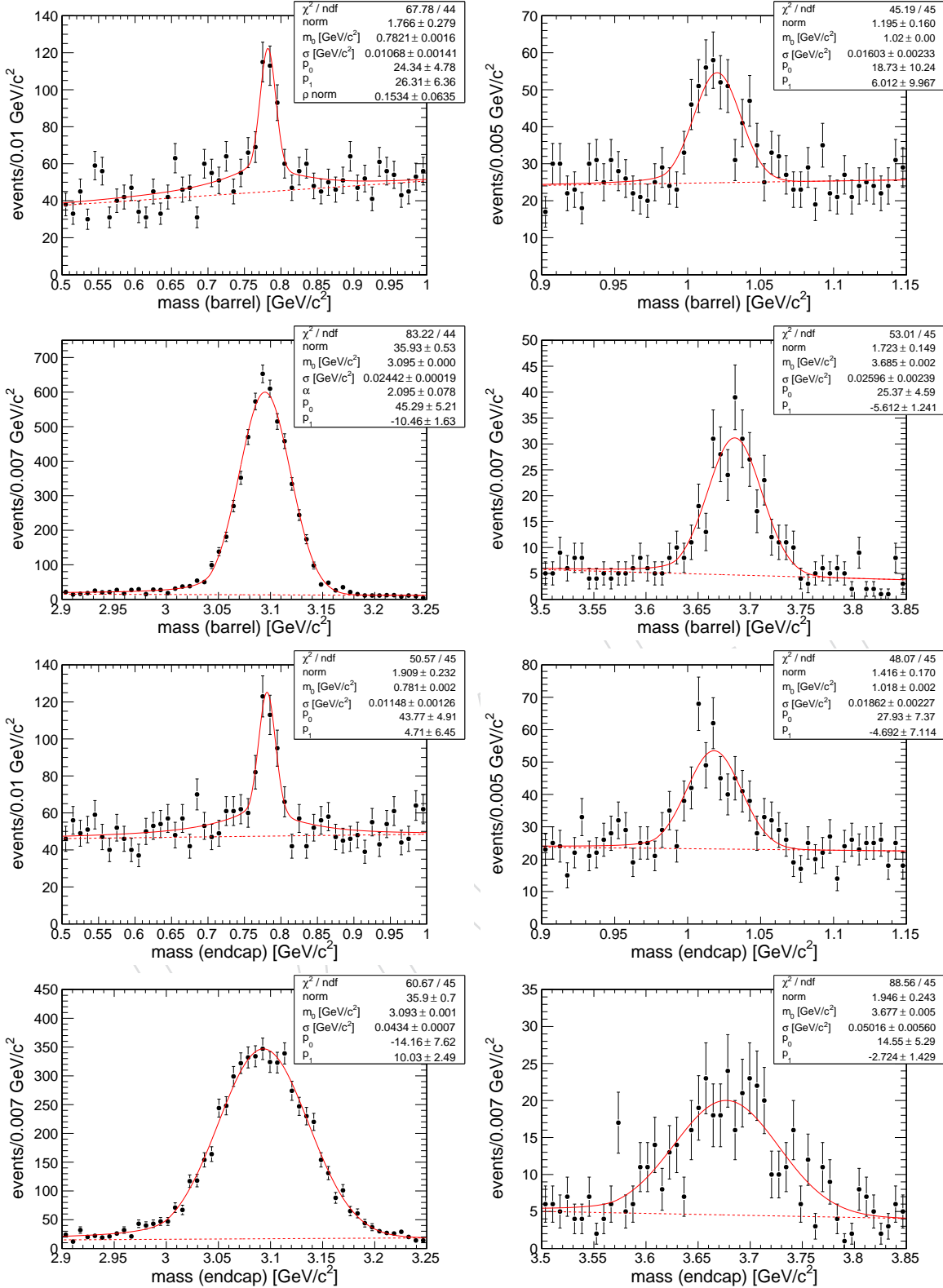


Figure 24: Four resonance mass peak fits in dimuon data: ω , ϕ , J/ψ , and ψ' in the barrel region $|\eta| < 0.9$ (top four plots) and the overlap and endcap $|\eta| > 0.9$ (bottom four). Signal shapes are fitted to Crystal Ball function with α parameter floating only in the J/ψ barrel case. Backgrounds are linear, and the ω fit has an additional ρ background component with ρ mass and width taken from the PDG.

of the two muons. We then compare events in data with the predictions based on simulated events for each of the main backgrounds: $b\bar{b}$ production, light flavor QCD multi-jet production, prompt resonance production (e.g. J/ψ) and Drell-Yan ($pp \rightarrow \gamma^* \rightarrow \mu\mu$ using Pythia 8 with no explicit low mass cut-off, although Pythia cuts it at $\sqrt{q_{\gamma^*}^2} \sim 0.35 \text{ GeV}/c^2$).

The isolation variable is defined using tracks around the dimuon system excluding both of the muons used in constructing the dimuon candidate such that the two close-by muons do not veto one another:

$$Iso = \sum_{\text{tracks}} p_T \text{ if } p_T > 1.5 \text{ GeV}/c, \Delta R < 0.4, \text{ and not a muon,} \quad (15)$$

where the p_T threshold and ΔR radius were chosen to minimize sensitivity to tracks from the pile-up and to achieve a near flat distribution of the isolation distribution for dimuons from the b -jets near $Iso = 0$ (using a simulated sample of $b\bar{b}$ MC events).

The flight distance is defined as

$$L_{xy} = \frac{(v_x - V_x)p_x + (v_y - V_y)p_y}{\sqrt{p_x^2 + p_y^2}} \quad (16)$$

where (v_x, v_y) is the 2-D position of the dimuon vertex, (p_x, p_y) is the 2-D projection of the dimuon momentum vector, and (V_x, V_y) is the 2-D position of the closest primary vertex in the z direction (z is parallel with the beamline).

Distributions for both variables, Iso and L_{xy} , are shown in Fig. 26, for the whole mass distribution $m_{\mu\mu} < 5 \text{ GeV}/c^2$, and also for two subsets of the events. The first subset is events from the “continuum” ($1.1 < m_{\mu\mu} < 2.9 \text{ GeV}/c^2$) part of the spectrum, and the second one contains events from the “low-mass” part of the spectrum ($0.35 < m_{\mu\mu} < 0.5 \text{ GeV}/c^2$). Note that the “low mass” region does not include the very low mass region of $0.25 < m_{\mu\mu} < 0.35 \text{ GeV}/c^2$. The “continuum” and “low-mass” ranges are motivated by different composition of the backgrounds as shown in Fig. 10(a), where these ranges are indicated by dotted vertical lines. As expected, Drell-Yan and prompt resonances are well isolated, while $b\bar{b}$ is not. The L_{xy} variable provides another handle on separate the long living and prompt sources of background. Drell-Yan and prompt resonances form a peak centered on $L_{xy} = 0$, while $b\bar{b}$ has a long tail toward positive L_{xy} due to the long lifetimes of B hadrons. Note that vertices with negative L_{xy} are mis-measured; this provides a direct indication of the vertex resolution. Vertex resolution degrades when the opening angle becomes small (or equivalently the low invariant mass $m_{\mu\mu}$, particularly as it approaches the kinematic threshold of $m_{\mu\mu} = 2m_\mu$), which is why the symmetric peak in the low-mass bin is wider than in all other bins.

These observations prompted us to partition the data into two regions dominated by $b\bar{b}$ and prompt/Drell-Yan, respectively (each containing resonance and continuum contributions) using the “ $b\bar{b}$ cuts” already mentioned in Eqn. 4 of the main text:

$$Iso > 4.5 \text{ GeV}/c \text{ or } L_{xy} > 2 \text{ mm}. \quad (17)$$

The ranges are indicated with dotted vertical lines in Fig. 26. Our conclusion is that the data is reasonably well described by the simulation (with the exception of some of the resonances neglected during event generation) and the two agree well for $m_{\mu\mu} > 0.35 \text{ GeV}/c^2$ with no unexpected backgrounds or other features. Small differences between the data and simulation, e.g. in the shape of isolation distributions are not a concern as we never use these cuts in the

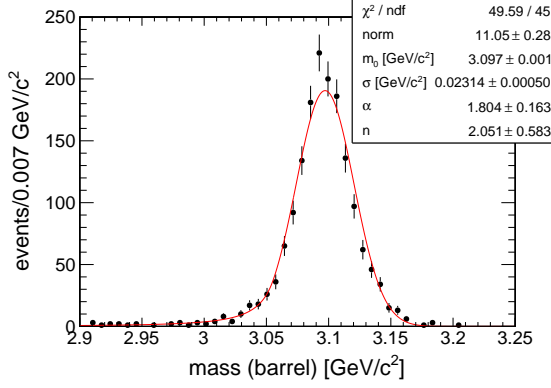


Figure 25: Fit of the J/ψ resonance mass peak using simulation to extract parameters α and n for the Crystal Ball shape and their correlation. There is a strong negative corelation ($k = -0.9$) between the two parameters, which was incorporated into the final fits of data.

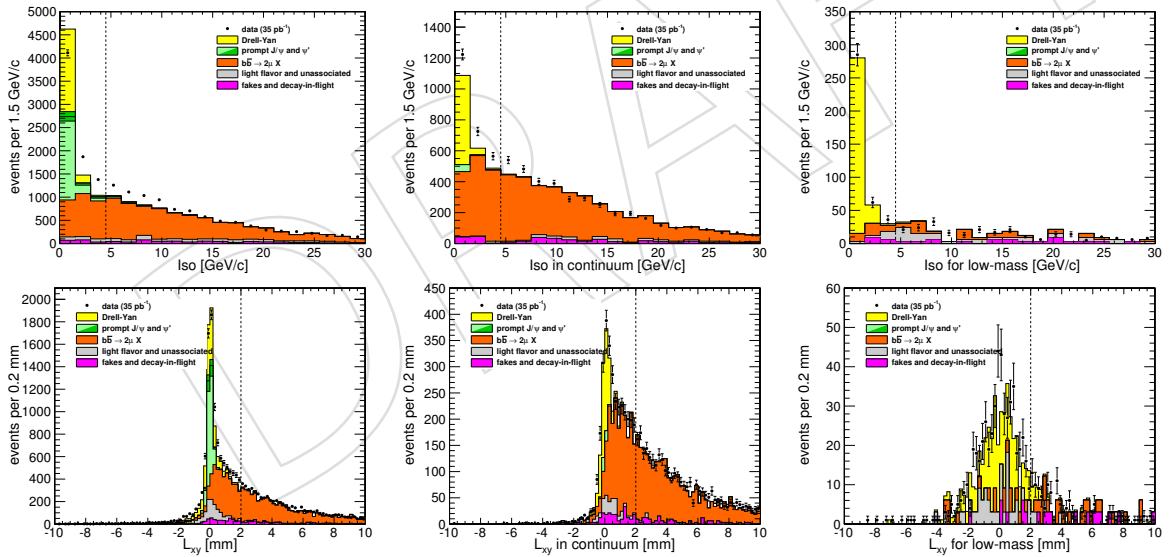


Figure 26: (a): Track-based isolation (see text for definition) for the whole sample. (b) The same distribution for events with $m_{\mu\mu} = 1.1 - 2.9 \text{ GeV}/c^2$ (the continuum), and (c): for the low mass region $m_{\mu\mu} = 0.35 - 0.5 \text{ GeV}/c^2$. (d): Distance of the dimuon vertex (in x - y) from the closest primary vertex (in z), along the direction of the dimuon momentum axis, for the whole sample, (e) distribution for events with $m_{\mu\mu} = 1.1 - 2.9 \text{ GeV}/c^2$. (f): for the low mass region $m_{\mu\mu} = 0.35 - 0.5 \text{ GeV}/c^2$. Note that the events in the “very low mass” range $0.25 < m_{\mu\mu} < 0.35 \text{ GeV}/c^2$ are not included in the low-mass or continuum plots.

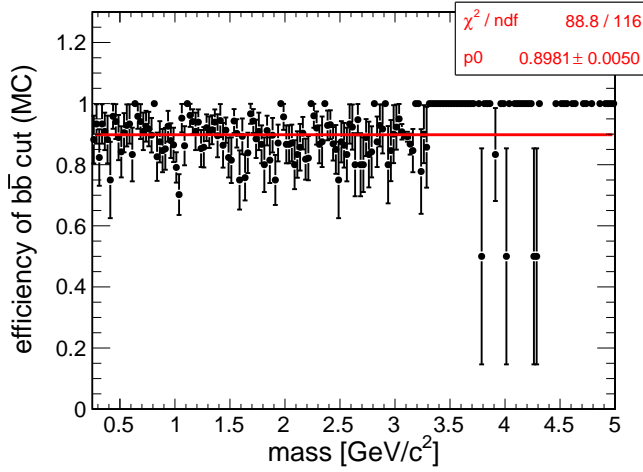


Figure 27: Efficiency of the $b\bar{b}$ cut for simulated $b\bar{b}$ events, demonstrating that the efficiency is constant, so the $b\bar{b}$ cuts do not introduce a shape bias.

1041 main analysis selections. Also, the agreement in isolation distributions is likely affected by the
 1042 lack of simulated $b\bar{b}$ events with lower \hat{p}_T (the sample used in these comparisons was generated
 1043 using $\hat{p}_T > 30 \text{ GeV}/c$).

1044 In addition to background composition studies, another use of the selections based on isolation
 1045 and flight distance is to demonstrate the approximate scaling of the dimuon invariant mass
 1046 distribution in $b\bar{b}$ events with the dimuon transverse momentum (see Fig. 11 in the main text).
 1047 This assumption is used in constructing the dimuon invariant mass template for background
 1048 events in region (a-1) and for the triggered dimuon template for background events in region
 1049 (b-1). It is therefore important to verify that these selections do not bias the shape of the dimuon
 1050 mass spectrum for $b\bar{b}$ events. Fig. 27 shows the efficiency of the $b\bar{b}$ cut versus dimuon invariant
 1051 mass using simulated $b\bar{b}$ events. The efficiency is uniform at the level of precision required for
 1052 the templates affirming the validity of our assumptions⁸

1053 E.1 The Very Low Mass Region $m_{\mu\mu} < 0.35 \text{ GeV}/c^2$

1054 In this section we discuss the properties of the events comprising the very low mass excess not
 1055 predicted by the simulated SM background processes used in this analysis. The excess has a
 1056 shape of a low-mass rise towards the lower edge of the invariant mass distribution. The excess
 1057 is very significant in the “very low mass” range $0.25 < m_{\mu\mu} < 0.35 \text{ GeV}/c^2$ and the tail of it
 1058 may be still present all the way up to $m_{\mu\mu} \sim 0.55 \text{ GeV}/c^2$.

1059 The shape of the “excess” is clearly not consistent with a dimuon resonance as could be con-
 1060 cluded from our studies of signal shapes (Sec. 3.4 and D) that extend to very low masses, which
 1061 indicate that a resonance will have a very narrow shape. In our nomenclature, the excess is only
 1062 present in the “ $b\bar{b}$ -enhanced” region while in the “ $b\bar{b}$ -depleted” sample a similar rise is consis-
 1063 tent with being the low mass DY events and the residual excess below $m_{\mu\mu} = 0.35 \text{ GeV}/c^2$ is
 1064 a likely artifact of the default low mass $\sqrt{q^2} \sim 0.35 \text{ GeV}/c^2$ cut-off in the Pythia 8 Drell-Yan
 1065 generation. However, at such low invariant masses our definition of the $b\bar{b}$ enriched samples
 1066 becomes not fully appropriate as the L_{xy} resolution becomes very poor for boosted dimuons
 1067 as the two muon tracks are nearly parallel. One can see that effect by comparing Figs. 26(d)

⁸Note that the use of both L_{xy} and Iso variables leads to a more uniform efficiency as compared to the case of using isolation only, although the bias in the latter case is not too large.

and (f), showing the L_{xy} resolution for simulated DY events in continuum and for the mass range $0.25 < m_{\mu\mu} < 0.35 \text{ GeV}/c^2$. For lower masses, the L_{xy} resolution quickly deteriorates becoming very broad. As a result, our “ $b\bar{b}$ cuts” continue being appropriate for selecting an enriched sample of $b\bar{b}$ events, but no longer constraints the DY events to the $b\bar{b}$ -depleted sample as the requirement of $L_{xy} > 2 \text{ mm}$ divides DY events in almost equal fractions between the “ $b\bar{b}$ -enriched” and the “ $b\bar{b}$ -depleted” subsets. Therefore, to study the very low mass excess, we partition the sample into $b\bar{b}$ -enriched and DY-enriched samples using isolation only, $I_{\text{so}} < 4.5 \text{ GeV}/c$ for the DY-enriched and $I_{\text{so}} \geq 4.5 \text{ GeV}/c$ for the $b\bar{b}$ -enriched subsamples. The distributions of invariant mass of the dimuon system for the two subsamples is shown in Figs. 28(a) and (b). It is very evident now that the bulk of the excess is due to the unsimulated DY events at very low Q^2 . Although there is a residual excess in the non-isolated subsample, which we are still studying, this unknown background component is absolutely inconsistent with signal due to its broad shape and constitutes less than 20% of all backgrounds in that region making it have no effect on the analysis results. Figures. 28(c) and (d) show the L_{xy} distribution for the very low mass events in isolated and non-isolated subsets reaffirming our earlier observations about degradation of the L_{xy} resolution at very low masses (note that the units on x -axis being cm and not mm as in other L_{xy} plots). It also shows that the residual background events in the non-isolated sample are prompt and very similar to DY events in the isolated samples in terms of L_{xy} distribution.

We therefore conclude that the bulk of the “excess” in the very low mass region is understood and is due to Drell-Yan events with very low $Q^2(\gamma^*)$ not generated in our DY simulated samples. The remaining excess is DY-like (except it appears to be not isolated, which perhaps could indicate either an off-shell photon production in jets or a tracking reconstruction artefact in the environment of two very close tracks) and is small compared to the overall size of the background in that region (less than 20%), which is well within the margin of our systematic uncertainties.

1094 F Supporting plots for background mass templates

1095 F.1 Dimuon Mass Spectrum for Misidentified Muons in Simulation

Dimuon invariant mass templates for background events in regions (a-2) and (a-3), containing high multiplicity mu-jets, has a component where a dimuon candidate originates from hadronic tracks that are misidentified as muons. While we measure the actual invariant mass distribution for pairs of misidentified muons directly from the data (see Sec. 4.3), it is nevertheless interesting to compare data driven results with the simulation predictions. The source of misidentified muons has two main components: a π^\pm , K^\pm , or (more rarely) strange baryon decays within the detector, and due to accidental matches of tracks with hits in the muon chambers. We use the simulated muon enriched QCD multi-jet sample to construct dimuon candidates using reconstruction level information. We then select dimuon candidates reconstructed from misidentified muons from each of these two categories. For the first category (decays in flight), we identify reconstructed muons matched to a generator-level muon whose parent is a long-lived hadron to select misidentified muons. For the second category, we identify reconstructed muon candidates with no generator-level match. Figure 29 shows the invariant mass spectra for dimuon candidates constructed using misidentified muons of each type. Evidently, the spectra are very similar to one another, and also similar to the mass templates derived from data in Sec. 4.3 reaffirming validity of our background modeling procedure.

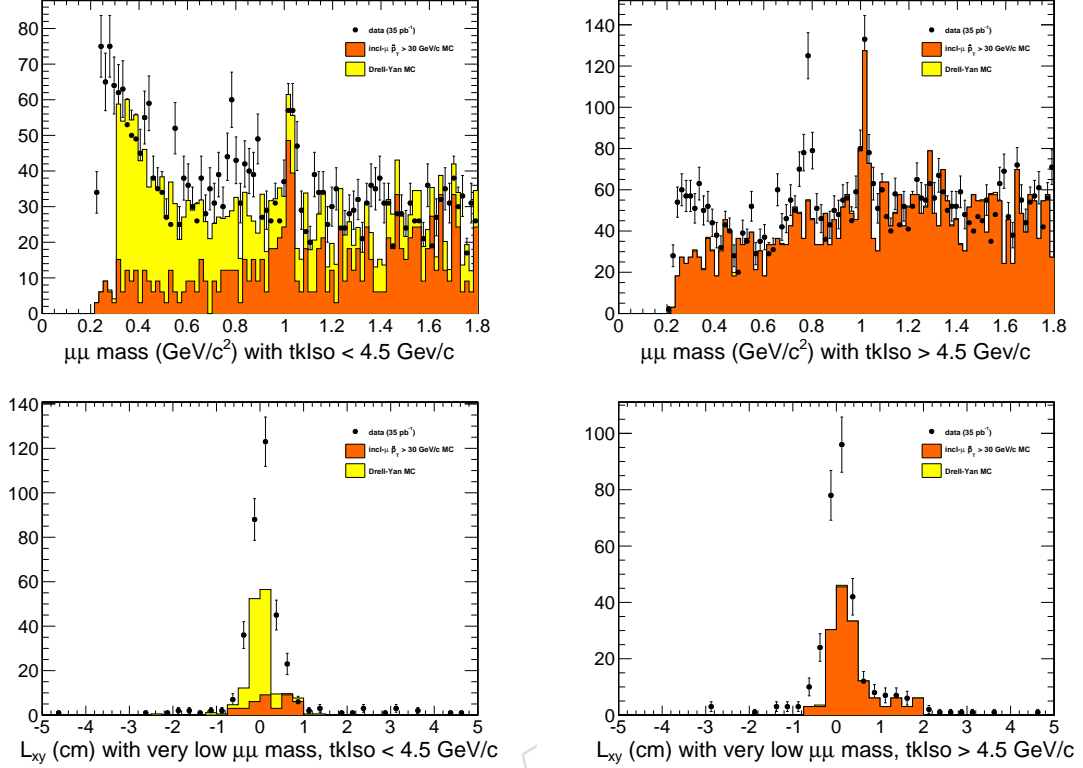


Figure 28: (a): Invariant mass distribution for events with $Iso < 4.5 \text{ GeV}/c$. (b): The same distribution for $Iso \geq 4.5 \text{ GeV}/c$. (c): L_{xy} distribution for isolated ($Iso < 4.5 \text{ GeV}/c$) events in the very low mass region $0.25 < m_{\mu\mu} < 0.35 \text{ GeV}/c^2$. (d): L_{xy} distribution for non-isolated events in the very low mass region.

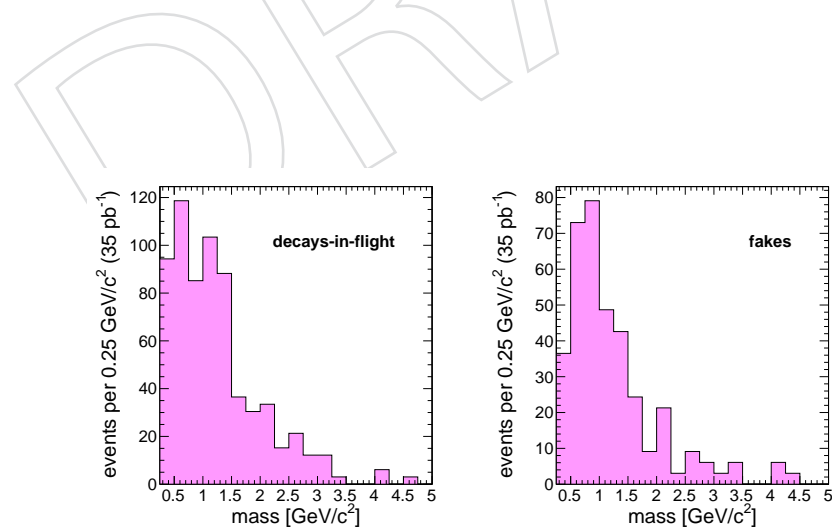


Figure 29: Distributions of dimuon mass for dimuons containing decay-in-flight and fake muons in inclusive-muon Monte Carlo.

1112 F.2 Weighting procedure for triggered and other dimuons (b-1)

1113 In events with two well-separated dimuons (b-1), at least one of the two dimuons must contain
 1114 a trigger muon, which introduces an asymmetry between the two dimuons with implications
 1115 for the shape of the mass spectrum (discussed in Sec. 4.4). Sometimes, however, both dimuons
 1116 contain a trigger: in that case, we randomly assign the labels “triggered” and “other.” While
 1117 this has no effect on the shape of the triggered dimuon mass spectrum, the triggerable part of
 1118 the other dimuon mass spectrum becomes depleted by a factor of $\frac{1}{2}$. To produce the correct
 1119 mass templates, we make the same correction in the background-enriched samples used to
 1120 construct the templates: events in the “other dimuon” template with a muon with the right
 1121 kinematics to satisfy the trigger ($p_T > 5 \text{ GeV}/c$ and $|\eta| < 0.9$) are weighted by $\frac{1}{2}$. Note that the
 1122 final analysis fit requires no weighting.

1123 To demonstrate that this weighting procedure produces the correct templates, we performed
 1124 two toy Monte Carlos, one with uniform distributions (to see the bias by eye) and another with
 1125 more realistic distributions. Background-enriched samples and background-in-signal-region
 1126 samples were simulated independently, but with the same distributions as each other. The
 1127 uniform toy Monte Carlo was simulated by throwing random p_T and η variables uniformly
 1128 in $0\text{--}50 \text{ GeV}/c$ and $|\eta| < 2.4$, respectively, in three cases: background-enriched for trigger,
 1129 background-enriched for other, and a 2D distribution $(p_{T1}, p_{T2}, \eta_1, \eta_2)$ for the signal region.
 1130 The background-enriched for trigger sample was required to satisfy a simulated trigger ($p_T >$
 1131 $15 \text{ GeV}/c$ and $|\eta| < 0.9$) while the background-enriched for other was not. The background-
 1132 enriched for other events were weighted by a factor of $\frac{1}{2}$ if they happened to satisfy the trigger,
 1133 however. The signal region simulation was required to satisfy the trigger ($(p_{T1} > 15 \text{ GeV}/c$ and
 1134 $|\eta_1| < 0.9)$ or $(p_{T2} > 15 \text{ GeV}/c$ and $|\eta_2| < 0.9)$), and the dimuons 1 and 2 were assigned labels
 1135 “triggered” and “other” the same way as in data: if only one dimuon satisfied the trigger, it was
 1136 labeled “triggered” and the other was labeled “other,” but if both satisfied the trigger, then the
 1137 labels were randomly assigned. The left-side plots in each of the four groups in Fig. 30 shows
 1138 background-enriched samples from the uniform toy MC (red lines) overlaid on projections of
 1139 the signal samples (black points) from the uniform toy MC, adjusted for overall normalization.
 1140 Each of the four groups shows a different variable: triggered p_T , triggered η , other p_T , and
 1141 other η . The trigger cuts are evident in the triggered samples and the $\frac{1}{2}$ weighting factor is
 1142 evident in the background-enriched other sample. It is also easy to see that this weighting
 1143 exactly compensates for the bias in the signal from randomly assigning labels in the cases with
 1144 two triggered dimuons.

1145 For a more realistic demonstration, the toy Monte Carlo was repeated with realistic distribu-
 1146 tions taken from $b\bar{b}$ Monte Carlo, though the same procedure was applied. These plots are
 1147 shown on the right-side of each of the four groups in Fig. 30. Though it is more difficult to see
 1148 the sculpting due to randomly assigning “triggered” and “other” labels, it is clear that the simu-
 1149 lated background-enriched samples pass through the projections of the simulated background-
 1150 in-signal region distributions.

1151 F.3 Correlations in Fragmentation of the b -jets in $b\bar{b}$ Events

1152 Two-dimensional background mass templates for signal region (b-1) are constructed from 1D
 1153 background-enriched samples by forming a Cartesian product of the 1D dimuon mass distribu-
 1154 tions. Such a procedure is based on the assumption that the two dimuon mass distributions are
 1155 independent in the signal region. For $b\bar{b}$ events (the dominant background in the (b-1) region),
 1156 this is equivalent to assuming that the decays of the two b -quarks and subsequent sculpting
 1157 of their distributions with muon p_T and η cuts are independent. This seems fairly obvious as

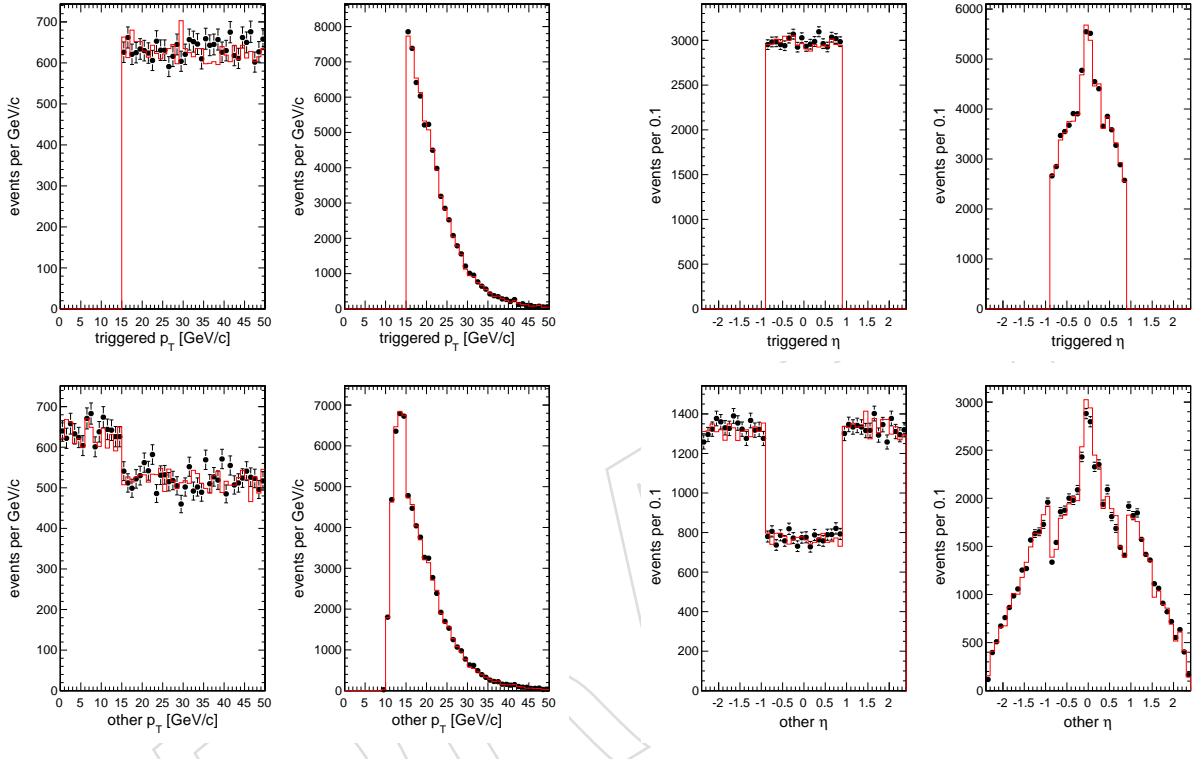


Figure 30: Toy Monte Carlo simulation of backgrounds in the dimuon-dimuon sample (black points), extrapolated from single-dimuons and dimuon-plus-muon background-enriched samples (red lines). In each pair of plots, the left is a simplified model with uniform p_T and η distributions and the right is a model with realistic p_T and η distributions. The “other dimuon” distribution is depleted in the signal region, but the background-enriched sample is weighted to have the same distribution.

1158 fragmentation of each b -quark should wash away any long range correlations before jet had-
 1159 ronization, yet we decided to verify this explicitly.

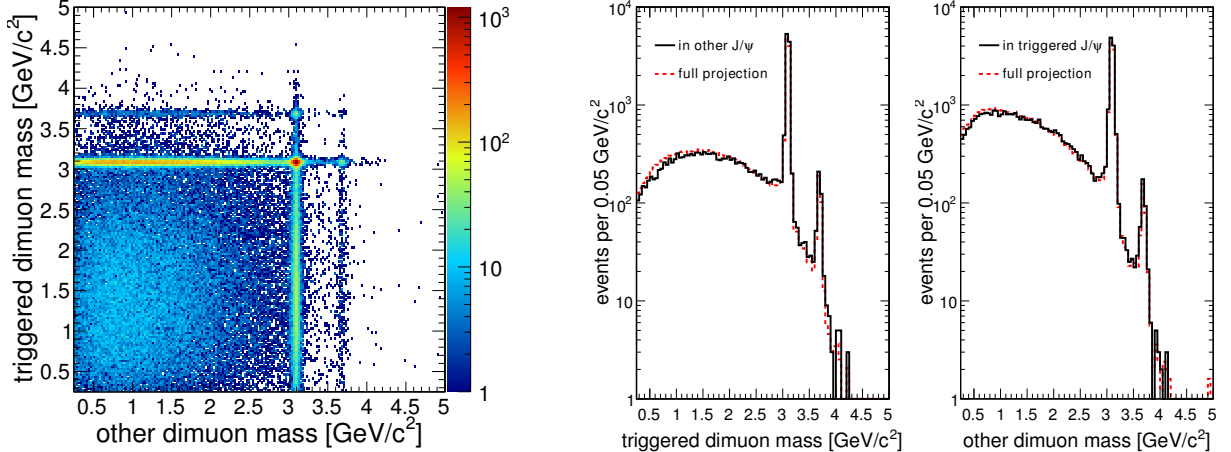


Figure 31: A Monte Carlo simulation of $b\bar{b} \rightarrow 2\mu 2\mu X$ events to demonstrate the factorization of background mass distributions. Left: the 2-D distribution. Right: projected distributions in a slice around the J/ψ and the whole distribution, normalized to equal areas.

1160 To test this, we generated a large sample of $b\bar{b} \rightarrow 2\mu 2\mu$ MC events (with full detector simula-
 1161 tion), large enough to see any failure in factorization by eye. After reconstructing the dimuon
 1162 candidates, in Fig. 31(a) we plot the 2D distribution of invariant masses for the triggered and
 1163 other dimuons. The plot shows the expected asymmetry in the mass spectrum due to scalpt-
 1164 ing of the trigger dimuon distribution by the requirement of an energetic muon, but no visible
 1165 correlations between the reconstructed masses of the two dimuons. To highlight any possible
 1166 correlation between the invariant masses of the two dimuons, Fig. 31(b) shows a 1D projection
 1167 of the distribution onto the y -axis (invariant mass of the triggered dimuon) for the entire dataset
 1168 (dashed red histogram) compared to the same projection but only for events in a narrow slice
 1169 in the x -direction near the J/ψ mass (solid black line) scaled up to have about the same normal-
 1170 ization as the full projection. Again, the mass spectra are nearly identical showing no evidence
 1171 of unexpected correlations. Fig. 31(c) shows the similarly defined distributions, but projected
 1172 onto the other dimuon mass axis.

1173 G Categorization efficiencies in various benchmark models

1174 The following tables present model acceptances as a function of \tilde{q} mass and γ_D branching
 1175 fraction to muons. Table 6 presents an NMSSM sample point (Sec. 2.3), Table 7 presents SUSY
 1176 dark matter with a $\mathcal{U}(1)_{\text{dark}}$ symmetry (Sec. 2.1), and Tables 8 and 9 present the Dark Fermion
 1177 Cascades model of Sec. 2.2. As a reminder, the (a-1) signal region is exactly one mu-jet with
 1178 exactly two muons and $p_T^{\mu\mu} > 80$ GeV/ c , (a-2) is exactly one mu-jet with exactly four muons
 1179 (two opposite-sign dimuons), (b-1) is exactly two mu-jets each containing two muons (four
 1180 total), and the $> 4\mu$ category represents all events with more than four muons contained in
 1181 mu-jets (sum of (a-3), (b-2), and (c-1)).

1182 H Event displays

1183 Figures 32 and 33 show sample events in the (a-2) and (b-1) control regions. There were no
 1184 events with equal-mass dimuons (or any larger numbers of muons than four).

Table 6: NMSSM model acceptances in percent with $\mathcal{B}(a \rightarrow \mu\mu) = 100\%$ hypothesis and separately for $m_h = 100 \text{ GeV}/c^2$ and $m_a = 2 \text{ GeV}/c^2$, where one of them is fixed and another one is variable (the case when $m_h = 100 \text{ GeV}/c^2$ and $m_a = 2 \text{ GeV}/c^2$ simultaneously duplicates the information in Table 2). Variable masses m_a and m_h are given in the first column (in GeV/c^2). Acceptance in regions with four muons ((a-2) and (b-1), labeled with asterisks) is restricted to the diagonal of the dimuon-dimuon space (within 5σ in detector resolution: $\sigma(m) = (0.026 + 0.0065 b m) \text{ GeV}/c^2$, where $b = 1$ for barrel and $b = 2$ for endcap).

m_a	NMSSM with $m_h = 100 \text{ GeV}/c^2$			
	(a-1)	(a-2)	(b-1)	$> 4\mu$
0.3	0.9	0.0	40.6	0.0
0.5	1.4	0.0	30.9	0.0
1.0	1.5	0.0	25.9	0.0
2.0	1.7	0.0	23.8	0.0
4.0	1.6	0.0	23.6	0.0

m_h	NMSSM with $m_a = 2 \text{ GeV}/c^2$			
	(a-1)	(a-2)	(b-1)	$> 4\mu$
85	1.2	0.0	20.4	0.0
100	1.7	0.0	23.8	0.0
120	2.5	0.0	28.9	0.0

CMS Experiment at LHC, CERN
Data recorded: Mon Oct 11 16:03:58 2010 CDT
Run/Event: 147754 / 142156381
Lumi section: 115
Orbit/Crossing: 30005881 / 1255

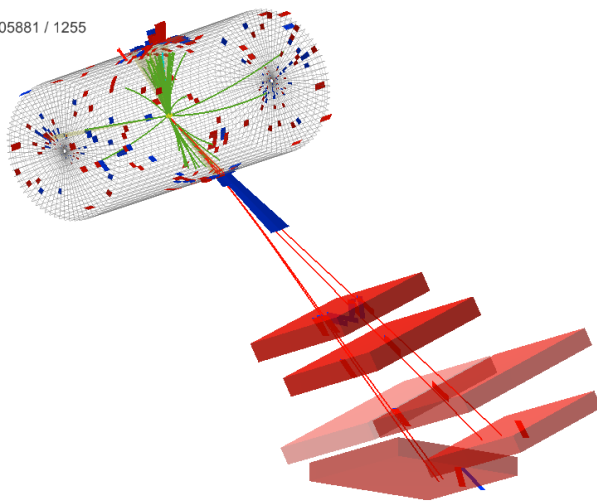


Figure 32: The event in the (a-2) region. The two dimuons are not close enough in mass to be decays of the same on-shell m_1 boson (and therefore belong to the off-diagonal control).

Table 7: Dark matter with $\mathcal{U}(1)_{\text{dark}}$ model acceptances (%) for three sample $\mathcal{B}(a \rightarrow \mu\mu)$ hypotheses and two masses of γ_{dark} (the case when $\mathcal{B}(a \rightarrow \mu\mu) = 100\%$, $m_{\tilde{g}} = 1200 \text{ GeV}/c^2$, and $m_{\tilde{\chi}_{\text{dark}}} = 1.0 \text{ GeV}/c^2$ duplicates information in Table 2). The gluino, which is the top of the cascade produced in the pp collision, has a mass given in the first column (in GeV/c^2), $m(\tilde{\chi}_{\text{dark}}) = 300 \text{ GeV}/c^2$. Acceptance in regions with four muons ((a-2) and (b-1), labeled with asterisks) is restricted to the diagonal of the dimuon-dimuon space (within 5σ in detector resolution: $\sigma(m) = (0.026 + 0.0065 b m) \text{ GeV}/c^2$, where $b = 1$ for barrel and $b = 2$ for endcap).

\tilde{g} mass	U(1) with $m_{\gamma_{\text{dark}}} = 1.0 \text{ GeV}/c^2$											
	Br($a \rightarrow \mu\mu$) = 100%				Br($a \rightarrow \mu\mu$) = 50%				Br($a \rightarrow \mu\mu$) = 33%			
	(a-1)	(a-2)	(b-1)	> 4 μ	(a-1)	(a-2)	(b-1)	> 4 μ	(a-1)	(a-2)	(b-1)	> 4 μ
500	5.9	4.2	14.3	40.0	10.6	3.1	8.7	6.3	9.2	1.8	4.7	1.9
600	6.0	4.5	14.1	41.7	11.0	3.3	9.1	6.8	9.4	1.9	4.9	2.2
800	6.6	4.8	15.2	43.2	12.3	4.1	9.6	6.4	10.5	1.9	5.3	1.9
1000	7.4	4.9	15.3	44.1	13.1	3.9	10.2	7.0	12.2	2.5	6.1	2.0
1200	7.4	5.1	15.4	45.3	15.1	4.1	10.5	6.6	13.5	2.3	5.7	2.2

\tilde{g} mass	U(1) with $m_{\gamma_{\text{dark}}} = 0.5 \text{ GeV}/c^2$											
	Br($a \rightarrow \mu\mu$) = 100%				Br($a \rightarrow \mu\mu$) = 50%				Br($a \rightarrow \mu\mu$) = 33%			
	(a-1)	(a-2)	(b-1)	> 4 μ	(a-1)	(a-2)	(b-1)	> 4 μ	(a-1)	(a-2)	(b-1)	> 4 μ
500	4.9	3.8	19.0	39.9	10.7	3.0	10.5	6.3	10.0	1.5	5.8	1.7
600	5.3	3.7	19.1	41.2	11.4	3.5	10.4	6.6	10.2	2.3	5.5	2.3
800	5.5	4.3	19.7	42.6	12.5	3.5	11.1	6.6	11.2	2.1	6.0	2.0
1000	6.3	4.3	19.7	43.3	14.4	3.7	11.2	6.9	12.9	1.9	6.6	2.5
1200	6.6	4.4	18.4	44.6	14.4	4.0	11.4	7.0	13.6	2.0	6.7	2.3

Table 8: Dark Fermion Cascades model acceptances (%) with only $\gamma_D \rightarrow \mu\mu$ (no $h_D \rightarrow \gamma_D \gamma_D \rightarrow 4\mu$), for three sample $\mathcal{B}(a \rightarrow \mu\mu)$ hypotheses (the case when $\mathcal{B}(a \rightarrow \mu\mu) = 100\%$ and $m_{\tilde{q}} = 400 \text{ GeV}/c^2$ duplicates information in Table 2). The squark, which is the top of the cascade produced in the pp collision, has a mass given in the first column (in GeV/c^2). Acceptance in regions with four muons ((a-2) and (b-1), labeled with asterisks) is restricted to the diagonal of the dimuon-dimuon space (within 5σ in detector resolution: $\sigma(m) = (0.026 + 0.0065 b m) \text{ GeV}/c^2$, where $b = 1$ for barrel and $b = 2$ for endcap).

\tilde{q} mass	$n_2(\rightarrow n_1 \gamma_D)$											
	$\text{Br}(\gamma_D \rightarrow \mu\mu) = 100\%$				$\text{Br}(\gamma_D \rightarrow \mu\mu) = 50\%$				$\text{Br}(\gamma_D \rightarrow \mu\mu) = 33\%$			
	(a-1)	(a-2)	(b-1)	> 4 μ	(a-1)	(a-2)	(b-1)	> 4 μ	(a-1)	(a-2)	(b-1)	> 4 μ
200	8.1	0.2	25.0	0.2	6.7	0.2	6.4	0.0	5.0	0.1	3.0	0.0
250	11.5	0.2	31.1	0.2	10.0	0.2	8.0	0.0	7.2	0.1	4.0	0.0
300	13.6	0.3	35.1	0.2	12.8	0.3	9.1	0.0	9.9	0.2	4.2	0.0
350	15.8	0.3	38.2	0.4	15.7	0.3	9.7	0.0	12.9	0.1	4.5	0.0
400	17.4	0.2	40.6	0.3	17.7	0.2	10.4	0.0	13.9	0.1	4.6	0.0
450	18.4	0.2	42.0	0.3	19.8	0.2	11.0	0.0	16.1	0.1	4.9	0.0
500	19.8	0.3	43.5	0.3	21.8	0.3	10.7	0.0	16.9	0.1	4.8	0.0
550	20.4	0.1	43.0	0.4	22.4	0.1	11.4	0.0	18.4	0.1	5.1	0.0
600	21.5	0.3	43.3	0.3	24.1	0.3	11.5	0.0	19.3	0.1	4.8	0.0
650	21.6	0.1	43.3	0.4	25.3	0.1	11.3	0.0	19.9	0.1	5.5	0.0

Table 9: Dark Fermion Cascades model acceptances (%) with only $h_D \rightarrow \gamma_D \gamma_D \rightarrow 4\mu$ (no direct $\gamma_D \rightarrow \mu\mu$), for three sample $\mathcal{B}(a \rightarrow \mu\mu)$ hypotheses (the case when $\mathcal{B}(a \rightarrow \mu\mu) = 100\%$ and $m_{\tilde{q}} = 400 \text{ GeV}/c^2$ duplicates information in Table 2). The squark, which is the top of the cascade produced in the pp collision, has a mass given in the first column (in GeV/c^2). Acceptance in regions with four muons ((a-2) and (b-1), labeled with asterisks) is restricted to the diagonal of the dimuon-dimuon space (within 5σ in detector resolution: $\sigma(m) = (0.026 + 0.0065 b m) \text{ GeV}/c^2$, where $b = 1$ for barrel and $b = 2$ for endcap).

\tilde{q} mass	$n_2 \rightarrow n_1 h_D(\rightarrow 2\gamma_D)$											
	$\text{Br}(\gamma_D \rightarrow \mu\mu) = 100\%$				$\text{Br}(\gamma_D \rightarrow \mu\mu) = 50\%$				$\text{Br}(\gamma_D \rightarrow \mu\mu) = 33\%$			
	(a-1)	(a-2)	(b-1)	> 4 μ	(a-1)	(a-2)	(b-1)	> 4 μ	(a-1)	(a-2)	(b-1)	> 4 μ
200	0.2	5.9	0.7	43.1	1.3	4.1	3.6	8.1	1.5	2.0	2.9	2.9
250	0.4	6.1	0.6	52.1	2.4	5.1	5.2	10.4	2.6	2.8	3.7	3.6
300	0.6	6.8	0.6	56.8	4.0	5.9	5.9	11.8	4.2	3.1	4.7	3.9
350	0.7	6.9	0.6	60.2	5.5	6.3	6.9	13.0	5.3	3.3	5.2	4.9
400	0.9	6.6	0.7	63.1	6.8	6.2	7.1	13.6	7.6	3.6	5.4	4.8
450	1.0	6.7	0.6	64.2	8.4	6.5	7.4	14.0	9.2	4.0	5.5	4.9
500	1.1	7.3	0.5	64.5	10.0	7.2	7.3	13.9	10.6	4.1	5.7	4.4
550	1.5	7.5	0.7	64.8	10.8	6.6	7.5	14.0	11.8	3.8	5.8	4.9
600	1.8	7.6	0.7	64.1	11.8	6.3	7.5	13.9	13.1	3.7	5.4	4.6
650	2.0	7.8	0.8	62.9	13.1	6.5	7.2	13.1	14.0	4.0	5.2	4.4

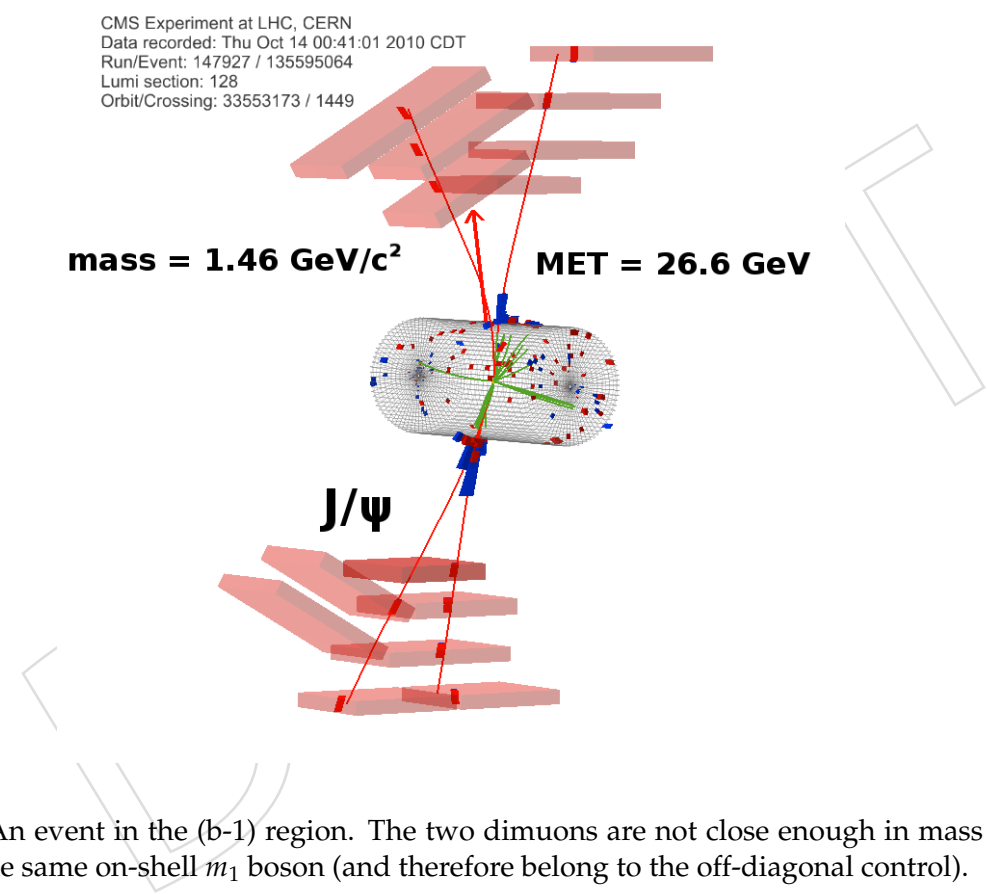


Figure 33: An event in the (b-1) region. The two dimuons are not close enough in mass to be decays of the same on-shell m_1 boson (and therefore belong to the off-diagonal control).

1185 | Tables of background templates parameters

Table 10: R_2^1 BG template fit results.

$\sigma_{J/\psi}$	0.0279 ± 0.0013
σ_ω	0.01
p_{1/m^2}	135 ± 65
p_ω	16.3 ± 6.3
p_ϕ	8.9 ± 5.8
$p_{J/\psi}$	492 ± 23
$p_{\psi'}$	21.5 ± 5.6
p_{poly}	1084 ± 75
σ_ϕ	0.01
p_1	0.57 ± 0.39
p_2	1.00
p_3	0.86 ± 0.78
p_4	0.00
p_5	0.00
p_6	0.080 ± 0.028
$\sigma_{\psi'}$	0.03

Table 11: R^1_2 BG template fit correlation matrix.

	$\sigma_{J/\psi}$	p_{1/m^2}	p_ω	p_ϕ	$p_{J/\psi}$	$p_{\psi'}$	p_{poly}	p_1	p_3	p_6
$\sigma_{J/\psi}$	1.000	0.055	-0.002	-0.009	0.136	0.028	-0.092	-0.087	-0.136	0.078
p_{1/m^2}	0.055	1.000	0.116	0.039	0.039	0.063	-0.874	-0.897	-0.716	0.648
p_ω	-0.002	0.116	1.000	0.032	-0.002	-0.001	-0.152	-0.101	-0.037	0.049
p_ϕ	-0.009	0.039	0.032	1.000	-0.007	-0.010	-0.091	0.003	0.062	-0.038
$p_{J/\psi}$	0.136	0.039	-0.002	-0.007	1.000	0.021	-0.067	-0.062	-0.097	0.054
$p_{\psi'}$	0.028	0.063	-0.001	-0.010	0.021	1.000	-0.085	-0.095	-0.131	0.103
p_{poly}	-0.092	-0.874	-0.152	-0.091	-0.067	-0.085	1.000	0.816	0.663	-0.591
p_1	-0.087	-0.897	-0.101	0.003	-0.062	-0.095	0.816	1.000	0.914	-0.772
p_3	-0.136	-0.716	-0.037	0.062	-0.097	-0.131	0.663	0.914	1.000	-0.754
p_6	0.078	0.648	0.049	-0.038	0.054	0.103	-0.591	-0.772	-0.754	1.000

J Monte Carlo datasets for various benchmark models and Drell-Yan process

K Validation of 7 TeV Monte Carlo sample for SUSY with Extra- $\mathcal{U}(1)_{\text{dark}}$ model

1190 A fragment of a generator particles list for sample with $m(\tilde{g}) = 800 \text{ GeV}/c^2$, $m(\tilde{\chi}_{\text{dark}}) = 300$
 1191 GeV/c^2 , $m(a_{\text{dark}}) = 1 \text{ GeV}/c^2$, and $m(h_{\text{dark}}) = 3 \text{ GeV}/c^2$ validates the momenta of colliding
 1192 protons and sample specific masses:

Table 12: R_4^1 BG template fit results (mu+mu BG template).

$\sigma_{J/\psi}$	0.0200 ± 0.0039
σ_ω	0.01
p_{1/m^2}	76 ± 48
p_ω	10.6 ± 4.7
p_ϕ	18.7 ± 5.6
$p_{J/\psi}$	23.5 ± 5.2
$p_{\psi'}$	3.4 ± 2.1
p_{poly}	267 ± 52
σ_ϕ	0.01
p_1	0.05 ± 0.60
p_2	1.00
p_3	0.00
p_4	0.00
p_5	0.04 ± 0.18
p_6	0.00 ± 0.99
p_7	0.00
p_8	0.00
p_9	0.0027 ± 0.0052
$\sigma_{\psi'}$	0.03

Table 13: R_4^1 BG template fit correlation matrix (mu+mu BG template).

	$\sigma_{J/\psi}$	p_{1/m^2}	p_ω	p_ϕ	$p_{J/\psi}$	$p_{\psi'}$	p_{poly}	p_1	p_5	p_6	p_9
$\sigma_{J/\psi}$	1.000	0.063	-0.004	-0.012	0.131	-0.021	-0.071	-0.074	-0.131	0.108	-0.035
p_{1/m^2}	0.063	1.000	0.073	-0.029	0.059	-0.110	-0.929	-0.952	-0.495	0.379	-0.374
p_ω	-0.004	0.073	1.000	0.023	-0.004	0.010	-0.118	-0.069	0.030	-0.037	-0.013
p_ϕ	-0.012	-0.029	0.023	1.000	-0.011	0.024	-0.018	0.045	0.093	-0.087	0.029
$p_{J/\psi}$	0.131	0.059	-0.004	-0.011	1.000	-0.021	-0.066	-0.069	-0.124	0.103	-0.033
$p_{\psi'}$	-0.021	-0.110	0.010	0.024	-0.021	1.000	0.095	0.133	0.285	-0.307	0.076
p_{poly}	-0.071	-0.929	-0.118	-0.018	-0.066	0.095	1.000	0.911	0.460	-0.347	0.355
p_1	-0.074	-0.952	-0.069	0.045	-0.069	0.133	0.911	1.000	0.581	-0.466	0.383
p_5	-0.131	-0.495	0.030	0.093	-0.124	0.285	0.460	0.581	1.000	-0.977	0.312
p_6	0.108	0.379	-0.037	-0.087	0.103	-0.307	-0.347	-0.466	-0.977	1.000	-0.282
p_9	-0.035	-0.374	-0.013	0.029	-0.033	0.076	0.355	0.383	0.312	-0.282	1.000

1201	531		1000022	-	~chi_10		415		233.026	0.291	1.721		68.729	400.003	
1202	542		1000022	-	~chi_10		506		178.187	0.330	2.749		59.792	400.003	
1203	...														
1204	556		27	-	P27		531		33.779	1.376	-2.124		62.619	1.000	
1205	557		1000028	-	P1000028		531		259.713	0.024	1.637		6.110	300.000	
1206	558		28	-	P28		542		39.991	-0.910	-0.607		-41.647	3.000	
1207	559		1000028	-	P1000028		542		217.431	0.451	2.710		101.439	300.000	
1208	560		13	-	mu-		556		7.829	1.359	-2.074		14.230	0.106	
1209	561		-13	-	mu+		556		25.963	1.381	-2.139		48.389	0.106	
1210	562		27	-	P27		558		26.715	-0.885	-0.636		-26.856	1.000	
1211	563		27	-	P27		558		13.309	-0.958	-0.549		-14.790	1.000	
1212	564		13	-	mu-		562		3.691	-0.833	-0.708		-3.442	0.106	
1213	565		-13	-	mu+		562		23.035	-0.893	-0.624		-23.415	0.106	
1214	566		13	-	mu-		563		5.581	-1.004	-0.621		-6.591	0.106	
1215	567		-13	-	mu+		563		7.753	-0.921	-0.497		-8.199	0.106	

Table 14: R_4^1 BG template fit results (track+track BG template).

μ_{peak}	0.592 ± 0.058
σ_{peak}	0.30 ± 0.11
p_{gaus}	140 ± 34
p_{poly}	259 ± 35
p_1	1.00 ± 0.74
p_2	1.00
p_3	0.00
p_4	0.163 ± 0.092
p_5	0.00
p_6	0.022 ± 0.021

Table 15: R_4^1 BG template fit correlation matrix (track+track BG template).

	μ_{peak}	σ_{peak}	p_{gaus}	p_{poly}	p_1	p_4	p_6
μ_{peak}	1.000	-0.475	-0.201	0.191	-0.017	-0.137	0.003
σ_{peak}	-0.475	1.000	0.750	-0.713	0.017	0.503	-0.015
p_{gaus}	-0.201	0.750	1.000	-0.833	0.030	0.602	-0.011
p_{poly}	0.191	-0.713	-0.833	1.000	-0.028	-0.573	0.010
p_1	-0.017	0.017	0.030	-0.028	1.000	-0.006	0.003
p_4	-0.137	0.503	0.602	-0.573	-0.006	1.000	0.229
p_6	0.003	-0.015	-0.011	0.010	0.003	0.229	1.000

L Tracker efficiency study

This appendix contains a detailed response to the question: Is signal efficiency affected by interference between muons in the tracker, possibly in a way that is not well-modeled by Monte Carlo?

L.1 Dominant efficiency systematic

The dominant efficiency systematic for nearby muons (inverse boost $1/\gamma \lesssim 0.3$) is from confusion of segments from different muons in the muon system. The uncertainty in this inefficiency is quantified in Fig. 5: there is a 2% difference between crossing and non-crossing muons for leading $p_T > 15 \text{ GeV}/c$, averaged uniformly in η , and 6% at the $|\eta| = 2.4$ extreme. (Definitions and supporting information are in Appendix A.) The cause of the inefficiency is due to incorrectly assigned segments: every muon track in the analysis is required to match at least two *unique* segments, and if muon A takes muon B 's segments while muon B does not match to muon A 's, then muon B would fail to be identified. Distances between extrapolated tracks

Table 16: R_4^1 BG template fit results (mu+track BG template).

p_{poly}	1654 ± 41
p_1	0.435 ± 0.055
p_2	1.00
p_3	0.00
p_4	0.00
p_5	0.00
p_6	0.029 ± 0.012
p_7	0.0282 ± 0.0093

Table 17: R_4^1 BG template fit correlation matrix (mu+track BG template).

	p_{poly}	p_1	p_6	p_7
p_{poly}	1.000	0.000	0.000	0.000
p_1	0.000	1.000	-0.197	0.060
p_6	0.000	-0.197	1.000	0.661
p_7	0.000	0.060	0.661	1.000

Table 18: R_4^1 invariant mass BG template fit results.

μ_{peak1}	2.30 ± 0.10
μ_{peak2}	4.31 ± 0.11
σ_{peak1}	0.701 ± 0.058
σ_{peak2}	0.707 ± 0.098
p_{gaus1}	443 ± 49
p_{gaus2}	411 ± 63
p_{poly}	372 ± 44
p_1	0.00
p_2	0.00
p_3	1.00
p_4	0.00
p_5	0.00 ± 0.54
p_6	0.063 ± 0.081
p_7	0.00
p_8	0.002 ± 0.022
p_9	0.00
p_{10}	0.00

and muon segments are typically 1–10 cm due to multiple scattering between the tracker and the muon system, so segments may even be confused for opening angles as large as 0.3 rad. The effect is larger in the endcap because large entrance angles in the magnetic field bending plane help to distinguish muons in the barrel.

Track-finding efficiencies are much higher than muon-identification efficiencies: $\sim 99.8\%$ for $p_T > 5 \text{ GeV}/c$, $|\eta| < 2.4$ tracks compared with $\sim 97\%$ for muons with the same kinematics. Since there are no road-broadening effects in the tracker that are comparable to the multiple scattering in the CMS magnet return yoke, tracks must be much closer together to suffer inefficiencies in the tracker alone. In this document, I will explicitly quantify this effect with Monte Carlo and information from [36–38].

Table 19: R_4^1 invariant mass BG template fit correlation matrix.

	μ_{peak1}	μ_{peak2}	σ_{peak1}	σ_{peak2}	p_{gaus1}	p_{gaus2}	p_{poly}	p_5	p_6	p_8
μ_{peak1}	1.000	0.831	0.808	-0.771	0.793	-0.780	0.235	-0.127	-0.059	0.041
μ_{peak2}	0.831	1.000	0.736	-0.751	0.788	-0.724	0.160	-0.096	-0.050	0.034
σ_{peak1}	0.808	0.736	1.000	-0.631	0.732	-0.672	0.149	-0.068	-0.024	0.017
σ_{peak2}	-0.771	-0.751	-0.631	1.000	-0.686	0.847	-0.448	0.255	0.124	-0.085
p_{gaus1}	0.793	0.788	0.732	-0.686	1.000	-0.636	0.008	0.064	0.066	-0.043
p_{gaus2}	-0.780	-0.724	-0.672	0.847	-0.636	1.000	-0.573	0.366	0.198	-0.134
p_{poly}	0.235	0.160	0.149	-0.448	0.008	-0.573	1.000	-0.592	-0.356	0.238
p_5	-0.127	-0.096	-0.068	0.255	0.064	0.366	-0.592	1.000	0.888	-0.615
p_6	-0.059	-0.050	-0.024	0.124	0.066	0.198	-0.356	0.888	1.000	-0.775
p_8	0.041	0.034	0.017	-0.085	-0.043	-0.134	0.238	-0.615	-0.775	1.000

Table 20: R_{22}^2 BG template fit results (trigger muon).

$\sigma_{J/\psi}$	0.02442 ± 0.00044
c_{exp}	-12.053
σ_ω	0.01
p_{exp}	334.67
p_ω	140 ± 16
p_ϕ	147 ± 18
$p_{J/\psi}$	3296 ± 60
$p_{\psi'}$	149 ± 14
p_{poly}	7905 ± 94
σ_ϕ	0.01
p_1	0.222 ± 0.018
p_2	0.443 ± 0.062
p_3	1.00
p_4	0.00
p_5	0.00
p_6	0.0079 ± 0.0073
p_7	0.0233 ± 0.0044
$\sigma_{\psi'}$	0.03

Table 21: R_{22}^2 BG template fit correlation matrix (trigger muon).

	$\sigma_{J/\psi}$	p_ω	p_ϕ	$p_{J/\psi}$	$p_{\psi'}$	p_{poly}	p_1	p_2	p_6	p_7
$\sigma_{J/\psi}$	1.000	-0.009	-0.009	0.120	0.011	-0.079	-0.003	-0.103	-0.006	0.030
p_ω	-0.009	1.000	0.029	-0.007	-0.004	-0.087	-0.027	0.110	0.026	-0.005
p_ϕ	-0.009	0.029	1.000	-0.007	-0.005	-0.104	0.035	0.145	0.027	-0.007
$p_{J/\psi}$	0.120	-0.007	-0.007	1.000	0.008	-0.062	-0.002	-0.080	-0.007	0.021
$p_{\psi'}$	0.011	-0.004	-0.005	0.008	1.000	-0.043	-0.007	-0.045	0.082	0.066
p_{poly}	-0.079	-0.087	-0.104	-0.062	-0.043	1.000	0.107	0.076	-0.005	-0.024
p_1	-0.003	-0.027	0.035	-0.002	-0.007	0.107	1.000	0.448	0.028	-0.028
p_2	-0.103	0.110	0.145	-0.080	-0.045	0.076	0.448	1.000	0.280	-0.036
p_6	-0.006	0.026	0.027	-0.007	0.082	-0.005	0.028	0.280	1.000	0.711
p_7	0.030	-0.005	-0.007	0.021	0.066	-0.024	-0.028	-0.036	0.711	1.000

I will also compare data and Monte Carlo distributions of the $\phi(1020)$ resonance, which allows us to test the simulation with $0.05 < \Delta R < 0.15$ opening angles.

L.2 CMS track reconstruction procedure

The CMS track reconstruction proceeds in five iterations, though the last three are designed for $p_T < 0.9$ GeV/ c and displaced tracks (low pixel efficiency). The first two iterations search for continuations of pairs and triplets of pixel clusters, and only if clusters can be unambiguously associated with a track (“highPurity”) are they removed from the list of clusters available in subsequent iterations. Tracks found in the same iteration can share up to 50% of their clusters. Clusters may be interpreted differently as hits on different tracks, due to track-dependent corrections, but inclusion of a cluster on one track does not automatically disqualify it from another.

L.3 Criteria for 50% overlap

To produce tracks that overlap through $\sim 50\%$ of the tracker, two oppositely signed muons would need to have very high momentum. To estimate this momentum, we use the following facts:

Table 22: R_{22}^2 BG template fit results (other muon).

$\sigma_{J/\psi}$	0.0325 ± 0.0058
σ_ω	0.01
p_ω	0.00 ± 0.84
p_ϕ	2.4 ± 2.6
$p_{J/\psi}$	36.1 ± 6.6
$p_{\psi'}$	2.1 ± 1.7
p_{poly}	195 ± 14
σ_ϕ	0.01
p_1	0.47 ± 0.16
p_2	0.94 ± 0.96
p_3	1.00
p_4	0.00
p_5	0.00
p_6	0.000 ± 0.063
p_7	0.012 ± 0.014
$\sigma_{\psi'}$	0.03

Table 23: R_{22}^2 BG template fit correlation matrix (other muon).

	$\sigma_{J/\psi}$	p_ω	p_ϕ	$p_{J/\psi}$	$p_{\psi'}$	p_{poly}	p_1	p_2	p_6	p_7
$\sigma_{J/\psi}$	1.000	0.000	-0.018	0.208	0.022	-0.095	0.101	0.172	0.000	0.059
p_ω	0.000	1.000	-0.000	0.000	0.000	0.000	0.000	0.000	0.000	0.000
p_ϕ	-0.018	-0.000	1.000	-0.015	-0.012	-0.121	-0.041	-0.161	-0.000	-0.039
$p_{J/\psi}$	0.208	0.000	-0.015	1.000	0.019	-0.082	0.088	0.149	0.000	0.051
$p_{\psi'}$	0.022	0.000	-0.012	0.019	1.000	-0.040	0.047	0.097	-0.000	0.019
p_{poly}	-0.095	0.000	-0.121	-0.082	-0.040	1.000	-0.038	-0.049	0.000	-0.018
p_1	0.101	0.000	-0.041	0.088	0.047	-0.038	1.000	0.181	0.000	0.119
p_2	0.172	0.000	-0.161	0.149	0.097	-0.049	0.181	1.000	0.000	0.298
p_6	0.000	0.000	-0.000	0.000	-0.000	0.000	0.000	0.000	1.000	-0.001
p_7	0.059	0.000	-0.039	0.051	0.019	-0.018	0.119	0.298	-0.001	1.000

- pixel channels are 100–150 μm wide (assume 100),
- TOB strips are about three times as wide (assume 300),
- clusters are 1.5–2 channels wide for high- p_T tracks.

The first two facts come from a conversation with Kevin Burkett, the last comes from Fig. 8 and 11 of [36, 37], reproduced in Fig. 35. Cluster size depends primarily on path length through the silicon, with a near-minimum for high- p_T tracks (near-minimal because of the magnetic field).

Figures 36 and 37 quantify the degree of separation at two distances from the beamline: 5 cm (first pixel layer) and 60 cm (first TOB layer, about 50% through the tracker). Two trajectories were propagated from the origin to 5 and 60 cm cylinders using the appropriate CMSSW propagator for a variety of $\Delta\phi$ opening angles at the origin and initial p_T of both trajectories (both momenta were equal, with $\eta = 0$). For a ~ 5 channel width separation at both radii, both muons would need $p_T > 60 \text{ GeV}/c$, for ~ 2 channel widths, both muons would need $p_T > 150 \text{ GeV}/c$, and for ~ 1 channel width, both muons would need $p_T > 300 \text{ GeV}/c$.

L.4 Observing track interference in pair-gun MC

To search for the onset of an inefficiency due to nearby tracks in the tracker, I plotted efficiency versus ΔR using our pair-gun MC. The pair-gun MC is a full CMSSW simulation of

Table 24: The Monte Carlo dataset for low mass Drell-Yan process is the following and on the ‘cms_dbs_ph_analysis_01’ DBS instance:

Dataset
/DrellYanPythia8-PU-CMSSW_3_8_7_GEN-SIM-RECO_v1
/aysen-DrellYanPythia8-PU-CMSSW_3_8_7_GEN-SIM-RECO_v2 -62767116feb65c0b8369dd073c0e13d0/USER

Table 25: List of Monte Carlo datasets for NMSSM model with various masses m_h and m_a given in first two columns (in GeV/c^2). All listed datasets are on the ‘cms_dbs_ph_analysis_01’ DBS instance.

m_h	m_a	Dataset
85	2	/NMSSM_h085_a2.0-PU-CMSSW_3_8_7_GEN-SIM-RECO_v1 /aysen-NMSSM_h085_a2.0-PU-CMSSW_3_8_7_GEN-SIM-RECO_v2 -62767116feb65c0b8369dd073c0e13d0/USER
100	0.3	/NMSSM_h100_a0.3-PU-CMSSW_3_8_7_GEN-SIM-RECO_v1 /aysen-NMSSM_h100_a0.3-PU-CMSSW_3_8_7_GEN-SIM-RECO_v2 -62767116feb65c0b8369dd073c0e13d0/USER
100	0.5	/NMSSM_h100_a0.5-PU-CMSSW_3_8_7_GEN-SIM-RECO_v1 /aysen-NMSSM_h100_a0.5-PU-CMSSW_3_8_7_GEN-SIM-RECO_v2 -62767116feb65c0b8369dd073c0e13d0/USER
100	1	/NMSSM_h100_a1.0-PU-CMSSW_3_8_7_GEN-SIM-RECO_v1 /aysen-NMSSM_h100_a1.0-PU-CMSSW_3_8_7_GEN-SIM-RECO_v2 -62767116feb65c0b8369dd073c0e13d0/USER
100	2	/NMSSM_h100_a2.0-PU-CMSSW_3_8_7_GEN-SIM-RECO_v1 /aysen-NMSSM_h100_a2.0-PU-CMSSW_3_8_7_GEN-SIM-RECO_v2 -62767116feb65c0b8369dd073c0e13d0/USER
100	4	/NMSSM_h100_a4.0-PU-CMSSW_3_8_7_GEN-SIM-RECO_v1 /aysen-NMSSM_h100_a4.0-PU-CMSSW_3_8_7_GEN-SIM-RECO_v2 -62767116feb65c0b8369dd073c0e13d0/USER
120	2	/NMSSM_h120_a2.0-PU-CMSSW_3_8_7_GEN-SIM-RECO_v1 /aysen-NMSSM_h120_a2.0-PU-CMSSW_3_8_7_GEN-SIM-RECO_v2 -62767116feb65c0b8369dd073c0e13d0/USER

Table 26: List of Monte Carlo datasets for SUSY with Extra- $\mathcal{U}(1)_{\text{dark}}$ model with various masses $m_{\tilde{g}}$ and $m_{\gamma_{\text{dark}}}$ given in first two columns (in GeV/c^2). All listed datasets are on the ‘cms_dbs_ph_analysis_01’ DBS instance.

$m_{\tilde{g}}$	$m_{\gamma_{\text{dark}}}$	Dataset
500	0.5	/ExtraU1_0500_0.5-PU-CMSSW_3_8_7_GEN-SIM-Raw_v2 /aysen-ExtraU1_0500_0.5-PU-CMSSW_3_8_7_GEN-SIM-RECO_v2 -62767116feb65c0b8369dd073c0e13d0/USER
500	1	/ExtraU1_0500_1.0-PU-CMSSW_3_8_7_GEN-SIM-Raw_v2 /aysen-ExtraU1_0500_1.0-PU-CMSSW_3_8_7_GEN-SIM-RECO_v2 -62767116feb65c0b8369dd073c0e13d0/USER
600	0.5	/ExtraU1_0600_0.5-PU-CMSSW_3_8_7_GEN-SIM-Raw_v2 /aysen-ExtraU1_0600_0.5-PU-CMSSW_3_8_7_GEN-SIM-RECO_v2 -62767116feb65c0b8369dd073c0e13d0/USER
600	1	/ExtraU1_0600_1.0-PU-CMSSW_3_8_7_GEN-SIM-Raw_v2 /aysen-ExtraU1_0600_1.0-PU-CMSSW_3_8_7_GEN-SIM-RECO_v2 -62767116feb65c0b8369dd073c0e13d0/USER
800	0.5	/ExtraU1_0800_0.5-PU-CMSSW_3_8_7_GEN-SIM-Raw_v2 /aysen-ExtraU1_0800_0.5-PU-CMSSW_3_8_7_GEN-SIM-RECO_v2 -62767116feb65c0b8369dd073c0e13d0/USER
800	1	/ExtraU1_0800_1.0-PU-CMSSW_3_8_7_GEN-SIM-Raw_v2 /aysen-ExtraU1_0800_1.0-PU-CMSSW_3_8_7_GEN-SIM-RECO_v2 -62767116feb65c0b8369dd073c0e13d0/USER
1000	0.5	/ExtraU1_1000_0.5-PU-CMSSW_3_8_7_GEN-SIM-Raw_v2 /aysen-ExtraU1_1000_0.5-PU-CMSSW_3_8_7_GEN-SIM-RECO_v2 -62767116feb65c0b8369dd073c0e13d0/USER
1000	1	/ExtraU1_1000_1.0-PU-CMSSW_3_8_7_GEN-SIM-Raw_v2 /aysen-ExtraU1_1000_1.0-PU-CMSSW_3_8_7_GEN-SIM-RECO_v2 -62767116feb65c0b8369dd073c0e13d0/USER
1200	0.5	/ExtraU1_1200_0.5-PU-CMSSW_3_8_7_GEN-SIM-Raw_v2 /aysen-ExtraU1_1200_0.5-PU-CMSSW_3_8_7_GEN-SIM-RECO_v2 -62767116feb65c0b8369dd073c0e13d0/USER
1200	1	/ExtraU1_1200_1.0-PU-CMSSW_3_8_7_GEN-SIM-Raw_v2 /aysen-ExtraU1_1200_1.0-PU-CMSSW_3_8_7_GEN-SIM-RECO_v2 -62767116feb65c0b8369dd073c0e13d0/USER

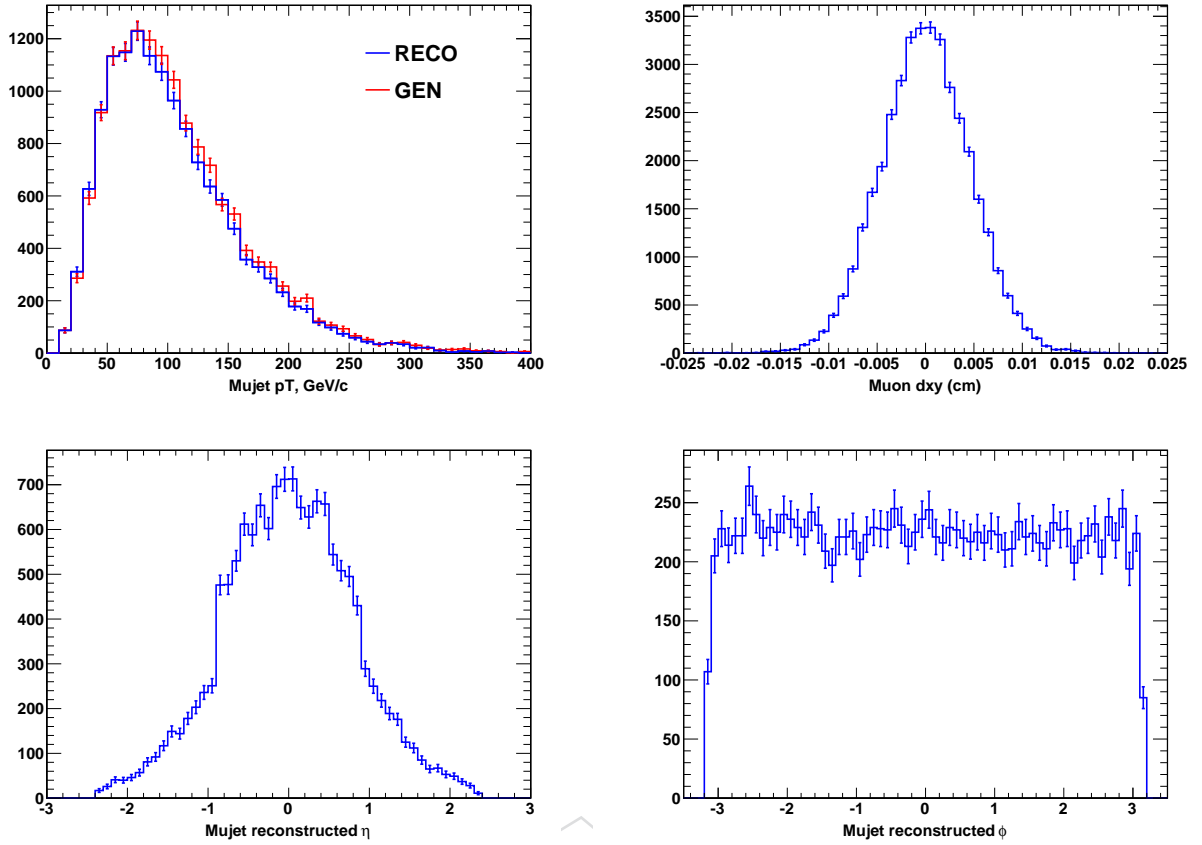


Figure 34: Basic validation plots of 7 TeV Monte Carlo sample for SUSY with Extra- $\mathcal{U}(1)$ _{dark} model made with the satisfied requirement of a minimal acceptance.

1270 two opposite-sign muons with uniformly random pair momentum ($0 < p_T^{\mu\mu} < 100 \text{ GeV}/c$),
 1271 mass ($2m_\mu < m < 6 \text{ GeV}/c^2$), pseudorapidity ($-2.5 < \eta^{\mu\mu} < 2.5$), and azimuthal angle
 1272 ($-\pi < \phi^{\mu\mu} < \pi$). Each pair of muons is reconstructed three times: once with the μ^+ as the
 1273 only particle in the event, once with the μ^- as the only particle in the event, and once with
 1274 both μ^+ and μ^- in the same event. This allows us to study efficiency losses due to interference
 1275 separately from single-particle efficiency.

With these tools, we can define “interference efficiency” in the following way:

$$P(\mu^+ \mu^- | \mu^+ \text{ and } \mu^-) = \frac{\text{both muons reconstructed in the same event and separately}}{\text{both muons reconstructed separately}} \quad (18)$$

1276 with additional generator-level requirements of $p_T > 5 \text{ GeV}/c$ and $|\eta| < 2.4$ for both numerator
 1277 and denominator. “Reconstructed” means that the reconstructed track exists with ≥ 8 hits
 1278 and $\chi^2/N_{\text{dof}} < 4$, though these quality cuts have negligible impact on the final result. The
 1279 probability of reconstructing both muons separately, given kinematical acceptance, is 99.6%.

1280 Figure 38 presents this interference efficiency as a function of ΔR , where an 8% dip is visible
 1281 for $\Delta R < 0.01$. This dip is correlated with high momentum (same figure), suggesting that it
 1282 is related to track overlap. For context, we show the mass distribution of muon pairs with
 1283 $\Delta R < 0.01$ in this sample in Fig. 39. The $100 \text{ GeV}/c$ upper limit in momentum implies only
 1284 mass $< 0.5 \text{ GeV}/c^2$ pairs have such a small opening angle. For a $1 \text{ GeV}/c^2$ boson, the onset of
 1285 the effect would be at higher momenta.

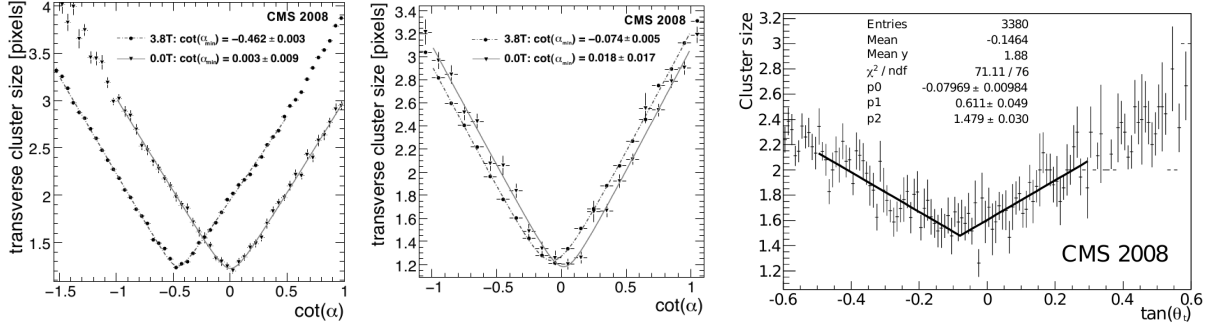


Figure 35: Cluster size versus entrance angle in the pixel barrel (left), pixel endcap (middle), with and without magnetic field, and TOB layer 4 (right). High- p_T tracks have minimal entrance angle. Reproduced from [36, 37].

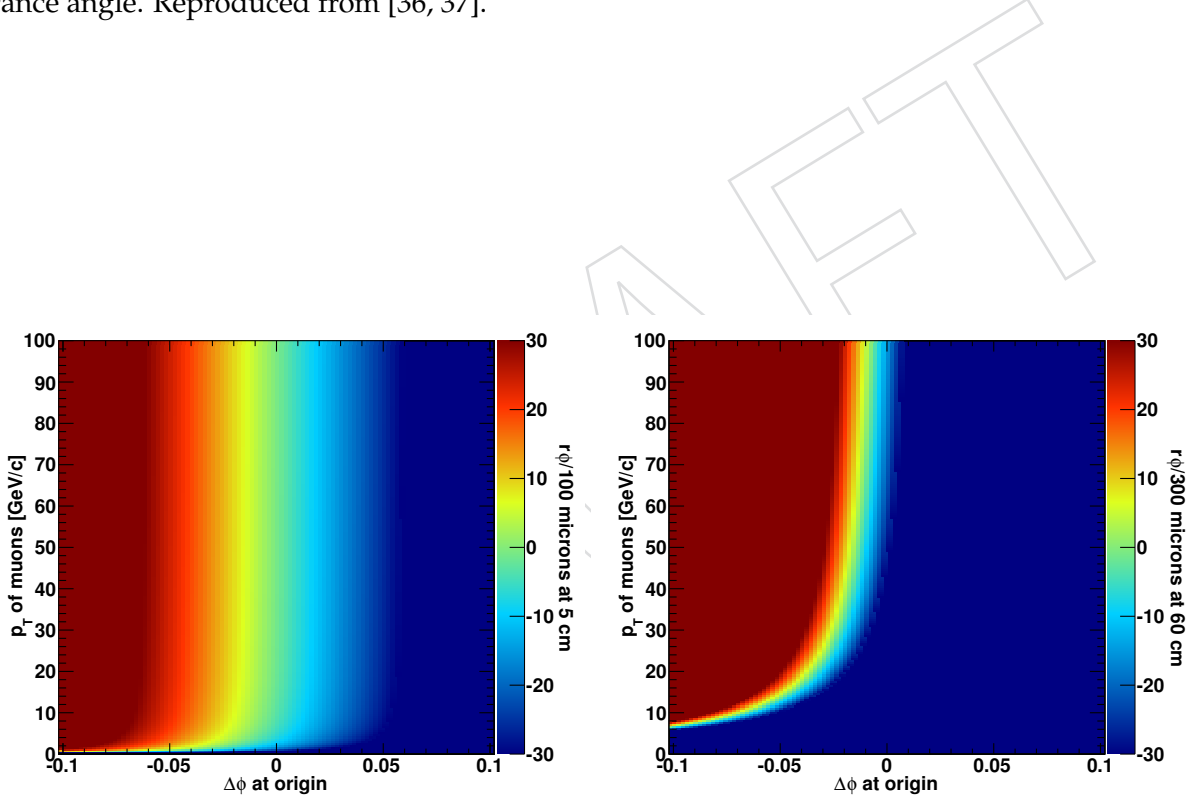


Figure 36: Separation of two muon trajectories at the first pixel layer, 5 cm from the beamline (left), and the first TOB layer, 60 cm from the beamline (right). The color scale is the $r\phi$ distance between the muon trajectories on a cylinder of the given radius, measured in units of channel widths, taking 100 μm for the pixel and 300 μm for the TOB. Green is zero separation; red and blue are 30 channels apart. The $r\phi$ separation asymptotically approaches a constant multiple of $\Delta\phi$ at the origin for high- p_T muons (both muons have the same p_T in this simulation).

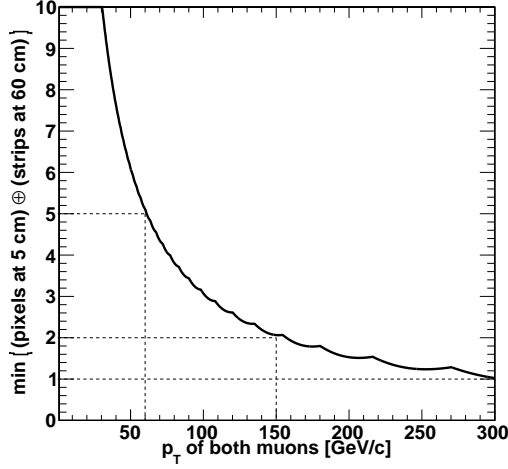


Figure 37: Minimum separation in *both* the pixel detector at a radius of 5 cm *and* the TOB at a radius of 60 cm. The vertical axis is the minimum $r\phi$ separation in pixel channel widths, added in quadrature with the minimum $r\phi$ separation in TOB channel widths, minimized over possible values of $\Delta\phi$ at the origin. For two muons to be separated by ~ 1 channel width in the pixel *and* TOB, both muons would need about $p_T \approx 300$ GeV/ c .

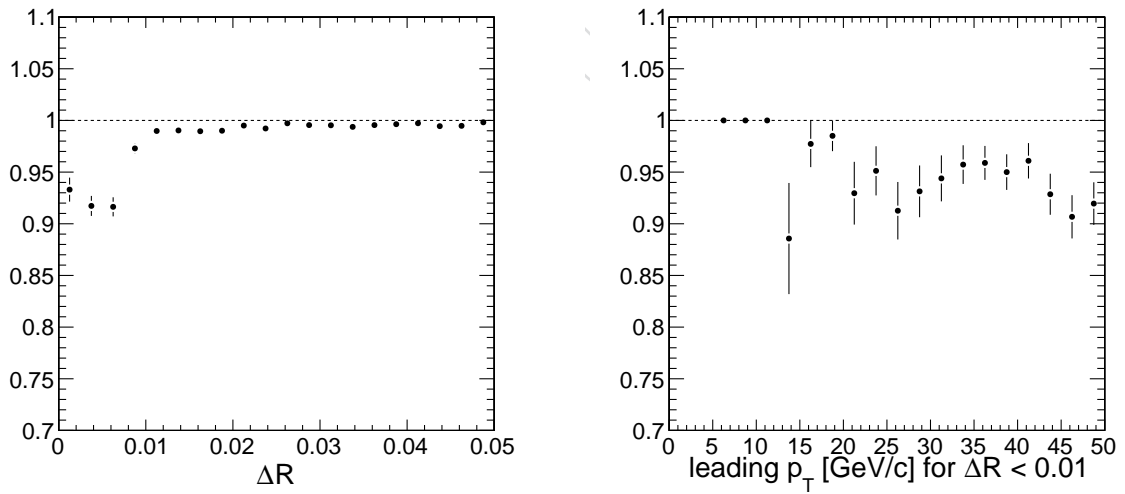


Figure 38: Left: $P(\mu^+\mu^-|\mu^+ \text{ and } \mu^-)$ for track cuts (see text) versus ΔR . Right: the same quantity versus leading muon p_T for $\Delta R < 0.01$, showing that the effect prefers high momenta.

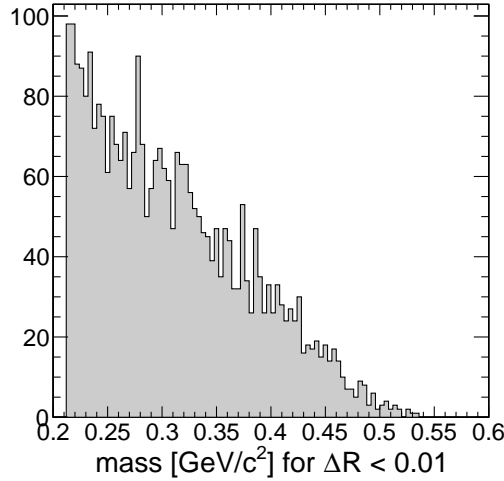


Figure 39: Values of muon pair mass consistent with $\Delta R < 0.01$ in this simulation, for context.

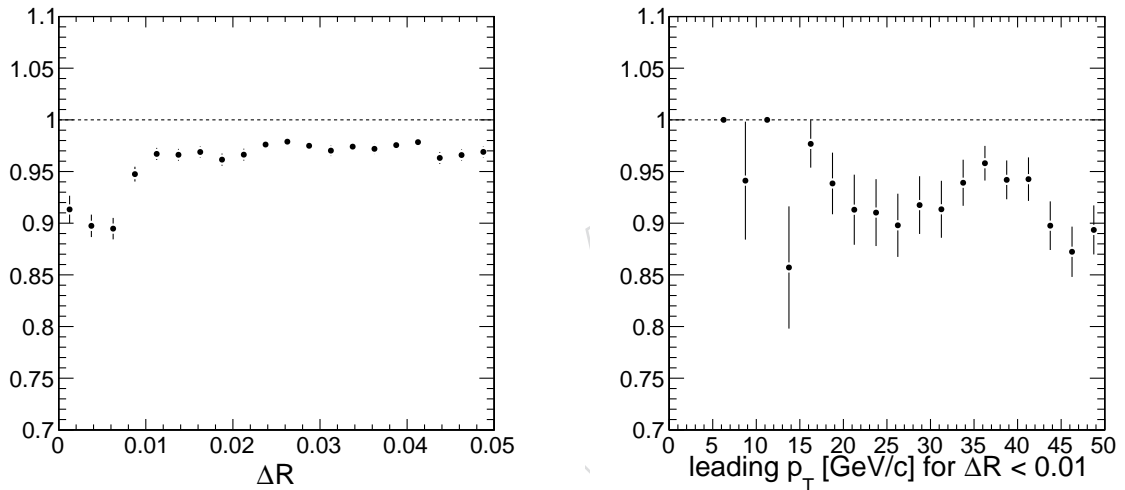
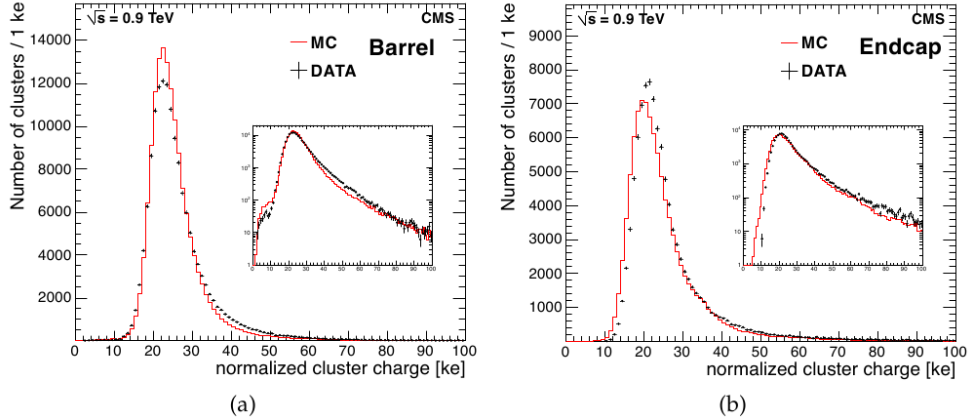


Figure 40: Left: $P(\mu^+ \mu^- | \mu^+ \text{ and } \mu^-)$ for muon cuts versus ΔR . Right: the same quantity versus leading muon p_T for $\Delta R < 0.01$, showing that the effect prefers high momenta.

1286 The same study can be performed for the full muon cuts, that is, adding the requirement that
 1287 the track is reconstructed as a TrackerMuon with ≥ 2 arbitrated muon segments. This is pre-
 1288 sented in Fig. 40. The interference efficiency for the full muon cuts has the same shape as a
 1289 function of ΔR , though a lower plateau for $\Delta R \gg 0.01$. This is the effect of the muons cross-
 1290 ing the muon system (discussed in the analysis note), which is not a strict function of ΔR at the
 1291 origin.

1292 L.5 Data/MC comparisons for tracking

1293 Reference [38] presents a detailed overview of the status of the tracking simulation with early
 1294 collisions. The simulation is shown to reproduce the shapes of signal responses (see Fig. 41,
 1295 copied from the paper) and many high-level tracking quantities. Figure 42 shows the number
 1296 of hits and χ^2/N_{dof} distributions from this paper, which are relevant to our analysis as track
 1297 quality cuts. The distributions in the early LHC paper represent low- p_T hadrons, rather than
 1298 $p_T > 5 \text{ GeV}/c$ muons, though.



~~Figure 4~~: The normalized cluster charge measured in the (a) barrel and (b) endcap pixel detectors for the sample of 0.9 TeV minimum bias events. The insets show the same distributions on semi-log scales.

Figure 41: Figure reproduced from [38].

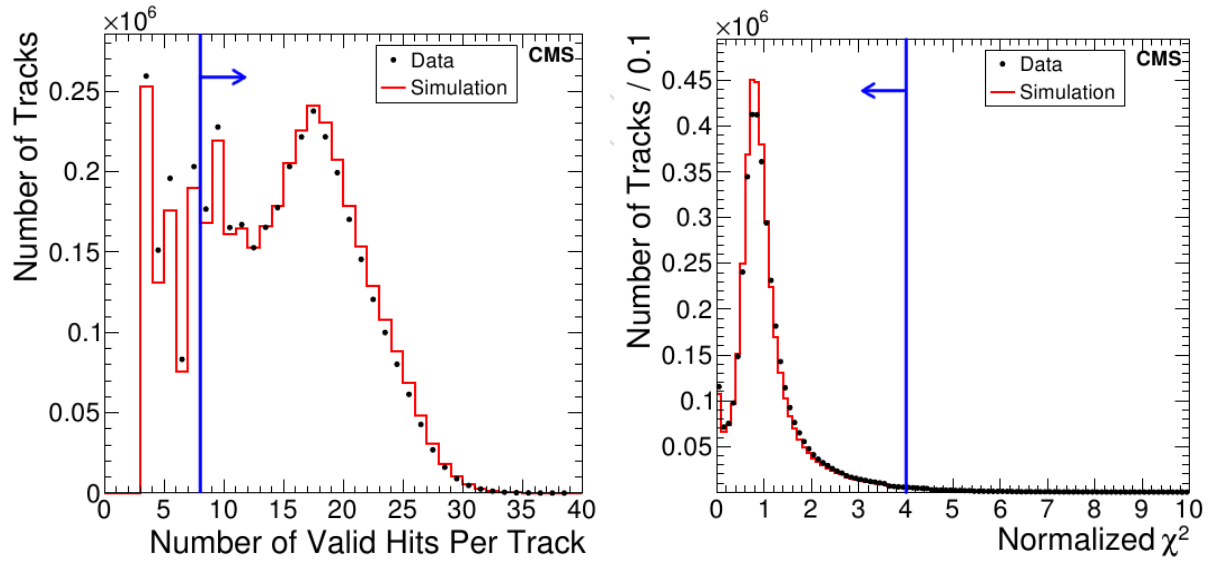


Figure 42: Two figures from the early LHC tracking paper relevant to our analysis: blue lines indicate our cuts. These distributions have different shapes for our $p_T > 5 \text{ GeV}/c$ tracks.

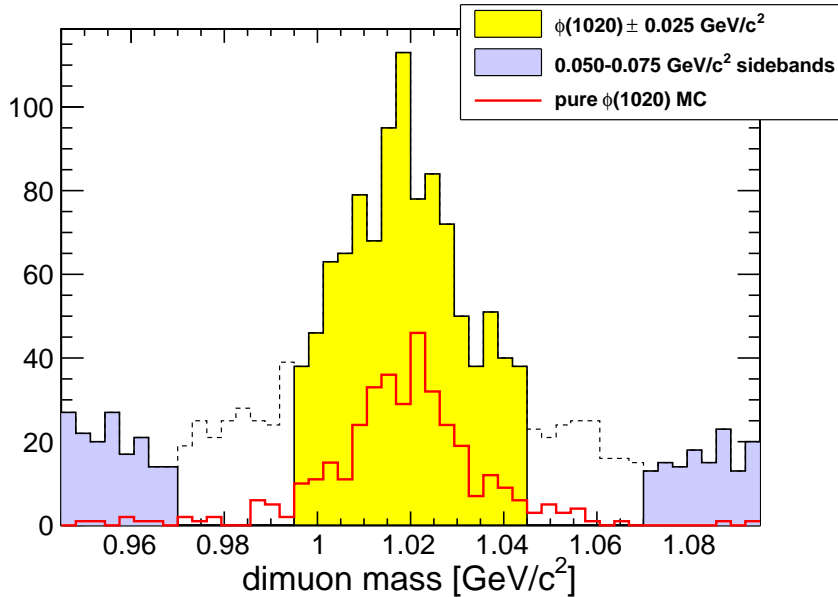


Figure 43: Basic distribution of the $\phi(1020)$ study: dimuon invariant mass distribution of data (dashed line, colored in sections) with the signal region indicated by yellow, the sidebands indicated by blue, overlaid with a pure $\phi(1020)$ MC simulation (unscaled).

1299 One may argue that the tracking simulation may be trusted if it reproduces all low-level sig-
 1300 nals and has a realistic alignment, since our analysis signal only differs in geometry, and all
 1301 geometry and algorithms are the same for data and Monte Carlo. This can be partially tested
 1302 with studies of the $\phi(1020)$ resonance.

1303 L.6 Study of the $\phi(1020)$ resonance

1304 The $\phi(1020)$ resonance provides a standard candle of low-mass, moderately high-momentum
 1305 dimuons with which to test the level of data/MC agreement. It corresponds to a moderately
 1306 low range of opening angles $0.05 < \Delta R < 0.15$, though not low enough to sample the $\Delta R <$
 1307 0.01 tracker inefficiency. It is the lowest-mass Standard Model narrow resonance found in both
 1308 data and Monte Carlo ($\omega(782) \rightarrow \mu\mu$ is missing from the Pythia 6 decay tables), and it is in
 1309 the middle of the target mass range of our analysis, though lower than our target momentum
 1310 range.

1311 Figure 43 presents the invariant mass distribution near the $\phi(1020)$ peak, indicating the signal
 1312 region ($|m - m_\phi| < 0.025 \text{ GeV}/c^2$), the sidebands ($0.050 < |m - m_\phi| < 0.075 \text{ GeV}/c^2$), and a
 1313 pure $\phi(1020)$ Monte Carlo simulation. The $\phi(1020)$ simulation is a subset of InclusiveMu5_Pt30
 1314 (muons from Pythia 6 QCD): dimuons selected at generator level to have $\phi(1020)$ as their par-
 1315 ent.

1316 The $\phi(1020)$ events in Monte Carlo are all prompt and in jets, while the data has a displaced
 1317 component and an isolated component. For a more appropriate comparison, I applied the
 1318 following cuts:

- 1319 • distance between the dimuon vertex and the closest primary vertex in z must be less
 1320 than 1 mm ($L_{xy} < 1 \text{ mm}$);
- 1321 • the sum of track p_T for $p_T > 1.5 \text{ GeV}/c$ in a $\Delta R < 0.4$ cone around the dimuon axis
 1322 must be greater than $3 \text{ GeV}/c$ ($Iso > 3 \text{ GeV}/c$);

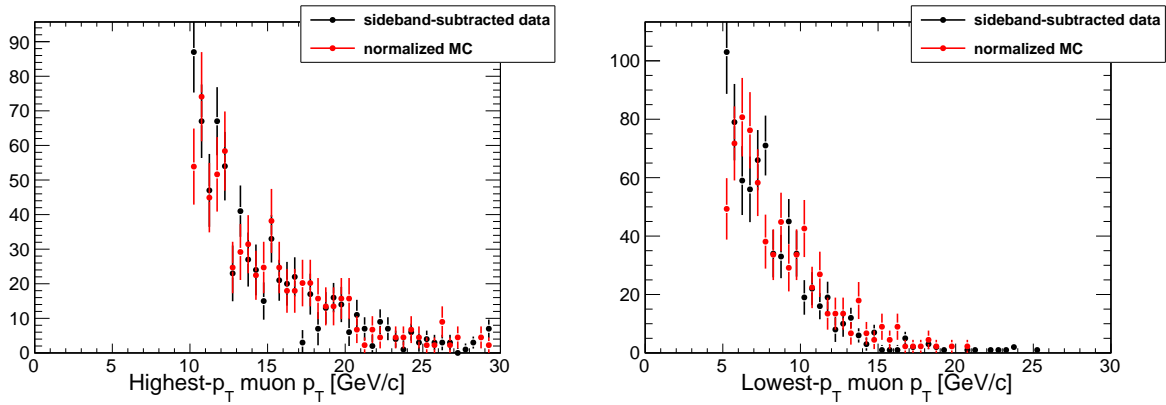


Figure 44: Sideband-subtracted muon momentum distributions overlaid by Monte Carlo (normalized to equal number of events).

- exactly two reconstructed muons per event;
- apply $|m - m_\phi| < 0.025 \text{ GeV}/c^2$ to Monte Carlo as well as the signal;
- at least one muon must have $p_T > 10 \text{ GeV}/c$.

The data were collected using any single or double-muon trigger that was available. Prescales changed during the run, but HLT_Mu9 and HLT_Mu11 were prescaled late in the year—the requirement of $p_T > 10 \text{ GeV}/c$ is a compromise between strict correctness (our analysis uses only $p_T > 15 \text{ GeV}/c$) and the need to maximize the size of the dataset for statistically meaningful comparisons. Figure 44 shows sideband-subtracted $\phi(1020)$ data overlaid by normalized Monte Carlo of the highest and lowest- p_T muon in each event. The data and Monte Carlo p_T spectra are consistent: there is no evidence of trigger prescale thresholds in the spectrum. Figure 45 presents the ΔR , η , I_{so} , and L_{xy} distributions (with all cuts applied).

Figure 46 shows the same sideband-subtracted data overlaid by normalized Monte Carlo for the distributions used to define muon quality cuts: number of tracker hits, tracker χ^2/N_{dof} , and number of arbitrated muon segments. All cuts are far from the distributions except the number of segments. The number of segments matched to a TrackerMuon track depends on the level of agreement between tracks propagated from the tracker and muon segment positions and entrance angles, which are shown in Fig. 47.

The Monte Carlo sample used in this study and all signal samples used in the main analysis were produced using ideal alignment and calibration conditions. The data in this $\phi(1020)$ study is a combination of Sep17ReReco (2010A) and PromptReco (2010B), unlike the main analysis, which uses Dec22ReReco. The only observed discrepancy between data and Monte Carlo is in the χ^2/N_{dof} distribution (Fig. 46 top-right), in which the Monte Carlo peaks at one but the data peaks lower than one. This could be because the tracker alignment uses artificially inflated Alignment Position Errors (APEs) in PromptReco for safety. The muon residuals distributions (Fig. 47) are completely insensitive to muon alignment conditions for $\sim 20 \text{ GeV}/c$ muon momenta because of the dominance of multiple scattering in the propagation.

L.7 Tracker efficiency conclusions

Muon segment assignment for muons whose trajectories cross in the muon system is the dominant efficiency systematic for a wide range of opening angles. However, efficiency losses in the tracker could play a significant role for $150\text{--}300 \text{ GeV}/c$ muons. An 8% loss in efficiency is observed in pair-gun MC for $\Delta R < 0.01$ muon pairs, though such a high boost is a special case in

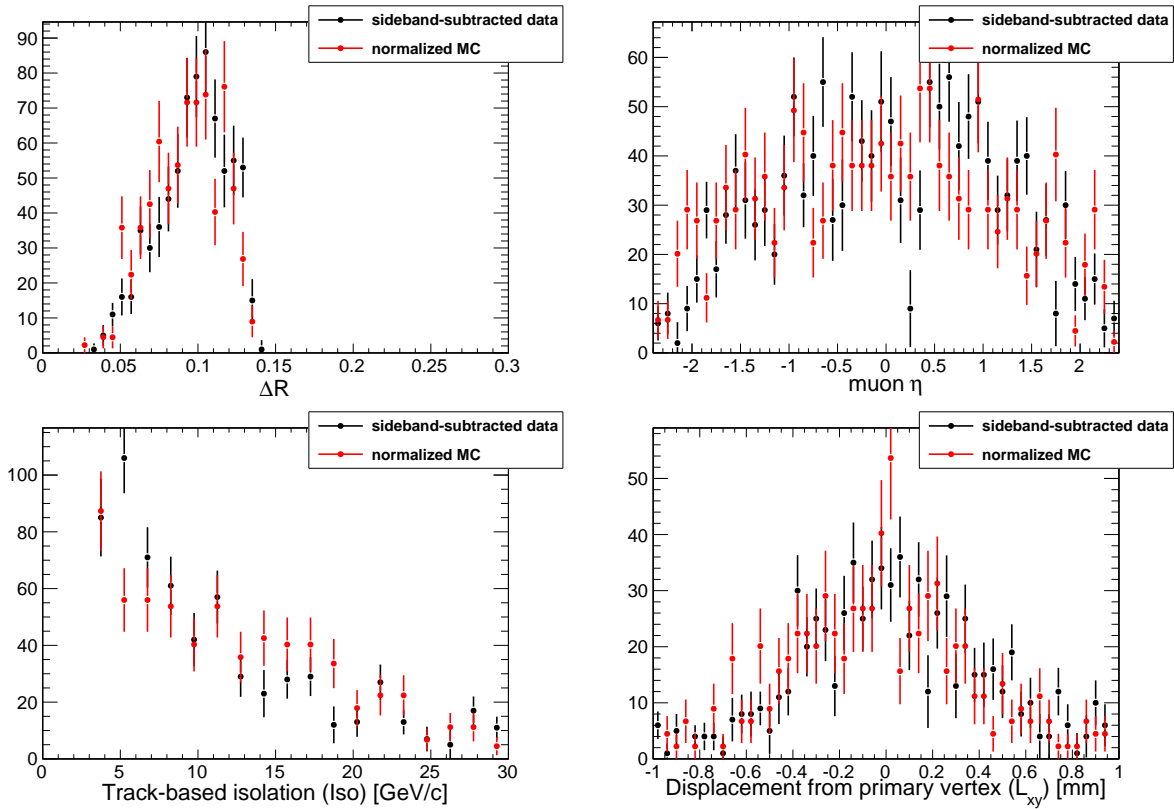


Figure 45: Other distributions relevant for or used to define the $\phi(1020)$ sample.

1354 our analysis. The simulation was tested for moderately low opening angles ($0.05 < \Delta R < 0.15$)
 1355 using the $\phi(1020)$ resonance, though the region where the tracker begins to be inefficient for
 1356 nearby muons is orthogonal to this or any test using Standard Model resonances.

1357 M MuscleFit study

1358 In order to estimate the effect of the new "twist-free" tracker alignment, we re-run the full
 1359 reconstruction for the events in our signal and signal control regions only.

1360 The December 22 re-reco datasets /Mu/Run2010A-Dec22ReReco_v1/RECO, /Mu/Run2010B-
 1361 Dec22ReReco_v1/RECO were officially produced with the "end-of-year" conditions set marked
 1362 with the FT_R_39X_V4A global tag. We verified that when we run our own reconstructions with
 1363 the same conditions, we get exactly the same results. This step assured the correctness of our
 1364 re-reconstruction procedure.

1365 To re-run reconstruction with the new "twist-free" tracker alignment and the updated global
 1366 position record, we changed the configuration to use the new constants stored in sqlite DB files.
 1367 The "twist-free" tracker alignment sqlite file was picked up at /afs/cern.ch/cms/CAF/
 1368 CMSALCA/ALCA_TRACKERALIGN/PayLoads/TwistFree/mp0529FULL_TobCentered.db.
 1369 The new GPR was created using the /afs/cern.ch/user/s/spiridon/public/gpr/
 1370 GlobalPositionRcd_FEB21_2011_1stTwistFreeGPR_liter-write_cfg.py configuration.
 1371

1372 We also tried applying the MuScleFit corrections to the same events. This is the corrections
 1373 formula that we used: $p_T^{\text{corr}} = (1.02013 - 0.000507004 p_T + Q0.0125399\eta - Q0.0048137\sin(\phi + 2.28505))p_T$. It is the current latest parametrization obtained according to the MuScleFit twiki
 1374

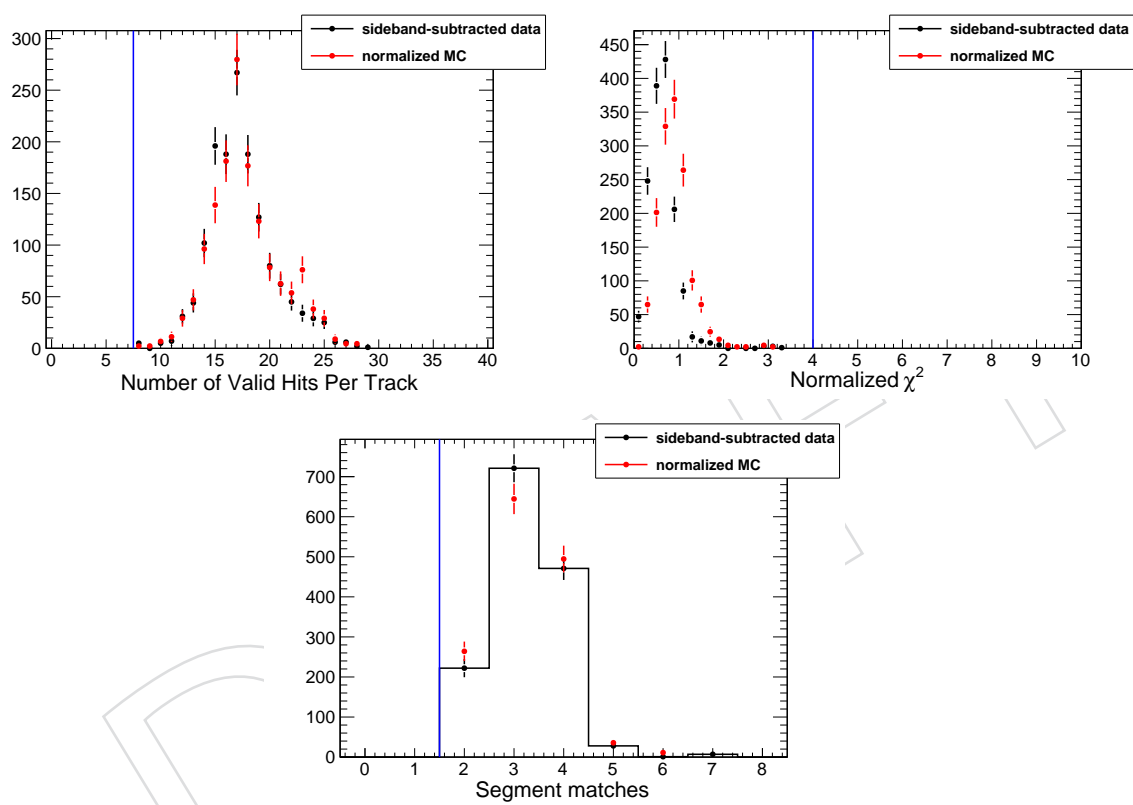


Figure 46: Distributions of track quality cuts (top row) and muon quality cuts (bottom) with cut thresholds indicated in blue. All cuts have been applied in all distributions.

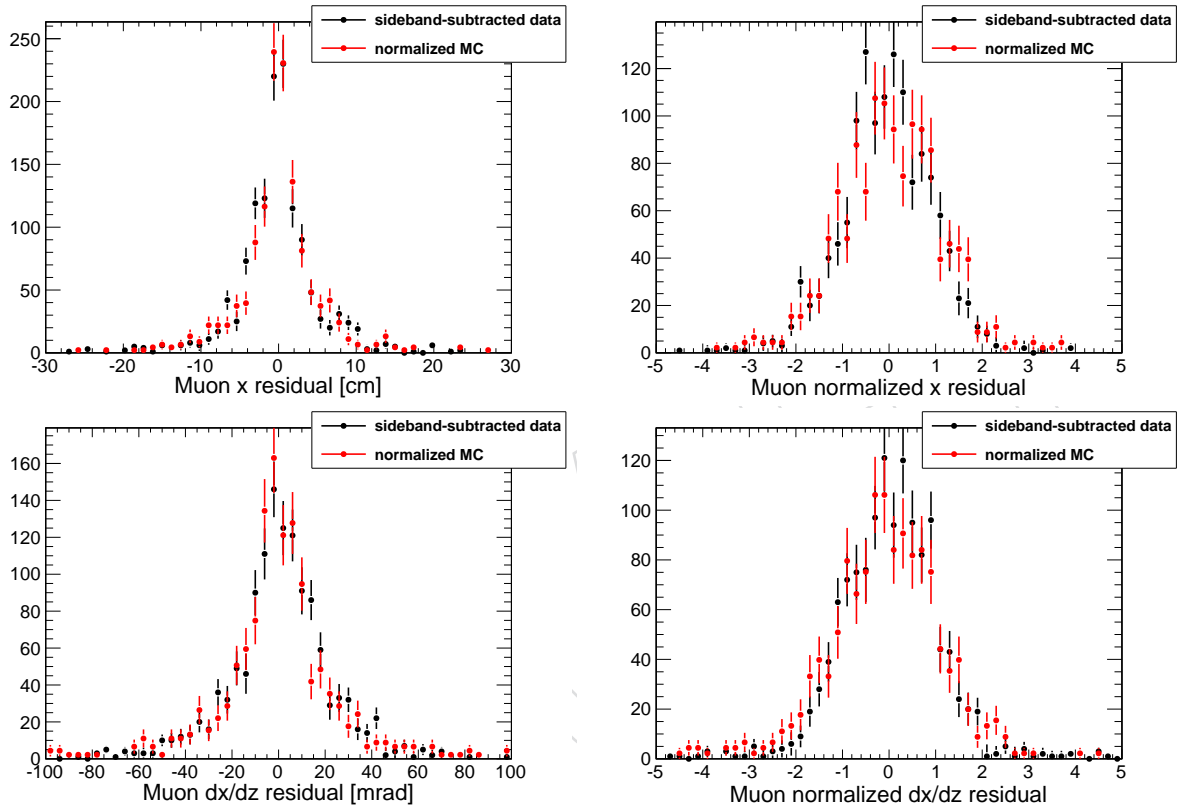


Figure 47: Distance between propagated track and muon segment in the magnetic field bending plane (x , top-left), the same normalized by uncertainty (top-right), the difference in entrance angle (dx/dz , bottom-left), and the same normalized by uncertainty (bottom-right). These are relevant for determining the number of muon segments matched to a TrackerMuon.

1375 instructions.

1376 Table 27 summarizes di-muon masses for the events in control signal regions of a-2 and b-1.
 1377 The di-muon resonance mass difference due to the change in tracker alignment is quite small,
 1378 usually less than 0.08 GeV. The MuScleFit corrections, on the other hand, give corrections with
 1379 variation of at least an order of magnitude larger. If we look at the similar number in the
 1380 region a-1 (not shown in the table) which has much larger number of events, the differences
 1381 in resonance mass due to the new tracker alignment are in the range of $[-0.11, 0.07]$, while
 1382 the differences due to MuScleFit corrections are as large as $[-1.19, 2.42]$. The effect of these
 1383 corrections are plotted in Fig. 48.

1384 Three events escape region a-1 with the "twist-free" tracker alignment: either due to p_T becoming
 1385 lower than 80 GeV/c or mu-jet not being reconstructed. However, we can't say if any other
 1386 new events enter our signal regions, as we have re-reconstructed only the limited set of events.

Table 27: Di-muon masses in regions a-2 and b-1 with the official December 22 re-reconstructed samples ($m(Dec22)$), the same events re-reconstructed with the new "twist-free" tracker geometry ($m(new)$), and with MuScleFit corrections applied ($m_{cor}(Dec22)$).

run evt lumi	mujet	$m(Dec22)$	$m(new)$	$m_{cor}(Dec22)$	$m(new) - m(Dec22)$	$m_{cor}(Dec22) - m(Dec22)$
(a-2)						
147754 142156381 115	1	0.8393	0.8381	0.5134	-0.0012	-0.3259
147754 142156381 115	2	1.0168	1.0158	1.1652	-0.0010	+0.1484
(b-1)						
147390 466023987 565	1	2.2415	2.2430	2.1463	+0.0015	-0.0952
147390 466023987 565	2	1.7018	1.7031	1.7033	+0.0013	+0.0015
148031 75834999 88	1	2.7795	2.7715	2.7881	-0.0080	+0.0086
148031 75834999 88	2	3.2009	3.1981	2.9649	-0.0028	-0.2360
148031 87893413 101	1	1.2463	1.2468	1.2553	+0.0005	+0.0091
148031 87893413 101	2	2.2720	2.2732	2.2607	+0.0012	-0.0113
148862 769926732 527	1	3.1413	3.1402	3.1774	-0.0010	+0.0362
148862 769926732 527	2	1.9327	1.9287	2.2289	-0.0039	+0.2962
149011 109260652 69	1	1.1908	1.1935	1.2374	+0.0028	+0.0466
149011 109260652 69	2	1.4572	1.4564	1.5472	-0.0008	+0.0900
149011 926316381 668	1	2.3061	2.3108	2.6775	+0.0047	+0.3714
149011 926316381 668	2	3.8348	3.8337	3.7852	-0.0010	-0.0495
149181 1009000653 1024	1	3.2128	3.2179	3.2589	+0.0051	+0.0461
149181 1009000653 1024	2	1.8336	1.8294	1.7334	-0.0041	-0.1002
149181 1604150756 1679	1	1.5460	1.5457	1.5195	-0.0003	-0.0265
149181 1604150756 1679	2	2.6663	2.6676	2.4888	+0.0013	-0.1775
149181 499095296 563	1	1.7449	1.7461	1.9299	+0.0011	+0.1849
149181 499095296 563	2	0.7217	0.7219	0.7296	+0.0002	+0.0079

1387 N High-boost dimuon efficiency study

1388 To study muon efficiency for extremely boosted dimuons, we generated a pair-gun MC sample
 1389 much like the one described in Appendix A, except with dimuon mass $< 0.6 \text{ GeV}/c^2$ (uniformly)
 1390 and pair p_T up to 500 GeV/c (uniformly). This allows us to more deeply investigate
 1391 the tracker inefficiency glimpsed in Fig. 38 (Appendix L.4).

1392 The muon efficiency is the probability that a muon is observed, given that it exists, which
 1393 requires some definition of "observed" in terms of a match between generator-level and re-
 1394 constructed objects. Extremely boosted dimuons can be fully reconstructed yet fail standard
 1395 muon-matching cuts if muon A is matched to muon B and vice-versa. Such cases should not

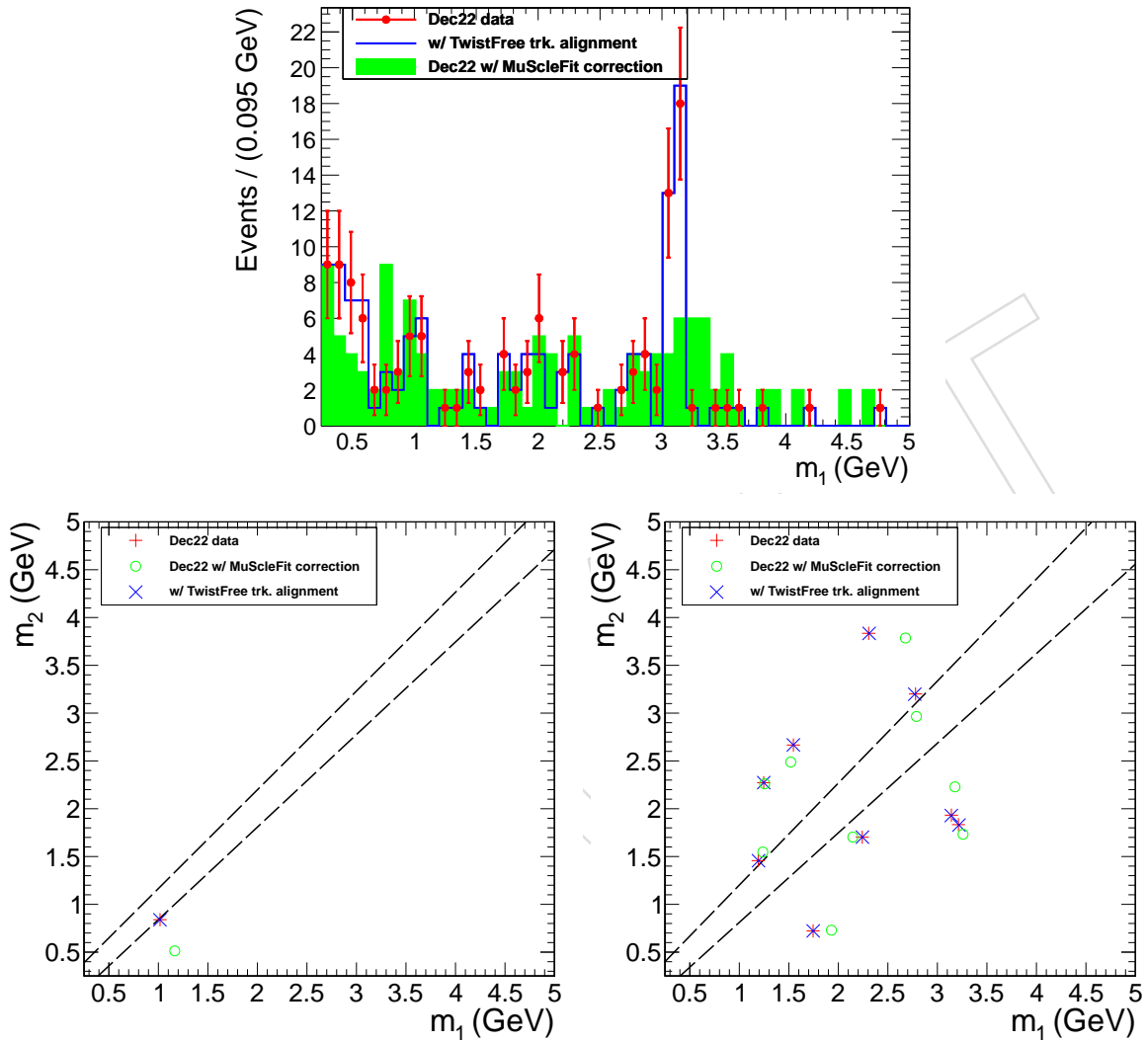


Figure 48: Invariant mass plots with a first-principles corrected alignment (blue) and MuScleFit track momentum corrections (green). Top: region (a-1); bottom-left: region (a-2); bottom-right: region (b-1).

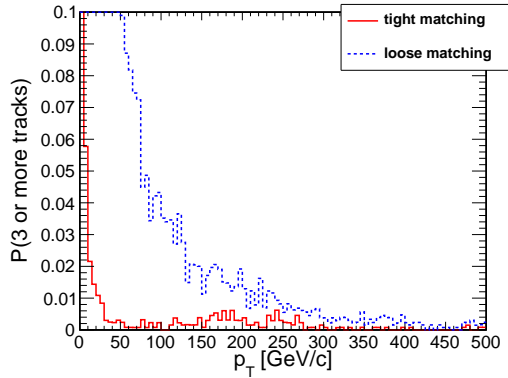


Figure 49: Probability of matching more than the two generated muons for tight and loose matching criteria (described in text). The “tight” criteria are used for the remainder of this section.

be interpreted as inefficiency, since the two muons are reconstructed. To avoid the problem in this study, we define a dimuon to be reconstructed in the tracker if the number of tracks with ($p_T(\text{reco}) > \frac{1}{2}p_T(\mu^+)$ or $p_T(\text{reco}) > \frac{1}{2}p_T(\mu^-)$) and ($\Delta R(\text{reco}, \mu^+) < 0.2$ or $\Delta R(\text{reco}, \mu^-) < 0.2$) is at least two. To verify that this cut is not too tight or too loose, we repeated the study with looser cuts: $\frac{1}{2} \rightarrow \frac{1}{10}$ and $0.2 \rightarrow 0.5$. Every efficiency plot shown in this section is identical with the two sets of matching cuts, but the looser version has an unacceptably high mismatch rate, shown in Fig. 49.

Four levels of efficiency were considered:

- reconstructing two tracker-tracks, matched to the dimuon as described above;
- same with number of hits ≥ 8 and $\chi^2/N_{\text{dof}} < 4$ applied;
- reconstructing two TrackerMuons (with track quality cuts), matched to the dimuon as described above;
- same with number of arbitrated segments ≥ 2 .

Each cut is more restrictive than the previous, and the final set is the muon quality cuts used in the analysis. Efficiencies as a function of pair p_T , mass, and pair η are presented in Fig. 50, where it can be seen that a large source of inefficiency at high p_T is due to the tracker only, and sources of inefficiency at $|\eta| = 0.25$ and 0.85 are due to the muon system only. To make this point more clear, Fig. 51 shows the probability of passing muon cuts given two quality tracks.

Since the high- p_T effect of our interest is due to something in the tracker, in Fig. 52 we plot efficiencies as a function of how close the muon trajectories approach each other at various points in the tracker $\Delta\phi(R)$, similar to Fig. 21 in Appendix A, but at radii of 5, 20, 60, and 110 cm. At 5 cm, the muons encounter the first pixel layers, at 20 cm, they transition from the pixel detector to the inner silicon strip detector (TIB), at 60 cm, they transition from the inner to the outer strip detector (TOB), and at 110 cm, they exit the tracker. Events are further subdivided into two classes: “cowboys” ($\phi_0(\mu^+) > \phi_0(\mu^-)$, where ϕ_0 is the azimuthal angle at the collision point) and “sailors” ($\phi_0(\mu^+) < \phi_0(\mu^-)$).

The plots in Fig. 52 show a deep inefficiency at a well-defined $\Delta\phi(R)$ value for each radius R . The minimum efficiency passes through $\Delta\phi(R_0) = 0$ at an R_0 of about 25 cm: approximately the average tracker radius when weighted by detector resolution. The inefficiency therefore does not appear to be dominated by any tracker subsystem, but is an average property of

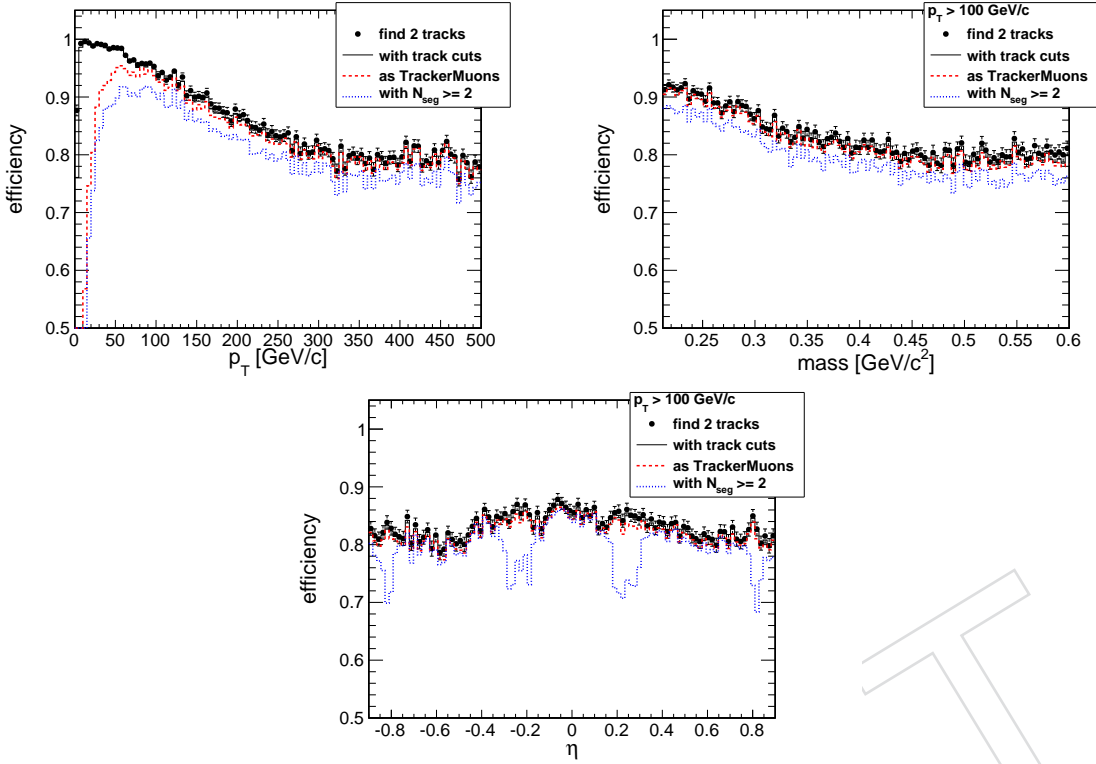


Figure 50: Probability of passing each of the four stages of cuts, given that two muons exist.

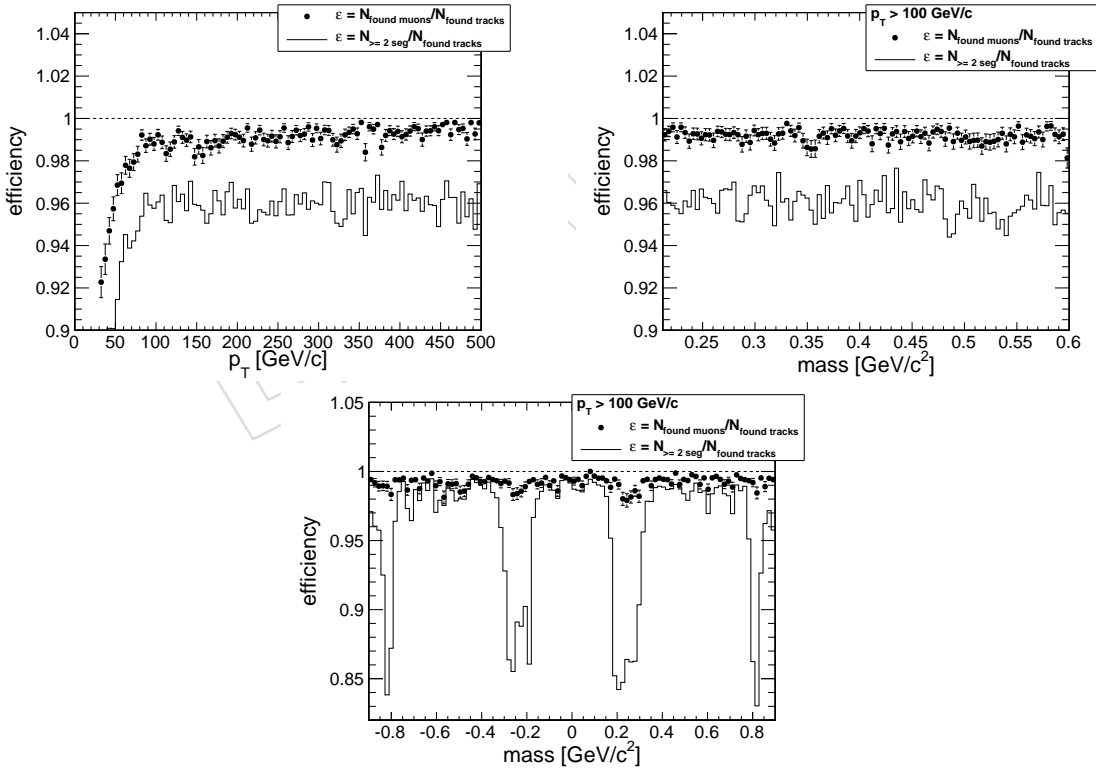


Figure 51: Probability of passing muon cuts, given that two reconstructed tracks exist.

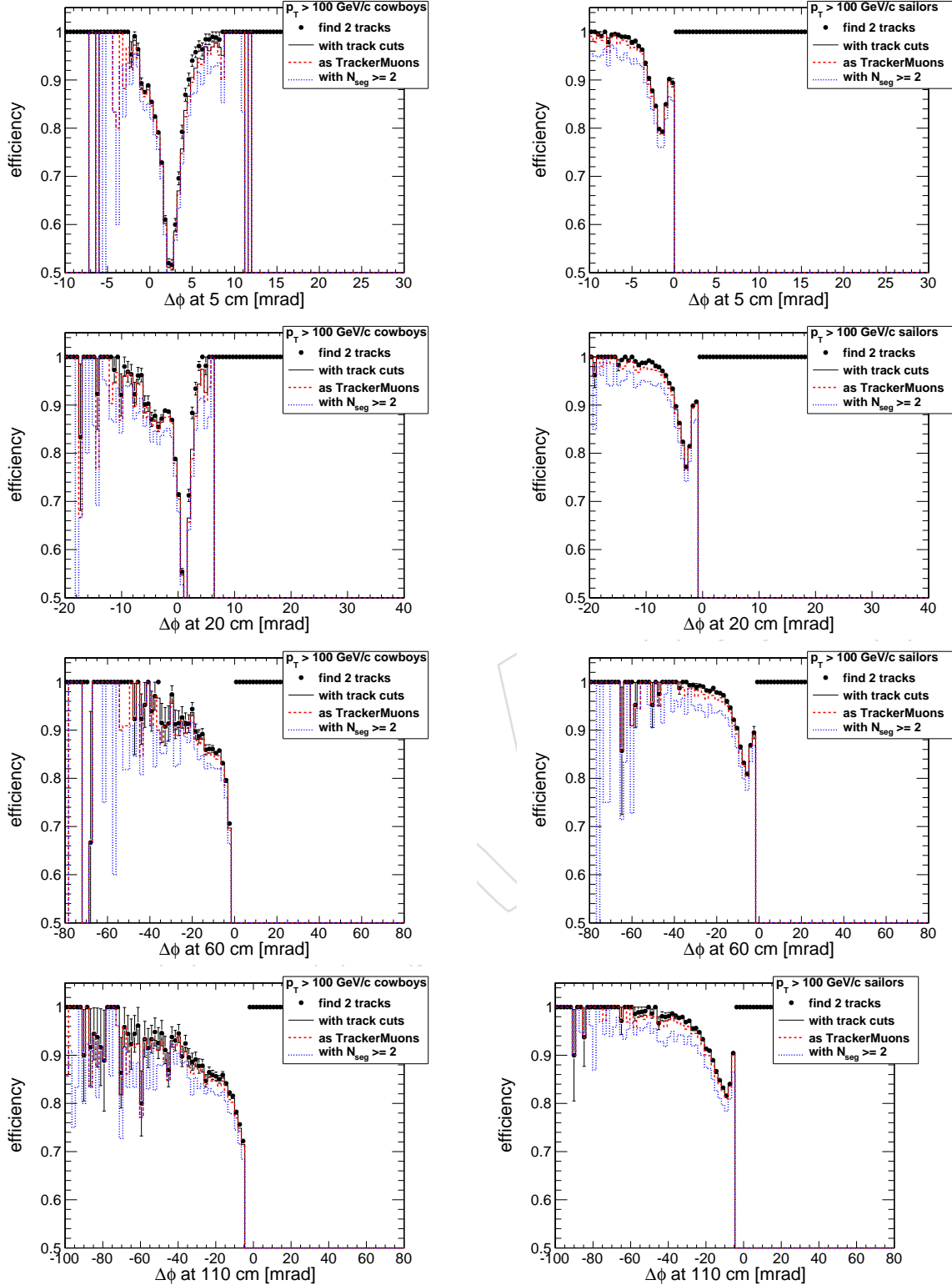


Figure 52: Efficiency as a function of distance of crossing in the bending plane $\Delta\phi(R)$ at various radii R in the tracker. Cowboys ($\phi_0(\mu^+) > \phi_0(\mu^-)$) are on the left, sailors ($\phi_0(\mu^+) < \phi_0(\mu^-)$) are on the right, with radius increasing toward the bottom of the page.

1426 track-fitting. This is consistent with expectations from Appendix L. For completeness, we show
 1427 efficiency as a function of $\Delta Z(R)/R$ in Fig. 53.

1428 To make the connection between detector-based variables, which show the effect most sharply,
 1429 and physics variables, which are relevant for setting efficiency systematics, we plot the tracker-
 1430 track inefficiency as a function of mass and pair p_T in Fig. 54. The region affected by the tracker
 1431 inefficiency broadly follows a line of constant boost of about $\gamma = 750$ (see also Fig. 55).

1432 O Dimuon efficiency study in U(1) samples

1433 References

- 1434 [1] O. Adriani et al., “Observation of an anomalous positron abundance in the cosmic
 1435 radiation”, *Nature* **458** (2009) 607–609.
- 1436 [2] D. Hooper, P. Blasi, and P. D. Serpico, “Pulsars as the Sources of High Energy Cosmic Ray
 1437 Positrons”, *JCAP* **0901** (2009) 025.
- 1438 [3] O. Arkani-Hamed et al., “A Theory of Dark Matter”, *Phys. Rev.* **D 79** (2009) 015014.
- 1439 [4] J. Hisano, S. Matsumoto, and M. M. Nojiri, “Explosive Dark Matter Annihilation”, *Phys.
 1440 Rev. Lett.* **92** (2004) 031303.
- 1441 [5] N. Cirelli, M. Kadastik, and A. Raidal, M. Strumia, “Model-independent implications of
 1442 the e+, e-, anti-proton cosmic ray spectra on properties of Dark Matter”, *Nucl. Phys.* **B 813**
 1443 (2009) 1–21.
- 1444 [6] O. Adriani et al., “A new measurement of the antiproton-to-proton flux ratio up to 100
 1445 GeV in the cosmic radiation”, *Phys. Rev. Lett.* **102** (2009) 051101.
- 1446 [7] Y. Bai and Z. Han, “A Unified Dark Matter Model in sUED”, *Phys. Rev.* **D 79** (2009)
 1447 095023.
- 1448 [8] P. J. Fox and E. Poppitz, “Leptophilic Dark Matter”, *Phys. Rev.* **D 79** (2009) 095023.
- 1449 [9] R. Bernabei et al., “New results from DAMA/LIBRA”, *Eur. Phys. J.* **C 67** (2010) 39–49.
- 1450 [10] Y. Bai and Z. Han, “Measuring the Dark Force at the LHC”, *Phys. Rev. Lett.* **103** (2009)
 1451 051801.
- 1452 [11] J. T. Ruderman, W. M. Maungart, C. Cheung et al., “Non-abelian dark sectors and their
 1453 collider signatures”, *JHEP* **04** (2009) 014.
- 1454 [12] V. Abazov and others (DØ Collaboration), “Search for Dark Photons from
 1455 Superseymmetric Hidden Valleys”, *Phys. Rev. Lett.* **103** (2009) 081802.
- 1456 [13] V. Abazov and others (DØ Collaboration), “Search for Events with Leptonic Jets and
 1457 Missing Transverse Energy in $p\bar{p}$ collisions at $\sqrt{s}=1.96$ TeV”, *Phys. Rev. Lett.* **105** (2010)
 1458 211802.
- 1459 [14] H. P. Nilles, M. Srednicki, and D. Wyler, “Weak Interaction Breakdown Induced By
 1460 Supergravity”, *Phys. Lett.* **B 120** (1983) 346.
- 1461 [15] J. M. Frere, D. R. T. Jones, and S. Raby, “Fermion Masses And Induction Of The Weak
 1462 Scale By Supergravity”, *Nucl. Phys.* **B 222** (1983) 11.

O Dimuon efficiency study in U(1) samples

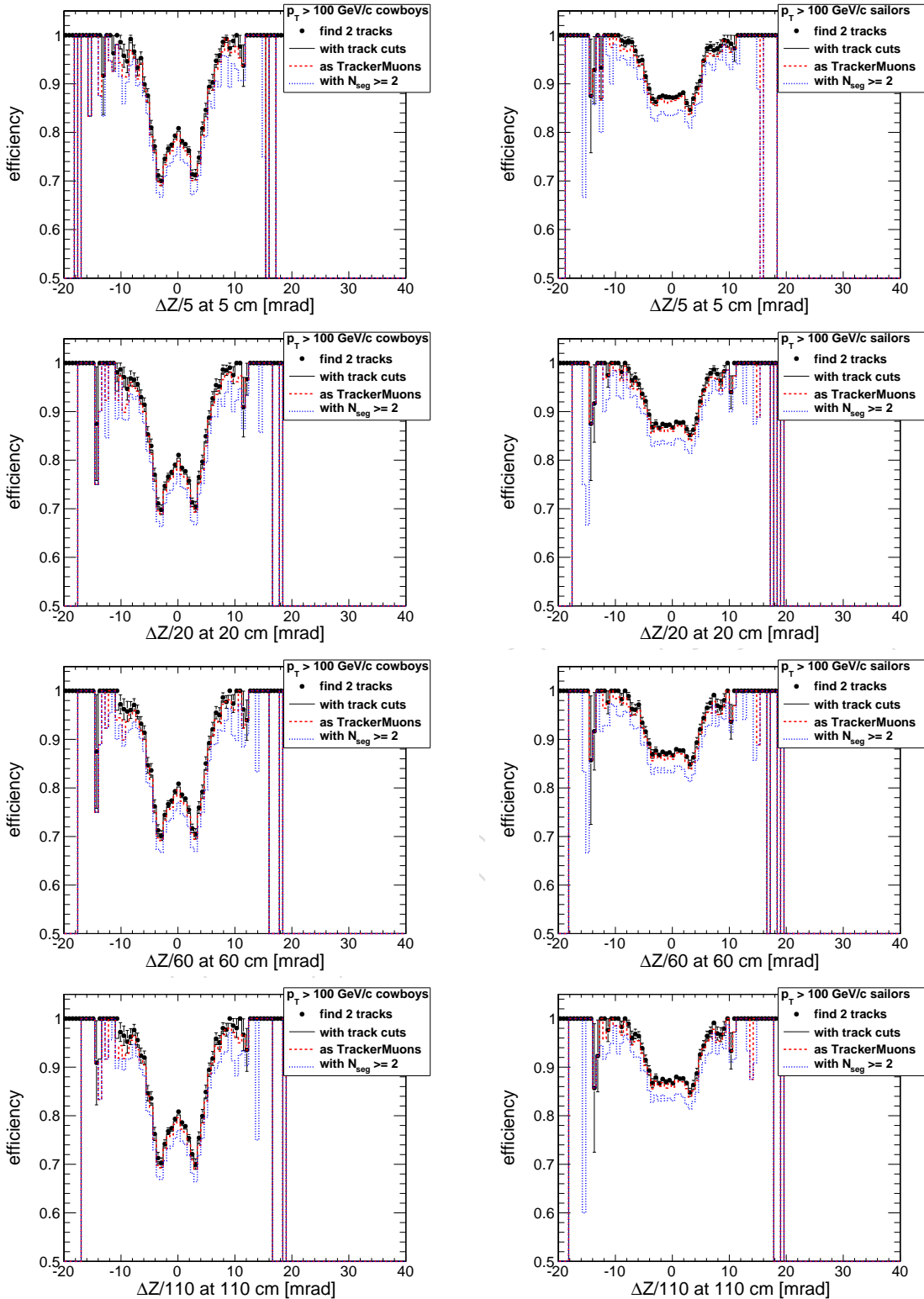


Figure 53: Efficiency as a function of distance of crossing parallel to the beamline $\Delta Z(R)/R$ at various radii R in the tracker.

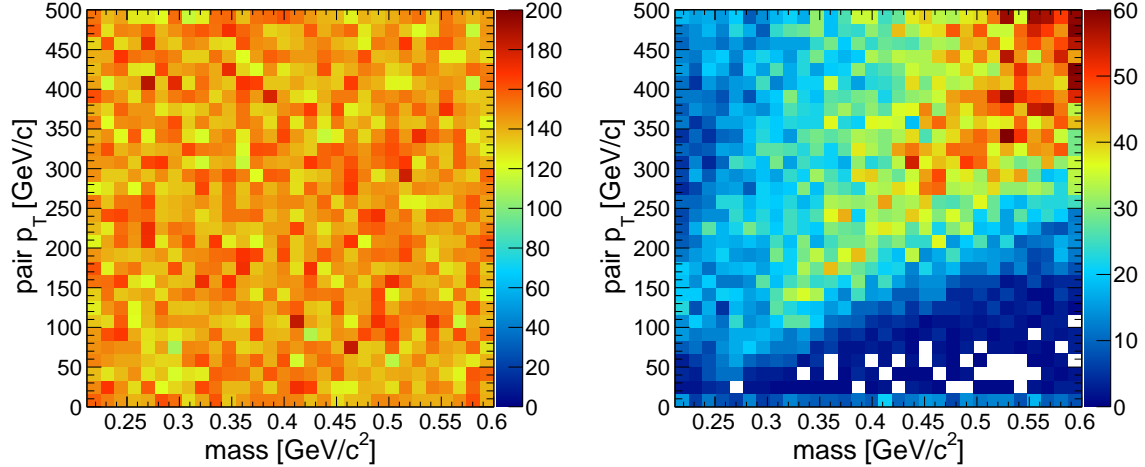


Figure 54: Two-dimensional histograms of mass and pair p_T used in the study. On the left, no cuts are applied, merely to demonstrate that the sample is uniform in mass and pair p_T , as intended. On the right, we require two tracker-tracks with quality cuts to *not* be found. This indicates the extent of the region affected by the tracker effect.

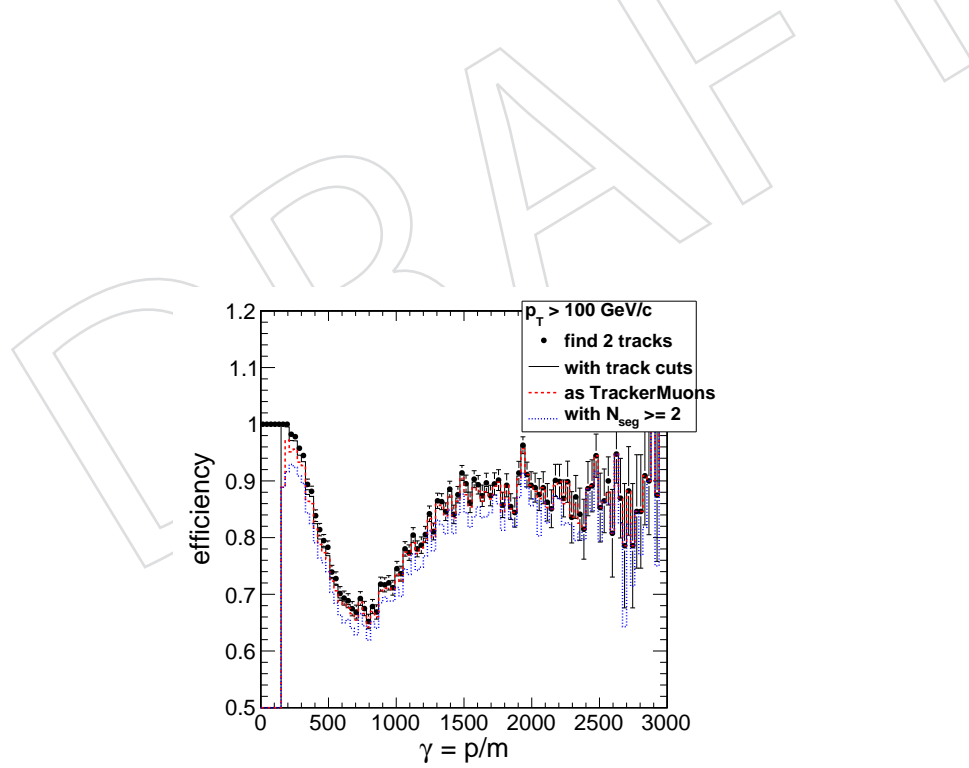


Figure 55: Efficiency as a function of relativistic boost γ .

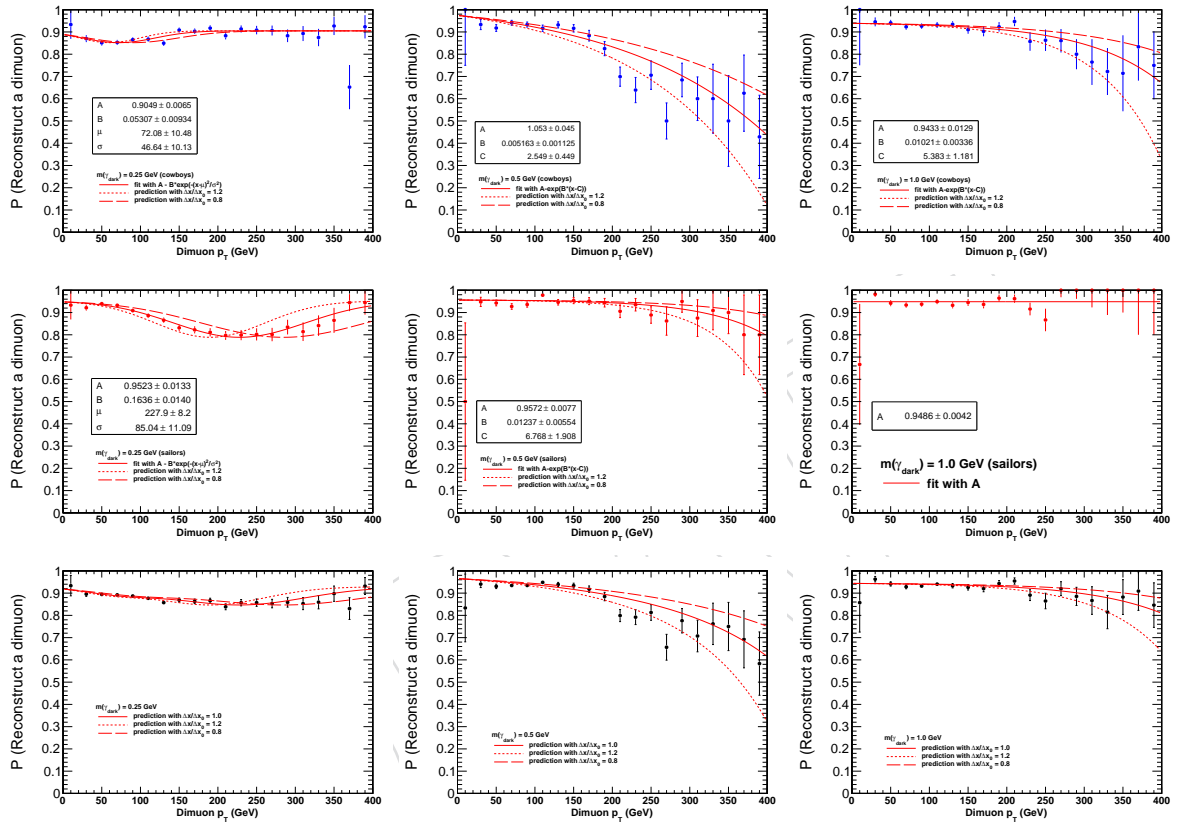


Figure 56: Prediction for dimuon efficiency when a cluster size is 20% more or less than default size and when $m(\gamma_{dark}) = 0.25 \text{ GeV}/c^2$ (left), $0.5 \text{ GeV}/c^2$ (center), $1.0 \text{ GeV}/c^2$ (right); separately for cowboys (top) and sailors (middle), for cowboys and sailors together (bottom)

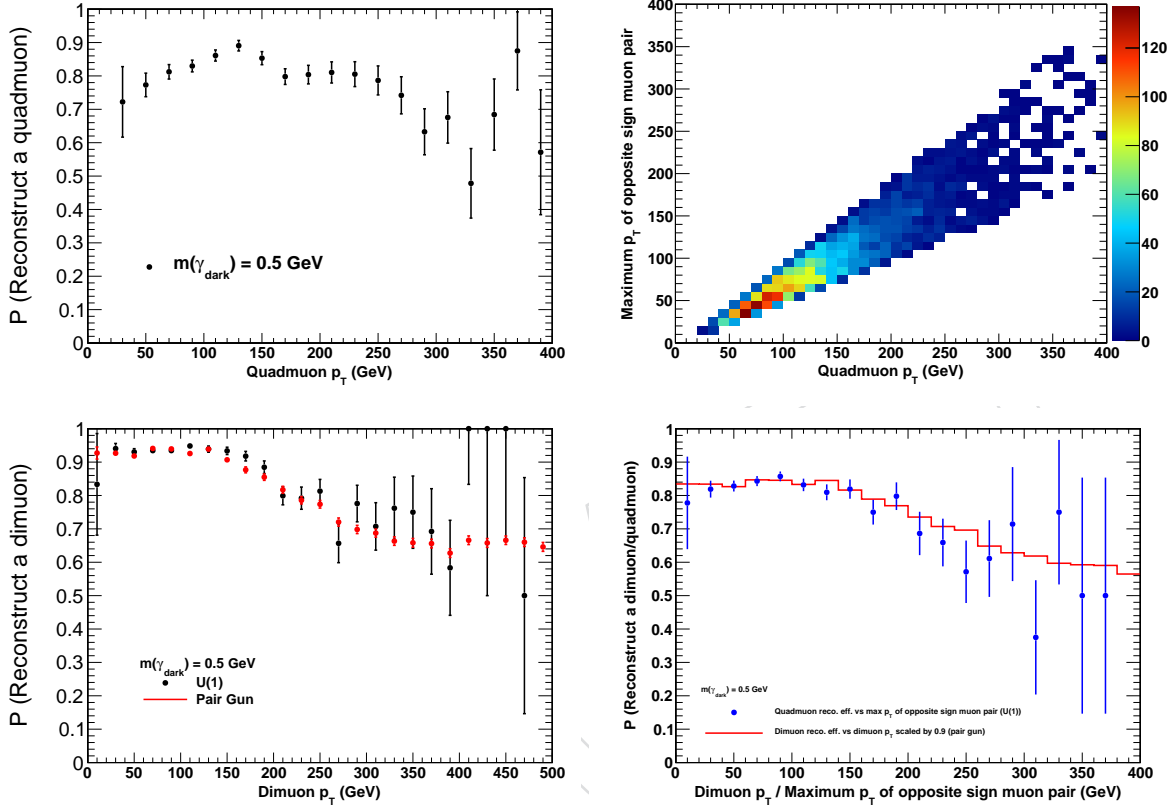


Figure 57: All plots are made with $m(\gamma_{dark}) = 0.5 \text{ GeV}/c^2$. Quadmuon efficiency as a function of quadmuon p_T (top left), quadmuon p_T as a function of maximum p_T of opposite sign muon pair within quadmuon (top right), dimuon efficiency from $U(1)$ and pair gun samples (bottom left), dimuon efficiency as a function of dimuon p_T scaled down in low- p_T region to quadmuon efficiency as a function of maximum p_T of opposite sign muon pair within quadmuon (bottom right)

- [16] J. R. Ellis, J. F. Gunion, H. E. Haber et al., "Higgs Bosons in a Nonminimal Supersymmetric Model", *Phys. Rev.* **D 39** (1989) 844.
- [17] M. Drees, "Supersymmetric Models with Extended Higgs Sector", *Int. J. Mod. Phys.* **4** (1989) 3635.
- [18] U. Ellwanger, M. Rausch de Traubenberg, and C. A. Savoy, "Particle spectrum in supersymmetric models with a gauge singlet", *Phys. Lett.* **B 315** (1993) 331.
- [19] U. Ellwanger, M. Rausch de Traubenberg, and C. A. Savoy, "Higgs phenomenology of the supersymmetric model with a gauge singlet", *Z. Phys.* **C 67** (1995) 665.
- [20] D. J. Miller, R. Nevzorov, and P. M. Zerwas, "The Higgs sector of the next-to-minimal supersymmetric standard model", *Nucl. Phys.* **B 681** (2004) 3.
- [21] R. Dermisek and J. F. Gunion, "Escaping the large fine tuning and little hierarchy problems in the next to minimal supersymmetric model and $h \rightarrow a_1 a_1$ decays", *Phys. Rev. Lett.* **95** (2005) 041801.
- [22] J. E. Kim and H. P. Nilles, "The Mu Problem And The Strong CP Problem", *Phys. Lett.* **B 138** (1984) 150.
- [23] A. Belyaev, J. Pivarski, A. Safonov et al., "LHC discovery potential of the lightest NMSSM Higgs in the $h \rightarrow a_1 a_1 \rightarrow 4$ muons channel", *Phys. Rev.* **D 81** (2010) 075021.
- [24] G. o. O. C. Abiendi *EPJC* **27** (2003) 483–495.
- [25] W. Love and others (CLEO Collaboration), "Search for Very Light CP-Odd Higgs Boson in Radiative Decays of Upsilon(S-1)", *Phys. Rev. Lett.* **101** (2008) 151802.
- [26] B. Aubert and others (BABAR Collaboration), "Search for Dimuon Decays of a Light Scalar Boson in Radiative Transitions Upsilon \rightarrow gamma A0", *Phys. Rev. Lett.* **103** (2009) 081803.
- [27] V. Abazov and others (DØ Collaboration), "Search for NMSSM Higgs bosons in the $h \rightarrow a_1 a_1 \rightarrow \mu\mu\mu\mu$, $\mu\mu\tau\tau$ channels using ppbar collisions at $\sqrt{s} = 1.96$ TeV", *Phys. Rev. Lett.* **103** (2009) 061801.
- [28] J. Alwall et al., "MadGraph/MadEvent v4: The New Web Generation", *JHEP* **0709** (2007) 028.
- [29] A. Pukhov, "CalcHEP 2.3: MSSM, structure functions, event generation, batchs, and generation of matrix elements for other packages", *arXiv:hep-ph/0412191v2* (2004).
- [30] P. Meade and M. Reece, "BRIDGE: Branching Ratio Inquiry / Decay Generated Events", *arXiv:hep-ph/0703031v2* (2007).
- [31] T. Sjostrand, S. Mrenna, and P. Skands, "PYTHIA 6.4 Physics and Manual", *JHEP* **0605** (2006) 026.
- [32] M. Spira, A. Djouadi, D. Graudenz et al., "Higgs boson production at the LHC", *Nucl. Phys.* **B 453** (1995) 17.
- [33] C. Balazs, H. J. He, and C. P. Yuan, "QCD corrections to scalar production via heavy quark fusion at hadron colliders", *Phys. Rev.* **D 60** (1999) 114001.

-
- 1501 [34] U. Ellwanger, J. F. Gunion, and C. Hugoine *JHEP* **0502** (2005) 066.
- 1502 [35] M. Spira *Nucl. Instrum. Meth. A* **389** (1997) 357.
- 1503 [36] CMS Collaboration, S. Chatrchyan et al., “Commissioning and Performance of the CMS
1504 Pixel Tracker with Cosmic Ray Muons”, *JINST* **5** (2010) T03007, arXiv:0911.5434.
1505 doi:10.1088/1748-0221/5/03/T03007.
- 1506 [37] CMS Collaboration, S. Chatrchyan et al., “Commissioning and Performance of the CMS
1507 Silicon Strip Tracker with Cosmic Ray Muons”, *JINST* **5** (2010) T03008,
1508 arXiv:0911.4996. doi:10.1088/1748-0221/5/03/T03008.
- 1509 [38] CMS Collaboration, V. Khachatryan et al., “CMS Tracking Performance Results from
1510 early LHC Operation”, *Eur. Phys. J. C* **70** (2010) 1165–1192, arXiv:1007.1988.
1511 doi:10.1140/epjc/s10052-010-1491-3.

DRAFT